Interfacial Behavior of 2D Materials in Devices for Solar Fuels and Sensing Applications

Thesis by

Annelise C. Thompson

In Partial Fulfillment of the Requirements
for the degree of
Doctor of Philosophy

CALIFORNIA INSTITUTE OF TECHNOLOGY
Pasadena, California

2019
(Defended May 30, 2019)

Annelise C. Thompson
ORCID: 0000-0003-2414-7050

ACKNOWLEDGEMENTS

Nature abhors a vacuum and so does the completion of a thesis. I am indebted to numerous people for helping me along the way to completing my dissertation. While I cannot possibly list everyone here, I want to acknowledge a few people who have had a lasting impact on my time at Caltech.

I would like to begin by thanking the many Lewis group members who have provided me with invaluable guidance and taught me everything I know about electrochemistry. To whole the Noyes crew over the years, Betar, Jonathan, Noah, Adam, Azhar, Ethan, Burt, Mo, Ellen, Michael, Sean, and occasional visitor (Sonja, Victoria, and Miguel) you have made graduate school infinitely more fun than it would have been otherwise. From dust woes to séances to strange door quotes, Noyes 220 is the best!

First and foremost from that wonderful group, I would like to thank Adam Nielander, who was my mentor when I started in the group. Thanks for teaching me how to use a potentiostat, for endless patience with our finicky projects, and being supportive of my work even as you have moved onto other endeavors.

I would like to specially thank Jonathan, Ethan, and Azhar for being part of the original crew that truly made Noyes a home for the weird. How do I encompass the joy and oddities of our friendship? I will always have fond memories of late night conversations over whisky and popcorn about squiggles, science, and life. Sharing the solar eclipse in August 2017 with you will always be burned into my memory as a crazy and amazing adventure. Square oatmeal anyone? Here is to more late nights and insane trips in the future!

I would not be here without the help of Burt. Our collaboration has grown into a great friendship. I appreciate your sass, scientific rigor, and continual (failed?) attempts to keep me relatively sane, especially in the last six months.

The Lewis group would not be the same without the excellent group of women who have joined over the years. As someone who joined the group when there were few women graduate students in the group, it has been a real pleasure to see our ranks swell over the past four years! I have enjoyed our GirlChats and am even happier that they have continued on in my absence while I have been writing my thesis.

A few women, postdocs and graduate students, deserve special thanks. Sonja and Betar, you still serve as inspiration for me. You both welcomed me into the group and helped me kick my imposter syndrome to the curb as I started at Caltech. Kyra, thanks for being a friend and collaborator. I am so glad we have had the chance to work together during my time here. Your patience in the past few months has been so helpful to completing the work in Chapter 4. Ellen, from when we were the two bastions of sanity in Noyes to our escape of the Noyes flood to the BI, I love that we have gotten closer even as our desks have gotten further apart! Mo, it has been so great to get to know you more over our late nights in lab. I know you will keep Noyes 220 appropriately weird in my absence and full of plain donuts.

A special thanks to the staff of on-campus administrative offices and facilities. You may not realize the small ways you continually improve the experience of graduate students around campus. Thank you for your hard work maintaining our campus and frequently fixing the AC in Noyes 220.

Thanks as well to my advisor, Dr. Nate Lewis, and my committee, Dr. Harry Gray, Dr. Mitchio Okumura, and Dr. Kimberly See. I have appreciated your insight into my research and your many words of encouragement throughout my time at Caltech.

I am also grateful for my graduate ResLife family, including Felicia, Nilza, Stephanie, Emily, Donal, Miggy, and Sina for friendship and support. I could not have asked for better coworkers and friends.

And, of course, I would like to thank the numerous friends who have also contributed to my time at Caltech.

Sara and Rachel, thank you for being excellent friends and lunch companions for the past five years. It’s been invaluable to lean on you for advice, support, and commiseration.

Sonya, Ryan, Lynn, Garrett, Sean, and Mak, thanks for always being there even when I was buried in lab work. It took me five years, but I finally beat this escape room too!

To my aerial ladies, especially Robyn and Keely in the past few months, thanks for helping distract me from the everyday concerns of graduate school, getting me out of my shell, and being excellent friends and spotters. Point your toes!

Finally, I would like thank the people who have been with me from the start, my loving and wonderful family. Allison and Dan, thank you for continuously opening your home to me and providing support in the form of food, love, and endless phone calls throughout the past five years. Allison, you are the best big sister ever (and certainly one of the few sisters to have helped edit her sister’s thesis!). The way you *elucidate* my mistakes never ceases to make me laugh.

And, despite what people may assume about living near your parents, nothing can capture the absolute joy it has been to live near my parents as an adult. I have had the extraordinary privilege of becoming close friends with you, Mom and Dad, and that will forever be the best thing I have taken away from my graduate school experience.

ABSTRACT

The field of 2D materials has expanded widely in the past 15 years to include many materials beyond graphene. However, the applications of graphene and its derivatives are still limited by the lack of thorough knowledge on how to successfully integrate a 2D material into a device while maintaining its unique properties. The work in this thesis investigates the application of 2D materials, such as graphene, fluorinated graphene, and hexagonal boron nitride, in solar fuels and sensing devices to reveal patterns that can inform device design with these and other materials in the future. In the second chapter, lightly fluorinated graphene is investigated as a protective layer on silicon photoanodes. This material is shown to possess superior abilities as a protective layer against oxidizing conditions as well as other deleterious surface reactions. The introduction of fluorine atoms to the lattice at postulated to terminate defects found along grain boundaries, leading to enhanced stability over 24h. The third chapter addresses the energetics of silicon/2D material/liquid junctions to elucidate how the density of states in these materials affect the formation of efficient charge-separation junctions. Hexagonal boron nitride on p-type silicon is shown to form a superior junction to graphene, as measured by changes in the open-circuit potential against a range of one-electron redox couples. Finally, chapter four shows the integration of a monolayer of graphene into a polymer-based chemiresistive vapor sensor to substantially enhance the signal of the sensor over the graphene or polymer alone. The response is dependent on strain at the graphene interface as demonstrated by Raman spectroscopy.

PUBLISHED CONTENT AND CONTRIBUTIONS

Thompson, A. C. et. al. (2016). “Lightly Fluorinated Graphene as a Protective Layer for n-Type Si(111) Photoanodes in Aqueous Electrolytes”. In: *Nano Letters*, 16(3), pp 4082-4086. doi: 10.1021/acs.nanolett.6b00773

> A.C.T. participated in the conception of the project, collected and prepared the data, and co-wrote the manuscript with A.C.N.

TABLE OF CONTENTS

LIST OF FIGURES AND TABLES

COMMON ABBREVIATIONS

2D material	a general topological (or two-dimensional) material
A/A^-	general expression for a one-electron redox couple; also A/A^+
Cc	one-electron redox couple; cobaltocene$^{+/0}$ or $Cp_2Co^{+/0}$
DecaMeCc	one-electron redox couple; decamethylcobaltocene$^{+/0}$ or $Cp^*{}_2Co^{+/0}$
DecaMeFc	one-electron redox couple; decamethylferrocene$^{+/0}$ or $Cp^*{}_2Fe^{+/0}$
DiMeFc	one-electron redox couple; dimethylferrocene$^{+/0}$ or $Me_2Cp_2Fe^{+/0}$
E_{CB}	energy of the conduction band of a semiconductor in eV
E_F	energy of the Fermi level of a material in eV
E_G	energy of the bandgap of a semiconductor in eV
E_{VB}	energy of the valence band of a semiconductor in eV
E(A/A-)	potential of an arbitrary redox couple in volts
$E°$	formal potential of a redox couple in volts
E_{eff}	effective potential of a redox couple in volts
Fc	one-electron redox couple; ferrocene$^{+/0}$ or $Cp_2Fe^{+/0}$ or $Fc^{+/0}$
F-Gr	fluorinated graphene
Gr	graphene
h-BN	hexagonal boron nitride
MV	one-electron redox couple; methyl viologen$^{2+/+\bullet}$ or $MV^{2+/+\bullet}$
Nc	one-electron redox couple; nickelocene$^{+/0}$ or $Cp_2Ni^{+/0}$
n-Si	an n-type silicon wafer; dopant density specified by chapter
n-Si/F–Gr	an interface formed by a fluorinated graphene overlayer on n-type silicon
p-Si	a p-type silicon wafer; dopant density specified by chapter
p-Si/Gr	an interface formed by graphene overlayer on p-type silicon
p-Si–H	a p-type silicon wafer treated with a buffered hydrofluoric acid solution to fully terminate the surface with hydrogen atoms
p-Si/h-BN	an interface formed by hexagonal boron nitride on p-type silicon

Chapter 1
An Introduction to 2D Materials

The successful isolation of monolayer graphene in 2004 prompted an explosion of research in the field of two-dimensional (2D) electronics. Graphene has been the subject of extensive research to understand and modulate its electronic properties because of its ballistic-level carrier mobility[1] and ambipolar field effect,[2] coupled with its 2D nature and remarkable strength.[3] While people have long claimed that graphene will revolutionize technology, this revolution has yet to occur due to the difficulty of designing scalable, reproducible graphene syntheses[4], the fundamental limitations imposed by the lack of a bandgap in graphene[5], and the challenge of integrating this material in devices while maintaining its unique properties.

While graphene still dominates work in this field, a large number of new materials has been isolated or grown in the past decade, including 2D semiconductors like the transition metal dichalcogenides (TMDs) and topological insulators like hexagonal boron nitride (h-BN). These discoveries have been driven by the need to isolate 2D materials that overcome the device limitations imposed by the semimetal character of graphene, while retaining high carrier mobilities for integration in a variety of fast, flexible electronics. Still, graphene serves both as a useful comparison to the other materials and a model for the behavior of a 2D semimetal. Graphene and its derivatives have been proposed for use in numerous applications, from advanced flexible electronics to components in polymer composites. This chapter will introduce a basic understanding of 2D material behavior and describe the three different areas within the field of 2D materials covered by this thesis: the ability of graphene and its derivatives to protect semiconductors from deleterious surface reactions, to control the band energetics at semiconductor/liquid junctions, and to enhance signal response in chemiresistive vapor sensors.

Properties of 2D Materials

Monolayer graphene is a semi-metallic 2D material composed entirely of carbon atoms (Figure 1). The atoms in the lattice are bonded together by sp^2-hybridized orbitals, making graphene a planar material with a thickness of only 3 Å.[2] The p_z orbitals, which are not involved in the C–C bonds of the lattice, stick up from the basal plane of the material. The overlap of these orbitals form bands that meet at the Dirac point, which allows the ballistic lateral transport of electrons and holes.[2] As a result, graphene has no bandgap and has a linearly decreasing density of states near the Fermi level. This honeycomb lattice of sp^2-hybridized carbon atoms is also chemically stable and impermeable to oxygen and water.[6,7] Its atomically thin nature makes it highly transparent, transmitting 97% of impinging light in the visible spectrum.[8] The uniformity of atoms within the basal plane contribute to the high stability and low reactivity of the lattice. Thus, pristine graphene is effectively inert.

Aggressive methods are needed to functionalize the basal plane of graphene. Due to the stability of the pristine lattice, it has been established that structural irregularities are critical for applications of graphene.[6] These defects can detract from the other beneficial properties of graphene—particularly charge mobility—as defective graphene has much lower conductivity than pristine graphene.[7] While these irregularities manifest as permanent defects to the lattice, electronic irregularities like those introduced by strain do not damage the network of C–C bonds in the basal plane.[8] Many methods have been designed to tune the bandgap of graphene, including but not limited to: substitutional doping of the graphene lattice during growth, noncovalent interactions with electron-rich and electron-poor molecules,[9] and covalent functionalization.[7] Researchers commonly prefer the last of these methods because it has proven the most effective for permanently altering the electronic properties of graphene.[7]

While no covalent functionalization can fully maintain the pristine nature of the lattice – the carbon atoms by necessity become tetravalent upon successful functionalization – the limitations that arise from the creation of permanent defects in the graphene lattice have prompted the search for functionalization methods that can lead to different electronic properties in the resulting lattice. One such modification is fluorination of monolayer graphene, which generates a corrugated, insulating lattice. Fully-fluorinated graphene has a bandgap of 3.0 eV and is very stable over time.[10] With such a large bandgap, this material has no density of states near its Fermi level. This characteristic makes fully fluorinated graphene a superior material to unfluorinated graphene, as it can be integrated into conventional electronics as a dielectric, whereas graphene has no direct analog in the field of semiconductor processing.[11]

The stability of the fully fluorinated material has led some to equate it to 2D Teflon.[10,12] This nickname for fluorinated graphene belies the reactive nature of the more common partially fluorinated graphene derivatives. Partially fluorinated graphene is actually quite reactive, showing the spontaneous detachment of fluorine in a matter of days after fluorination, which has led to its use as a precursor for subsequent functionalization.[13,14] As a result, many methods have been used to try to achieve full fluorination of the basal plane of graphene to achieve greater stability of the lattice. These methods include exposure to various strong fluorine chemistries, including hydrofluoric acid, XeF_2 gas, and CF_4 and SF_6 plasmas.[15] However, the methods that introduce the most fluorine also introduce the most disorder to the lattice and eventually destroy the lattice entirely. Thus, the partially fluorinated material is more widely studied than the fully fluorinated derivative and can take on a range of characteristics, depending on the degree of fluorination of the underlying basal plane.[16]

Similar to fluorinated graphene, hexagonal boron nitride (h-BN) is a topological insulator, but it is a single monolayer of atoms in its pristine forms. While it has the same crystal structure as graphene, h-BN is formed of an alternating honeycomb lattice of boron and nitrogen atoms with lattice parameters very close to those of graphene and fluorinated graphene ($r_{B\text{–}N}$ = 1.45 Å while $r_{C\text{–}C}$ = 1.42 Å). It has the largest bandgap of the known 2D materials at ~6.0 eV.[17] The highly insulating and inert nature of h-BN has made it most commonly used as a passivation layer in devices, as it can stabilize a surface without significantly changing the behavior of the underling layers.

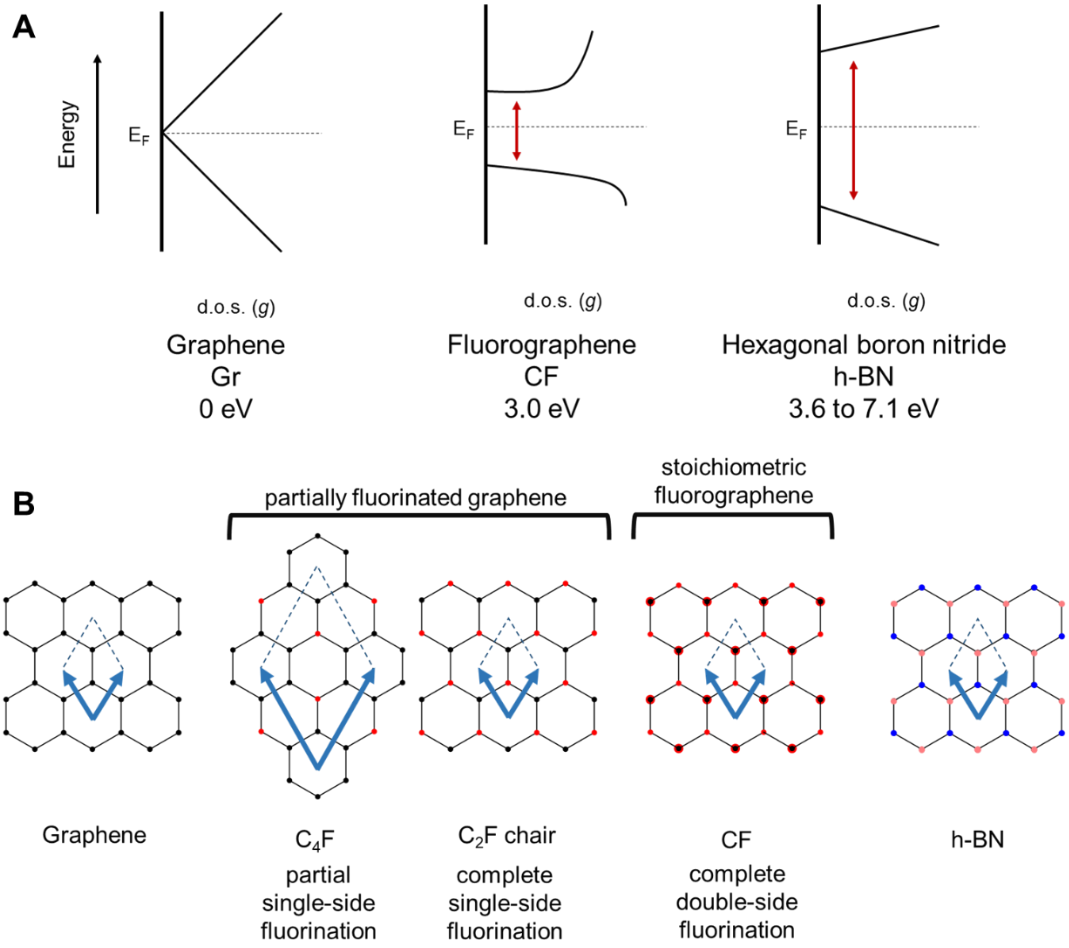

Figure 1. 2D materials used in this thesis. A) Density of states (**g**) for graphene and fully single-side fluorinated graphene (C$_4$F). The D.O.S. for fluorographene is significantly further from the intrinsic Fermi level for graphene while h-BN is completely insulating. B) The unit cells for graphene and fluorinated graphene. There are multiple ways that fluorine can bond to the basal plane to form partially fluorinated graphene.

Protective layers in photoelectrochemical cells

Photoelectrochemical (PEC) cells are unique in that the charge-separating junction of the device is formed at a semiconductor/liquid interface instead of a semiconductor/solid interface, as is found in standard photovoltaic (PV) cells. Fabrication of a PEC device can be as simple as submerging a semiconductor in an appropriate electrolyte solution. These devices can generate chemical fuel directly via photon-driven water-splitting at the semiconductor surface without a separate electrolyzer (E), as a typical PV strategy would require. By eliminating the need for a separate electrolyzer, we expect the PEC cell to reduce the total cost of the solar water-splitting process compared to the common PV+E strategy.[2]

The protection of semiconductor surfaces from passivation and corrosion upon exposure to aqueous solution under photoanodic conditions is one of the foremost challenges facing the fabrication of stable PEC devices.[3] To prevent these deleterious reactions, several protection strategies have been developed, including various metallic and metal oxide protective layers for photoanodes. However, these layers generally reduce effective light absorption and thus limit energy conversion efficiency.[3,4] Protective metallic layers are limited by loss of majority carriers to the recombination processes that are promoted by thermionic emission at the interface. Protective metal oxide layers are limited by the thickness required for protection; films of promising oxide materials become more porous as they are made thinner to decrease absorption and prevent loss to reflection, which limits their effectiveness. Ideally, a protective layer would be optically transparent, while preventing deleterious surface reactions and still allowing for an efficient charge-separating junction to form.[3]

As a protective layer on n-type silicon (n-Si) under illumination in photoanodic conditions for 1000s, graphene has been shown to only partially pin the graphene/semiconductor interface, due to the lack of states at the Fermi level (Figure 1).[9]

However, current growth methods limit the use of graphene as a protective layer.[9] Exfoliation, or “the Scotch tape method,” produces single-crystal graphene pieces that are small (~100 μm) and difficult to locate optically. Chemical vapor deposition (CVD) growth can be used to make polycrystalline sheets with variable grain size. However, diffusion through grain boundaries and defects from wet-chemistry transfers have stymied the use of CVD-grown graphene as the ubiquitous, transferable protective layer it could be.[10,11] In addition, small amounts of contaminants left behind after wet transfer are known to dope the graphene sheets, which allows easy access to more deleterious surface states by charge carriers at the interface.[12,13] It would be beneficial to limit the effect of high-energy defect sites and grain boundaries on the performance of graphene-based electrodes through passivation and limit the number of surface states easily accessible to charge carriers at a graphene/semiconductor interface.

Recent work has shown that various protective layers, such as HfO_2 and TiO_2, can react with high energy defect sites and effectively repair some of the damage to the honeycomb structure of graphene, preventing unwanted diffusion through the lattice.[14,15] With this in mind, Chapter 2 will detail work using monolayer fluorographene on a semiconductor photoanode to stabilize the surface and form an efficient charge-separating junction for use in a solar water-splitting device through termination of defect sites with fluorine atoms.

Interfacial control at semiconductor/liquid junctions

To form an efficient charge-separating junction, we need to minimize the number of electronic states introduced by a protective layer with energy mid-gap to the semiconductor. In addition, the initial difference between the electrochemical potential of the semiconductor (E_F) and the contacting electrolyte determines the maximum efficiency of a photoanode or photocathode.[18] Efficient photoanodic devices have the edge of the valence band aligned with the electrochemical potential for the reaction of interest (E(A/A$^-$)), maximizing the extractable energy (Figure 2a). In contrast, photocathodic devices have the conduction band aligned with E(A/A$^-$) (Figure 2b). Thus, these interfaces can be optimized with the use of interstitial layers to tune the resulting efficiency for different applications, shown as a dipole in Figure 2. When a 2D material is used as this interstitial layer, the properties of the layer, particularly its density of states, are predicted to have a strong effect on the quality of the resulting interface. Since graphene has a Fermi level that falls between the the band edges of many semiconductors, it is not predicted to make an efficient charge-separating junction. Because h-BN has a large bandgap, there are no mid-gap states and it should produce a more efficient charge-separating junction than graphene would.[17] Chapter 3 will further explain how these interfaces were tested using macroscale and nanoscale techniques.

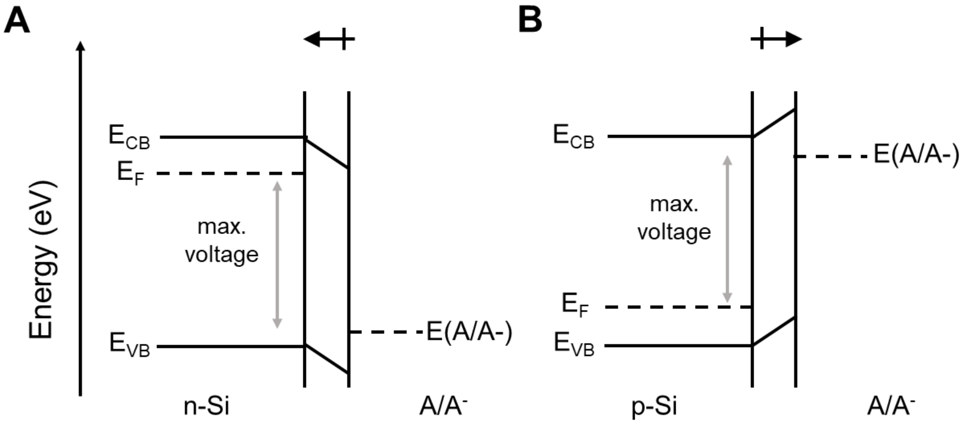

Figure 2. Energy diagrams for efficient charge-transfer in semiconductor/2D material/liquid junctions. An efficient semiconductor/2D material/liquid junction places the electrochemical potential of the contacting electrolyte (E(A/A$^-$)) close to the appropriate band given the dopant type in the semiconductor. A) For the n-Si/2D material/liquid junction, E(A/A$^-$) is moved closer to the the valence band. B) A p-Si/2D material/liquid junction has E(A/A$^-$) close to the conduction band. Note that the direction of the necessary surface dipole has switched for the two interfaces.

Strain-based sensing with graphene

Strain-induced reactivity of graphene is a promising method that explores the effect that controlled tensile and compressive strain of the basal plane of graphene has on reactivity. This technique relies on the strain-induced change in electron density along the basal plane to increase reactivity. In the same way that dangling bonds along grain boundaries or edges promote reactivity, these strain-induced hot spots have been shown to be highly reactive to graphene functionalization methods.[18–20] Unlike other methods for covalent functionalization, the generation of these reactive hot spots should also be fully reversible with the removal of strain from the lattice. Since strain significantly changes the conductivity of graphene, strain-based methods should allow the reversible changes to the conductivity of graphene with minimal damage to the underlying lattice.

Even with only minor rippling of the lattice, the lability of the C–C bonds still substantially increases because of reduced orbital overlap and increased localization of electron density.[21] From π-orbital angle vector (POAV) analysis – frequently used in discussions of fullerenes or other intrinsically strained carbon allotropes – deviation from sp^2 hybridization decreases electron delocalization and increases the chemical potential of the strained atoms.[22] That is, as the s-orbital character of the p_z orbital increases, the delocalization of the π-bond network decreases. The deformation of graphene and the resulting charge localization alter the conductivity through the monolayer, creating a detectable change in the resistance across the lattice.

This reversible and detectable change in conductivity makes graphene an ideal material to study as part of a chemiresistive sensor. These sensors detect the adsorption of particular chemicals through a change in the resistance of the sensing material. As the graphene lattice is very sensitive to perturbations, a sensor made with pristine graphene should have high sensitivity to molecule adsorption in contrast with the amorphous conductive carbon commonly used today. However, as highlighted previously, pristine graphene is relatively inert. Clean graphene actually shows very low selectivity to gases. In fact, most of the sensitivity attributed to graphene has been shown to be attributable to polymer contamination on the surface. Rather than excluding graphene from use in chemiresistive sensors though, this lack of selectivity has inspired the work detailed in Chapter 4, where a sensor is developed to amplify small changes in strain to large changes in resistance across the lattice through the integration of a textured substrate with and polymer-coated graphene layer.

Summary

Together the three materials used herein bridge a wide range of bandgaps currently accessible in 2D materials. The diverse work in this thesis characterizing the interfacial behavior of graphene, fluorinated graphene, and h-BN will allow scientists to elucidate the pattern of behavior expected as the density of states of these materials and to better predict the behavior of new 2D materials in the future.

References

1. Novoselov, K. S. *et al.* Two-dimensional gas of massless Dirac fermions in graphene. *Nature* **438**, 197–200 (2005).
2. Novoselov, K. S. *et al.* Electric Field Effect in Atomically Thin Carbon Films. *Science* **306**, 666–669 (2004).
3. Lee, C., Wei, X., Kysar, J. W. & Hone, J. Measurement of the Elastic Properties and Intrinsic Strength of Monolayer Graphene. *Science* **321**, 385–388 (2008).
4. Kauling, A. P. *et al.* The Worldwide Graphene Flake Production. *Adv. Mater.* **30**, 1803784 (2018).
5. Novoselov, K. Graphene: Mind the gap. *Nat. Mater.* **6**, 720–721 (2007).
6. Eftekhari, A. & Garcia, H. The necessity of structural irregularities for the chemical applications of graphene. *Mater. Today Chem.* **4**, 1–16 (2017).

7. Georgakilas, V. *et al.* Functionalization of Graphene: Covalent and Non-Covalent Approaches, Derivatives and Applications. *Chem. Rev.* **112**, 6156–6214 (2012).
8. Bissett, M. A., Tsuji, M. & Ago, H. Strain engineering the properties of graphene and other two-dimensional crystals. *Phys. Chem. Chem. Phys.* **16**, 11124–11138 (2014).
9. Liu, H., Liu, Y. & Zhu, D. Chemical doping of graphene. *J. Mater. Chem.* **21**, 3335–3345 (2011).
10. Nair, R. R. *et al.* Fluorographene: A Two-Dimensional Counterpart of Teflon. *Small* **6**, 2877–2884 (2010).
11. Ho, K.-I. *et al.* Fluorinated Graphene as High Performance Dielectric Materials and the Applications for Graphene Nanoelectronics. *Sci. Rep.* **4**, 5893 (2014).
12. Robinson, J. T. *et al.* Properties of Fluorinated Graphene Films. *Nano Lett.* **10**, 3001–3005 (2010).
13. Stine, R., Lee, W.-K., Whitener, K. E., Robinson, J. T. & Sheehan, P. E. Chemical Stability of Graphene Fluoride Produced by Exposure to XeF2. *Nano Lett.* **13**, 4311–4316 (2013).
14. Whitener, K. E., Stine, R., Robinson, J. T. & Sheehan, P. E. Graphene as Electrophile: Reactions of Graphene Fluoride. *J. Phys. Chem. C* **119**, 10507–10512 (2015).
15. Feng, W., Long, P., Feng, Y. & Li, Y. Two-Dimensional Fluorinated Graphene: Synthesis, Structures, Properties and Applications. *Adv. Sci.* **3**, 1500413 (2016).
16. Zhou, S., Sherpa, S. D., Hess, D. W. & Bongiorno, A. Chemical Bonding of Partially Fluorinated Graphene. *J. Phys. Chem. C* **118**, 26402–26408 (2014).
17. Zhang, K., Feng, Y., Wang, F., Yang, Z. & Wang, J. Two dimensional hexagonal boron nitride (2D-hBN): synthesis, properties and applications. *J. Mater. Chem. C* **5**, 11992–12022 (2017).

18. Bissett, M. A., Konabe, S., Okada, S., Tsuji, M. & Ago, H. Enhanced Chemical Reactivity of Graphene Induced by Mechanical Strain. *ACS Nano* **7**, 10335–10343 (2013).
19. Wu, Q. *et al.* Selective surface functionalization at regions of high local curvature in graphene. *Chem. Commun.* **49**, 677–679 (2013).
20. Park, M. J. *et al.* Enhanced Chemical Reactivity of Graphene by Fermi Level Modulation. *Chem. Mater.* (2018). doi:10.1021/acs.chemmater.8b01614
21. Deng, S. & Berry, V. Wrinkled, rippled and crumpled graphene: an overview of formation mechanism, electronic properties, and applications. *Mater. Today* **19**, 197–212 (2016).
22. Haddon, R. C. Rehybridization and .pi.-orbital overlap in nonplanar conjugated organic molecules: .pi.-orbital axis vector (POAV) analysis and three-dimensional Hueckel molecular orbital (3D-HMO) theory. *J. Am. Chem. Soc.* **109**, 1676–1685 (1987).

Chapter 2
2D Materials as protective layers on silicon photoanodes

This chapter has been adapted from the following citation. Further permissions related to the material excerpted should be directed to the ACS.

Thompson, A. C. et. al. (2016). “Lightly Fluorinated Graphene as a Protective Layer for n-Type Si(111) Photoanodes in Aqueous Electrolytes”. In: Nano Letters, 16(3), pp 4082-4086.
https://pubs.acs.org/doi/abs/10.1021/acs.nanolett.6b00773

Several protective coating strategies have been developed to suppress deleterious surface reactions associated with corrosion or passivation of semiconductor photoanodes in aqueous electrolytes.[1-2] NiO_x films prepared by reactive sputtering or amorphous TiO_2 films in conjunction with a Ni-oxide based electrocatalyst have produced extended stability for Si photoanodes and allow the photochemical evolution of O_2(g) from water under alkaline conditions.[3-4] Thin metallic overlayers or transparent conductive metal oxide protective layers often result in relatively low photovoltages due to thermionic emission of majority carriers at Si/overlayer Schottky contacts.[3-10] Insulating metal oxide barriers must be thin enough (a few nm) to permit conduction by tunneling, and such thin layers are difficult to prepare in a pinhole-free manner over macroscopic areas.[5, 11-12] Chemical functionalization has led to improved stability of n-Si surfaces, but such methods have not yet yielded stability over extended time periods in aqueous electrolytes.[13-15]

An ideal protective coating would be transparent, provide low resistance to charge transfer, allow for maximum energy-conversion efficiency for a range of semiconductor/electrolyte contacts, would be applied easily to semiconductor surfaces, would be capable of uniformly protecting macroscopic electrode areas, and would be chemically and electrochemically stable under the relevant conditions. Monolayer graphene can be prepared in large (>100 cm^2), pinhole-free layers and transferred to any arbitrary planar surface, and has been shown to inhibit oxidation of metals both in air and in aqueous solution.[16-21] Graphene is chemically inert, optically transparent, can be deposited onto surfaces at room temperature. Illuminated graphene-coated Si photoanodes in contact with neutral pH aqueous electrolytes have demonstrated stability for over 1000 s while providing desirable photoelectrochemical performance.[22-25] However, the graphene does not completely protect the Si photoanodes from oxidation, and the devices exhibit partial Fermi-level pinning which limits their energy-conversion efficiency. The incomplete protection and Fermi-level pinning are consistently ascribed to reactive sites near grain boundaries in the polycrystalline graphene produced by chemical-vapor deposition (CVD), and to the presence of mid-gap electronic states introduced at the n-Si/Gr interface as a result of the graphene electronic structure, respectively.

Relative to unfluorinated graphene, fluorination of graphene should reduce the density of states near the Fermi level, thus reducing Fermi level pinning effects, and should passivate reactive graphene defect sites via fluorine capping.[26-28] Accordingly, we report herein an investigation of the stability and photoelectrochemical behavior of fluorinated-graphene-coated Si photoanodes in contact with aqueous electrolytes.

Methods

Materials

Single-crystalline, Czochralski grown, (111)-oriented, planar, 380 μm thick, phosphorus doped, 1.1 Ω-cm resistivity (doping density, $N_D \approx 5 \times 10^{15}$ cm^{-3}) single-side polished n-type silicon wafers were obtained from University Wafer, Inc. Water was obtained from a Barnstead Nanopure system and had a resistivity ≥ 18.0 MΩ-cm. Copper Etch Type CE – 100 ($FeCl_3$-based, Transene Company, Inc., Danvers, MA), and buffered HF(aq) (semiconductor grade, Transene Company, Inc., Danvers, MA) were used as received. Acetone (HPLC grade, Sigma-Aldrich) was used as received.

Acetonitrile (99.8% anhydrous, Sigma-Aldrich) used in electrochemical measurements was dried over Al_2O_3 prior to use.

Ferrocene (Fc, bis(cyclopentadienyl)iron(II), 99%, Strem), cobaltocene ($CoCp_2$, bis(cyclopentadienyl)cobalt(II), 98%, Strem), and acetylferrocene (AcFc, (acetylcyclopentadienyl)-cyclopentadienyl iron(II), 99.5%, Strem) were purified via sublimation. Ferrocenium tetrafluoroborate ($Fc^+[BF_4]^-$, bis(cyclopentadienyl)iron(III) tetrafluoroborate, technical grade, Sigma-Aldrich) was recrystallized from a mixture of diethyl ether (ACS grade, EMD) and acetonitrile (ACS grade, EMD) and dried under vacuum. Cobaltocenium hexafluorophosphate ($CoCp_2^+$, bis(cyclopentadienyl)cobalt(III) hexafluorophosphate, 98%, Sigma-Aldrich) was recrystallized from a mixture of ethanol (ACS grade, EMD) and acetonitrile (ACS grade, EMD) and dried under vacuum. Acetylferrocenium ($AcFc^+$) was generated in situ via electrochemical oxidation of $AcFc^0$ with the concomitant reduction reaction occurring in a compartment that was separated by a Vycor frit from the working electrode compartment. Potassium ferricyanide ($K_3[Fe(CN)_6]$, 99.2%, Sigma-Aldrich) and potassium ferrocyanide ($K_4[Fe(CN)_6]•3H_2O$, ACS Certified, Fischer Scientific) were used as received. $LiClO_4$ (battery grade, Sigma-Aldrich) was used as received. Petri dishes used were Falcon Optilux™ branded and were cleaned with water prior to use. All other chemicals were used as received unless otherwise noted.

Electrode fabrication

Monolayer graphene was grown by chemical-vapor deposition (CVD) of carbon on Cu.[29] Additional CVD-grown monolayer graphene on Cu was purchased from Advanced Chemical Supplier Materials. A 2.5 cm x 1 cm piece of monolayer graphene on Cu (from either source) was fluorinated using a home-built XeF_2 pulse chamber, with one pulse of XeF_2 (g) at 2 Torr for 90 s with a base pressure of <1 mTorr.[28] X-ray photoelectron spectroscopy (XPS) of the resulting F–Gr confirmed the fluorination.[27-28]

The F–Gr was further characterized by UV/Vis and Raman spectroscopy. The fluorinated graphene samples on Cu were then coated with 495K A4 polymethyl methacrylate (PMMA, MicroChem) by spinning at 2000 rpm (500 rpm s^{-1} acceleration) for 60 s, followed by a 5 min bake at 185 °C. This procedure was repeated twice to yield a PMMA/F-Gr/Cu stack.

Smaller pieces were cut from the PMMA/F-Gr/Cu and floated in $FeCl_3$ solution until complete removal of the Cu (~1 h) was observed. To remove the etchant residue, each stack was transferred between five consecutive ≥18MΩ-cm resistivity water baths. N-type Si was etched for 30 s in buffered improved HF (Transene) to yield n-Si–H surfaces, and any SiO_2 was removed using a modified SC1/SC2 cleaning method. SC-1 consisted of soaking the Si wafers in a 5:1:1 (by volume) solution of H_2O, NH_4OH (~30 wt.%, J.T. Baker) and H_2O_2 (~35 wt.%, Sigma) for 10 min at 75^o C. After washing with H_2O, SC-1 cleaned wafers were exposed to SC-2 conditions, which consisted of soaking the Si wafers in a 5:1:1 (by volume) solution of H_2O, HCl (11.1 M, Sigma) and H_2O_2 (~35 wt.%, Sigma) for 10 min at 75 ^{o}C. A clean PMMA/F-Gr stack was then pulled gently onto the appropriate Si wafer and dried with a stream of $N_2(g)$ to remove any remaining water between the Si wafer and the graphene sheet. The final PMMA/F-Gr/wafer stack was baked at 80 °C for 10 min in air. The majority of the PMMA was detached with a 10 min acetone soak and the remaining PMMA residue was removed by an anneal (H_2:Ar v:v 5:95) for 2h at 350°C.[30]

Si/F-Gr electrodes were fabricated using Ga:In (75:25) eutectic as an ohmic back contact. The wafers were attached to a Cu wire with Ag paint (high purity, SPI Supplies).[29, 32] All surfaces except the F–Gr layer were covered with insulating epoxy (Loctite Hysol 9460). CH_3-terminated Si(111) wafers were prepared using a previously reported procedure.[31] H-terminated Si(111) electrodes were etched with HF(aq) immediately before use.

Instrumentation

X-ray photoelectron spectroscopic (XPS) data were collected at ~5 × 10^{-9} Torr using a Kratos AXIS Ultra DLD with a magnetic immersion lens that consisted of a spherical mirror and concentric hemispherical analyzers with a delay-line detector (DLD). An Al Kα (1.486 KeV) monochromatic source was used for X-ray excitation. Ejected electrons were collected at a 90° angle from the horizontal. The CASA XPS software package v 2.3.16 was used to analyze the collected data.

Raman spectra were collected with a Renishaw Raman microscope at λ=532 nm through an objective with numerical aperture=0.75. The laser power was ~ 3 mW.

UV/Vis transmission spectra were collected with a Cary 5000 absorption spectrometer equipped with an external DRA 1800 attachment. The data were automatically zero/baseline corrected by the instrument before any additional processing was performed.

Electrochemical data were obtained using a Princeton Applied Research Model 273, Biologic SP-250, or a Gamry Reference 600 potentiostat. A Pt wire reference electrode (0.5 mm dia., 99.99% trace metals basis, Sigma-Aldrich) and a Pt mesh counter electrode (100 mesh, 99.9% trace metals basis, Sigma-Aldrich) were used for the electrochemical measurements. The cell potentials for the nonaqueous redox species were determined using cyclic voltammetry to compare the solution potential to the formal potential of the redox species. The potential difference between cells was calculated using the difference between the formal potentials for each redox couple in conjunction with standard reduction potentials from the literature. The CH_3CN-$CoCp_2^{+/0}$ solution ($CoCp_2$ [3 mM]/ $CoCp_2^+$ [50 mM]) was calculated to have a solution potential of $E(A/A^-)$ = -1.26 V vs Fc/Fc^+, the CH_3CN-$Fc^{+/0}$ solution (Fc [55 mM]/ Fc^+ [3 mM]) was calculated to have $E(A/A^-)$ = -0.10 V vs Fc^+/Fc, and the CH_3CN-$AcFc^{+/0}$ solution (pre-electrolysis AcFc concentration = [50 mM]) was calculated to have $E(A/A^-)$ = +0.40 V vs

Fc^+/Fc. The nonaqueous electrochemical solutions each contained 1.0 M $LiClO_4$. The aqueous 50 mM $K_3[Fe(CN)_6]$ - 350 mM $K_4[Fe(CN)_6]$ solution contained no additional supporting electrolyte due to the high intrinsic salt concentration. The current under forward bias saturated at much larger values in the $Fe(CN)_6^{3-/4-}$ solution than in the Fc^+/Fc solution due to the increased concentration of electron-accepting species in the $Fe(CN)_6^{3-/4-}$ solution. $Fc[BF_4]$ is a highly colored species that, at high concentrations, absorbs a significant fraction of the light prior to photons striking the photoelectrode. The electrolyte solution was rapidly stirred with a small, Teflon-covered stir bar. Illumination was provided with an ENH-type tungsten-halogen lamp. Illumination intensities were set to provide ~10-11 mA cm^{-2} of light-limited current density. These intensities corresponded to ~1/3rd of a Sun (~33 mW cm^{-2}), respectively, as determined through the concurrent use of a Si photodiode (Thor Laboratories) that was calibrated relative to a secondary standard photodetector that was NIST-traceable and calibrated at 100 mW cm^{-2} of AM1.5G illumination. Nonaqueous electrochemistry was performed anaerobically in an Ar(*g*)-filled glovebox. Aqueous electrochemistry was performed in air. Electrodes were washed with H_2O and dried prior to transfer between electrolyte solutions.

The current density versus potential data in HBr(aq) were measured using a three-electrode setup with a Si working electrode, a Pt wire pseudo-reference electrode, and a large Pt mesh counter electrode. The electrolyte consisted of aqueous 0.4M Br_2 - 7.0 M HBr (pH=0) electrolyte under rapid stirring, and ~33 mW cm^{-2} of simulated solar illumination from an ELH-type W-halogen lamp.

Photoelectrochemical deposition of Pt was performed by immersing the electrode into an aqueous solution of 5 mM K_2PtCl_4 (99.9%, Alfa Aesar) and 200 mM LiCl. Using a three-electrode setup, with a saturated calomel reference electrode and a Pt mesh counter electrode, galvanostatic control was maintained at -0.1 mA/cm^2 in a stirred solution until -100 mC/cm^2 had passed. The samples were then rinsed with deionized water and were dried under a stream of N_2(g).

The stability of the fluorinated graphene was tested under acidic, neutral, and alkaline aqueous solutions, respectively. To insure that the same area was examined before and after testing, a small area on the graphene wafer was outlined with Hysol 9460 epoxy. Optical images along with Raman spectra were acquired, and wafers were then placed for 1 h in aqueous solutions at pH 0, pH 7, and pH 14. After carefully rinsing the samples with >18 MΩ-cm H_2O and drying the samples with a stream of N_2(g), optical images along with Raman spectra were obtained from the same areas as done before testing.

Results

Characterization

Figure 1 shows the x-ray photoelectron spectra and Raman spectroscopy of n-Si/F–Gr samples before and after the final anneal under forming gas. The C 1s region before annealing displayed four peaks at binding energies of 284.8 eV, 285.6 eV, 287.2 eV, and 289.5 eV, attributed to C–C, C=C, C–O, and C–F bonds respectively. The F 1s region displayed two peaks at binding energies of 687.1 eV and 690.0 eV, corresponding to ionic and covalently bound fluorine atoms. The Raman spectra before annealing showed characteristic graphene peaks at 1585 cm^{-1} and 2690 cm^{-1} known as the G and 2D peak respectively. Fluorination also leads to the presence of a prominent defect peak at 1350 cm^{-1}.

After annealing, two additional peaks, at 291 eV and 293.5 eV (inset), attributable to CF_2 and CF_3 groups, were observed in the C 1s XP spectra. The positions of the peaks in the F 1s region were shifted slightly to 686.1 eV and 689.8 eV, respectively, and decreased in size. The defect peak at 1350 cm^{-1} is still visible underneath a new broad peak corresponding to the presence of amorphous carbon on the surface. These spectra are consistent with a lightly fluorinated (C_XF, x>10) graphene surface.[4] The change in fluorination profile after annealing is consistent with a reorganization of the fluorine on the surface, and the XPS spectra demonstrate the expected decrease in fluorine content after a two-hour 350 °C anneal under a H_2:Ar (5:95) atmosphere.[4]

Further characterization after annealing by UV/Visible spectroscopy is shown in Figure 2 for both Gr and F–Gr. Both materials transmit 97% of incoming light on average across the region from 350 nm to 1200 nm. While transmittance decreases at shorter wavelengths for both, no increase indicative of the presence of a bandgap was detected. The small change in transmittance at 800 nm marks the region where the instrument switches the grating used for collection.

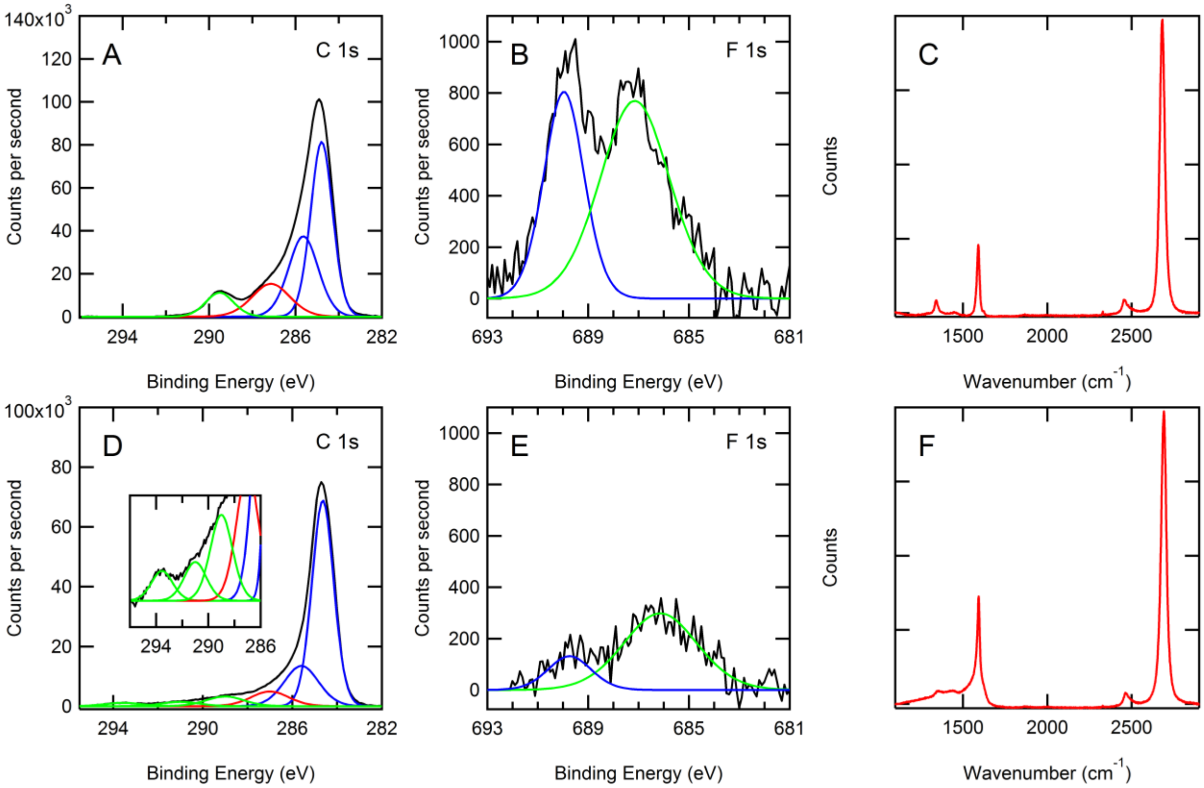

Figure 1. Raman and X-ray photoelectron (XP) spectra of fluorinated graphene (F–Gr) before and after annealing. (A) The C 1s region before annealing. Peaks attributed to carbon bound to fluorine are shown in green; peaks attributed to carbon bound to carbon are shown in blue; and peaks attributed to carbon bound to oxygen are shown in red. (B) The F 1s region before annealing. (C) The Raman spectrum of before annealing. The prominent defect peak is visible at 1350 cm^{-1}. (D) The C 1s region after annealing. Two new CF$_x$ peaks are visible. (E) The F 1s region after annealing. The two peaks are shifted slightly down in energy from the original sample. (F) The Raman spectrum after annealing. The defect peak is visible under a broad peak corresponding to amorphous carbon.

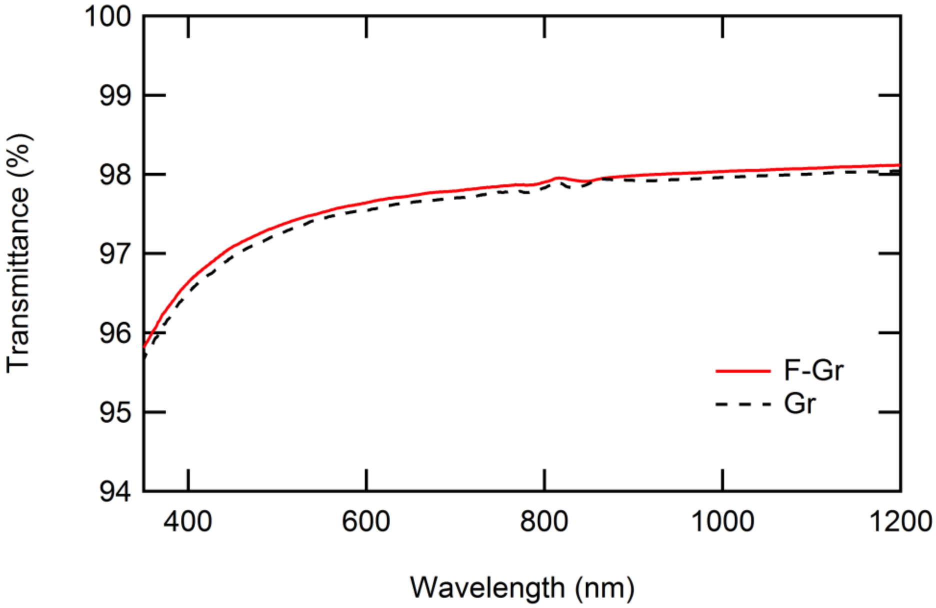

Figure 2. UV/Vis spectra of Gr and F-Gr on glass. Graphene and fluorinated graphene were transferred to borosilicate glass slides using the standard transfer procedures (vide supra).

Electrochemical stability

Figure 3 shows the current-density versus time (*J*-*t*) and current density vs. potential (*J*-*E*) behavior for illuminated (~33 mW cm^{-2} ENH-type W-halogen lamp) n-Si/F–Gr photoanodes in contact with aqueous 50 mM $Fe(CN)_6^{3-}$ - 350 mM $Fe(CN)_6^{4-}$ (aq). The n-Si/F–Gr electrodes exhibited stable current over 100 s while the current density of n-Si–H electrodes decayed to nearly baseline values over the same time period (Figure 3a). Furthermore, the current density of the n-Si/F–Gr electrode decayed by less than 1 mA cm^{-2} for > 100,000 s of continuous operation (Figure 3b). After correcting for fluctuations in the light intensity impinging on the electrode, greater than 97% of the expected current density of an ideally stable electrode was observed. Figure 3c depicts the *J*-*E* behavior before and after exposure to the conditions in Figure 3b. The stable open-circuit potential (-0.27 V vs. $E(A/A^-)$) and fill factor (0.33 before exposure, 0.32 after exposure) show relatively little change in the n-Si/F–Gr interface.

Similar results were observed for np$^+$-Si/F–Gr electrodes (Figure 4). For the np$^+$-Si/F-Gr/$Fe(CN)_6^{3-/4-}$ cell, the following photovoltaic metrics were measured: V_{oc} = -0.39 V, J_{sc} = 11.1 mA cm^{-2}, ff = 0.30. The same degree of stability is seen with no decrease in photocurrent over 100,000 s. Additional data were collected with a Pt catalyst to demonstrate that the fluorinated graphene overlayer did not attenuate the effect of a catalyst on fill factor (Figure 5). For the np$^+$-Si/Pt PV cell, the following photovoltaic metrics were measured: V_{oc} = -0.40 V, J_{sc} = 11.3 mA cm^{-2}, ff = 0.50. The similar V_{oc} values with varying fill factors between these two interfaces suggest that the Si/F-Gr/$Fe(CN)_6^{3-/4-}$ interface is the source of an additional series resistance but that the parallel shunt resistances are similar between the np$^+$-Si/Pt and np$^+$-Si/F-Gr/$Fe(CN)_6^{3-/4}$ interfaces. A similar parallel shunt resistance is also consistent with the use of the same buried photoactive junction at each interface. The np$^+$-Si/Pt PV cell was prepared by evaporating 15 nm of Pt onto the freshly HF etched p^+ surface of an np^+-Si chip and scribing a GaIn eutectic onto the backside of an n-doped surface.

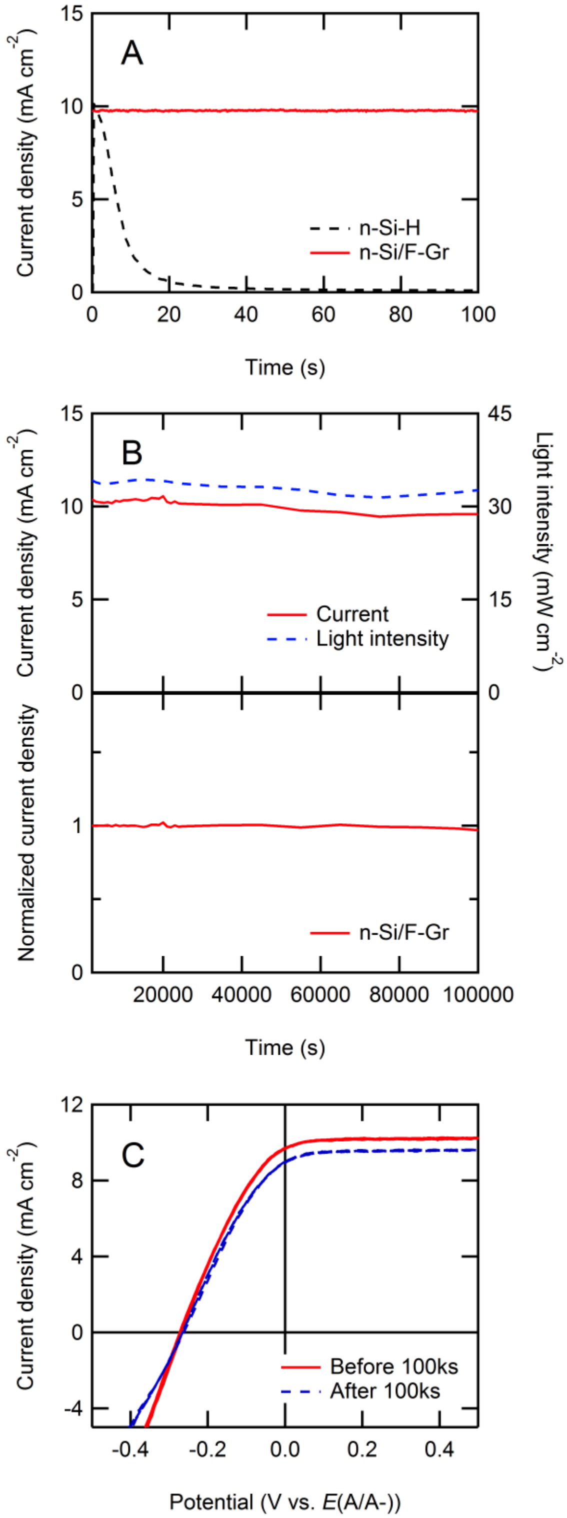

Figure 3. Current density-time (*J*-*t*) and current density-potential (*J*-*E*) behavior of n-Si/F–Gr electrodes in contact with aqueous 50 mM $Fe(CN)_6^{3-}$ - 350 mM $Fe(CN)_6^{4-}$ under ~ 33 mW cm^{-2} of ENH-type W-halogen lamp illumination. (A) Comparison of the *J*-*t* behavior of bare n-Si–H and n-Si/F-Gr electrodes over 100 s. (B) The *J*-*t* behavior of F–Gr covered n-Si at *E*= 0 V vs. the Nernstian potential of the solution (*E*(A/A$^-$)) over 100,000 s (>24 hours). The normalized current density is reported to correct for any variation in the intensity of the light source with time. (C) *J*-*E* behavior of n-Si/F–Gr (3 scans at 50 mV s^{-1}) before and after exposure to the conditions

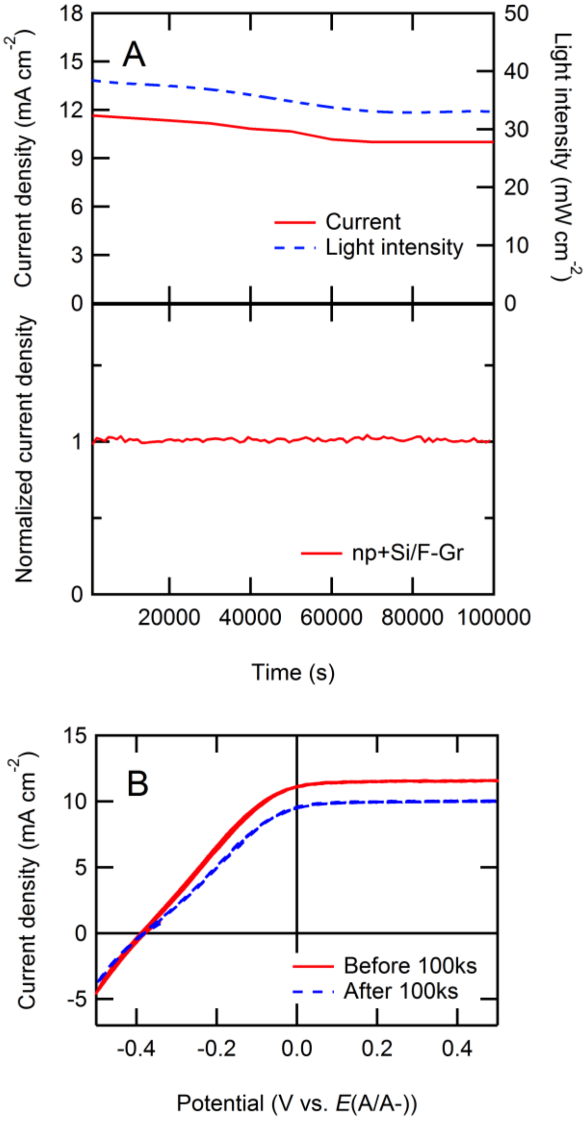

Figure 4. Current density vs. time (J-t) and current density vs potential (J-E) behavior of np+-Si/F–Gr electrodes in contact with aqueous 50 mM Fe(CN)$_6^{3-}$ - 350 mM Fe(CN)$_6^{4-}$ electrolyte under ~33 mW cm-^{2} of ENH-type W-halogen illumination. (A) The J-t behavior of np+-Si/F–Gr at E= 0 V vs. E(A/A-) over 100,000 s (>24 h). The normalized current density is reported to correct for any variations in the light intensity during the experiment. (B) J-E behavior of np+-Si/F–Gr (3 scans at 50 mV s^{-1}) before and after exposure to the conditions depicted in (A). The current density decay in the original chronoamperograms is consistently ascribed to fluctuations in the light source, as well as to decomposition of the Fe(CN)$_6^{3-/4-}$ under illumination, which produced thin colored film on the electrochemical cell over the course of the experiment depicted in (A).

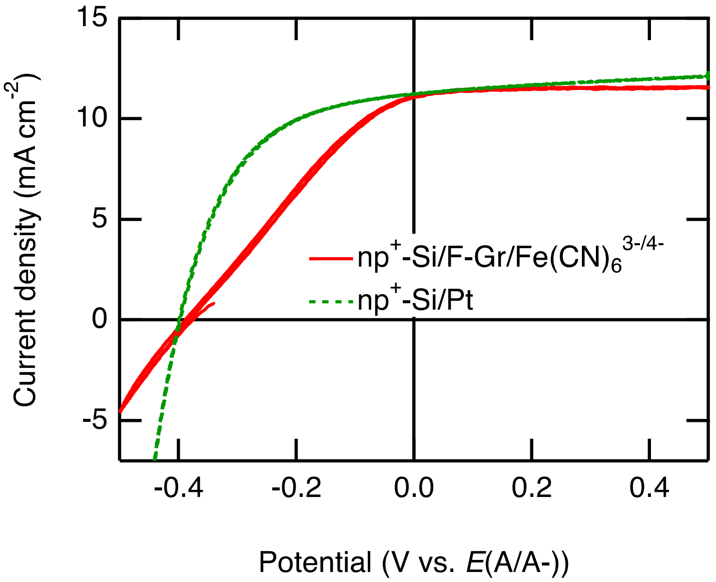

Figure 5. *J-E* behavior of an np$^+$-Si/Pt PV cell and an np$^+$-Si/F-Gr/Fe(CN)$_6^{3-/4-}$ photoanode under ~33 mW cm^{-2} of ENH-type W-halogen illumination. For this cell, the (E(A/A$^-$)) referenced on the x-axis refers to the potential of the Pt contact.

Table 1. $|V_{oc}|$ values for n-Si/Gr and n-Si/F–Gr electrodes in contact with non-aqueous redox couples under ~33 mW cm^{-2} of W-halogen illumination. The Nernstian potential, $E(A/A^-)$, of the contacting non-aqueous electrolytes were measured as follows: $E(CoCp_2^{+/0})$ = -1.26 V vs. $E°'(Fc^{+/0})$, $E(Fc^{+/0})$ = -0.1 V vs. $E°'(Fc^{0/+})$, $E(AcFc^{+/0})$ = +0.4 V vs $E°'(Fc^{+/0})$.

	$|V_{oc,CoCp2+/0}|$ (V vs. $E(CoCp_2^{+/0})$)	$|V_{oc,Fc+/0}|$ (V vs. $E(Fc^{+/0})$)	$|V_{oc,AcFc+/0}|$ (V vs. $E(AcFc^{+/0})$)
Gr	0	0.26	0.43
F–Gr	0	0.20	0.30

The behavior of n-Si/Gr and n-Si/F–Gr in contact with a series of non aqueous, one-electron redox couples spanning a range of potentials is shown in Table 1. The n-Si/Gr samples consistently showed no photovoltage in contact with cobaltocene ($CoCp_2^{+/0}$, -1.26 V vs. $E°'(Fc^{+/0})$) and increasing values for photovoltage in contact with more positive couples, such as ferrocene ($Fc^{+/0}$, -0.1 V vs. $E°'(Fc^{0/+})$) and acetylferrocene ($AcFc^{+/0}$, +0.4 V vs $E°'(Fc^{+/0})$). The same trend was observed for the n-Si/F–Gr samples, although the photovoltages were attenuated from those of the n-Si/Gr samples.

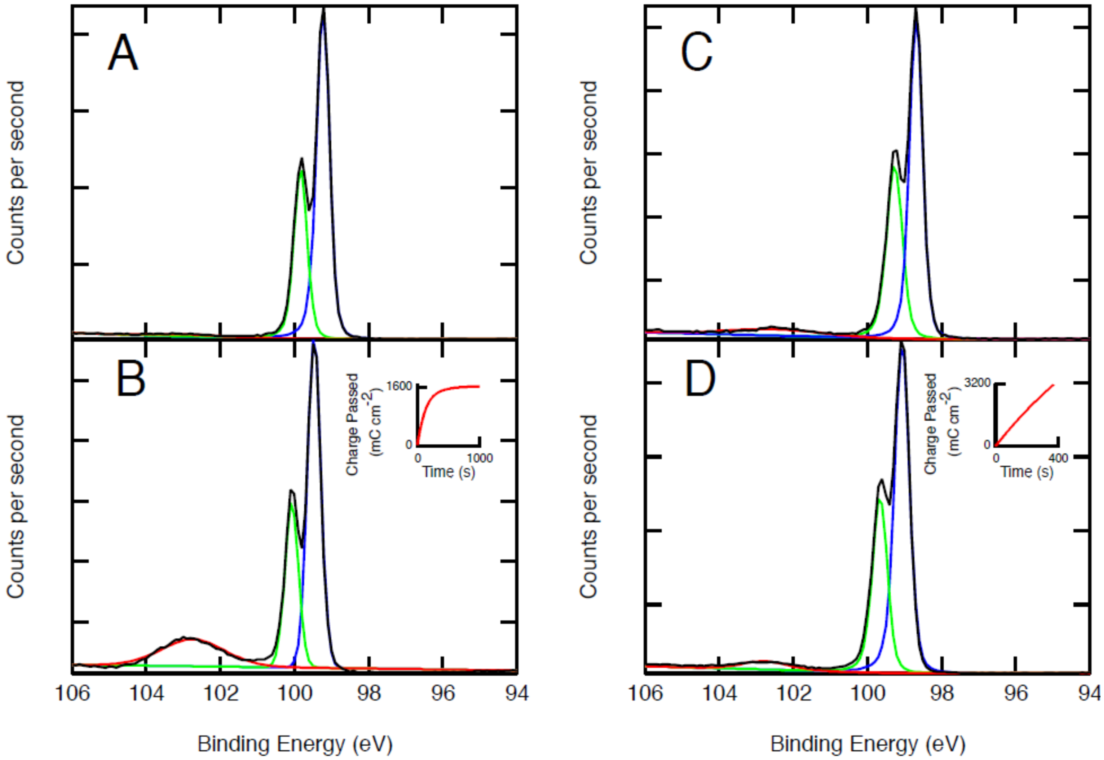

Figure 6. XP spectra of n-Si–Me and n-Si–Me/F–Gr electrodes. (A) and (B) show the XP spectra of an n-Si–Me electrode before and after passing 1600 mC cm^{-2} (inset) while passing anodic current in contact with an aqueous 50 mM $Fe(CN)_6^{3-}$ - 350 mM $Fe(CN)_6^{4-}$ electrolyte. (C) and (D) show an n-Si–Me/F–Gr electrode before and after passing 3200 mC cm^{-2} under similar electrochemical conditions to (A) and (B).

Figure 6 shows a comparison of the XP spectra of methyl-terminated n-Si electrodes (n-Si–Me) with and without a F–Gr protective layer before and after photoelectrochemical testing in an aqueous 50 mM $Fe(CN)_6^{3-}$ - 350 mM $Fe(CN)_6^{4-}$ electrolyte. After passing 1600 mC cm^{-2} of anodic charge on an n-Si-Me electrode, the growth of an oxide peak was observed in the Si 2p XPS region. In contrast, no additional growth of the oxide peak was observed after passing twice the number of Coulombs (3200 mC cm^{-2}) across an n-Si–Me/F–Gr electrode.

XPS analysis was performed in order to determine the effect of electrochemical oxidation at the Si–Me surface on the oxidation state of the Si photoanode surface (Figure 6). Silicon oxide detected before and after electrochemical oxidation was quantified using a simple substrate—overlayer model described by equation 1:[8]

$$d = \lambda_{ov} \sin\theta \left\{ \ln\left[1 + \frac{I_{Si}^{o}}{I_{ov}^{o}} * \frac{I_{ov}}{I_{Si}}\right]\right\} \tag{1}$$

Where d is the overlayer thickness, λ_{ov} is the attenuation factor through the oxide overlayer (assumed to be 2.6 nm)[9], θ the angle from the surface of the sample to the detector (90°), $\frac{I_{Si}^{o}}{I_{ov}^{o}}$ is an instrument normalization factor related to the expected signal for a pure Si and a pure SiO_2 sample (taken to be 1.3 for this instrument), I_{ov} is the measured intensity of the silicon, and I_{ov} is the measured intensity of the silicon oxide overlayer. The thickness of a monolayer of oxide was taken to be 0.35 nm.[10] Negligible silicon oxide was detected on the bare methyl-terminated silicon surfaces prior to electrochemical oxidation (Figure 6a) and an oxide thickness of approximately 0.75 nm, or >2 monolayers of oxide, was observed after exposure of the Si–Me surface (Figure 6b) to the electrochemical oxidation conditions described in Figure 6. An oxide thickness of approximately 0.15±0.05 nm was detected on the Si–Me/F–Gr surfaces prior to electrochemical oxidation (Figure 6c) and an oxide thickness of approximately 0.17± 0.5 nm, was observed after exposure (Figure 6d) of the Si–Me/F–Gr surface to the electrochemical oxidation conditions described in Figure 6. Hence, F–Gr acts as a physical barrier to oxide formation, preserving the photoelectrochemical behavior of the n-Si-Me/solution interface. Methylated surfaces were used because, in contrast with n-Si–H surfaces, the n-Si–Me surface does not easily oxidize in air or form significant oxide upon fabrication of n-Si/F–Gr interfaces, allowing more facile observation of oxide growth in the presence of various protective layers, such as F–Gr.

The photoelectrochemical stability of pristine graphene-coated n-Si electrodes and of fluorinated graphene-coated electrodes was compared by collecting *J*-*t* data for n-Si/Gr and n-Si/F–Gr electrodes from four different electrode 'batches' (two n-Si/Gr and two n-Si/F–Gr batches) in contact with aqueous 50 mM $Fe(CN)_6^{3-}$- 350 mM $Fe(CN)_6^{4-}$ under ~33 mW cm^{-2} of ENH-type W-halogen illumination (Figure 8). These batches of electrodes each mutually consisted of 5-6 electrodes in which each electrode was fabricated from the same section of a larger sheet of Gr or F–Gr, respectively. However, between batches of electrodes, different PMMA/(F–)Gr/Cu stacks or different regions of the same stack were used. The n-Si/Gr from the first graphene electrode batch (batch Gr_A) exhibited stable current densities for > 1000 s (Figure 8a). Among these electrodes fabricated, all five electrodes were photoelectrochemically stable (5/5 stable, where stability was defined as having a current density at *t*=1000 s of at least 60% of the current density displayed at *t*=0 s). This definition was used because some graphene-

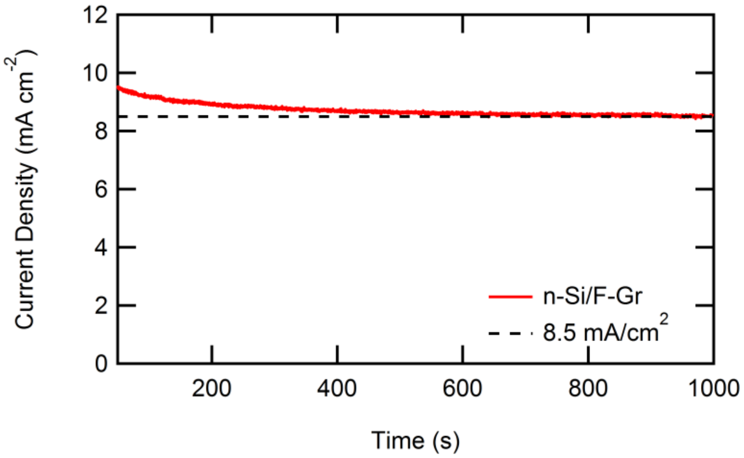

Figure 7. Representative J-t data of an n-Si/F–Gr electrode in contact with aqueous 50 mM $Fe(CN)_6^{3-}$ - 350 mM $Fe(CN)_6^{4-}$ under ~33 mW cm^{-2} of W-halogen illumination. After an initial decay in current density, the current density stabilized at ~8.5 mA cm^{-2}.

covered (and F–Gr covered) electrodes displayed an initial decay of current density followed by a subsequent stabilization, as seen in Figure 7. This behavior is consistent with the hypothesis that any pinholes in the graphene protective coating led to the oxidation at the exposed Si surface, but that stability is observed when the exposed Si is passivated with SiO_x. However, the other batch (batch Gr_C, Figure 8c) yielded only two n-Si/Gr electrodes out of six that exhibited stable current densities for > 1000 s (2/6 stable). The inconsistent behavior in the photoelectrochemical stability imparted by pristine graphene coatings on n-Si electrode was observed over many iterations of graphene growth and electrode fabrication. Conversely, both batches of F–Gr coated n-Si electrodes (batch F–Gr_B, Figure 8b and batch F–Gr_D, Figure 8d) yielded n-Si/F–Gr electrodes that exhibited stable current densities for > 1000 s (5/5 stable in batch F–Gr_B and 5/5 stable in batch F–Gr_D). Figure 9 shows the behavior of occasional ‘champion’ electrodes that could be fabricated from Gr or F–Gr with stability over 100,000 s. The improved consistency of the photoelectrochemical stability is one of the key attributes of the fluorinated graphene-coated n-Si electrodes relative to the routinely observed behavior of pristine graphene-coated n-Si electrodes.

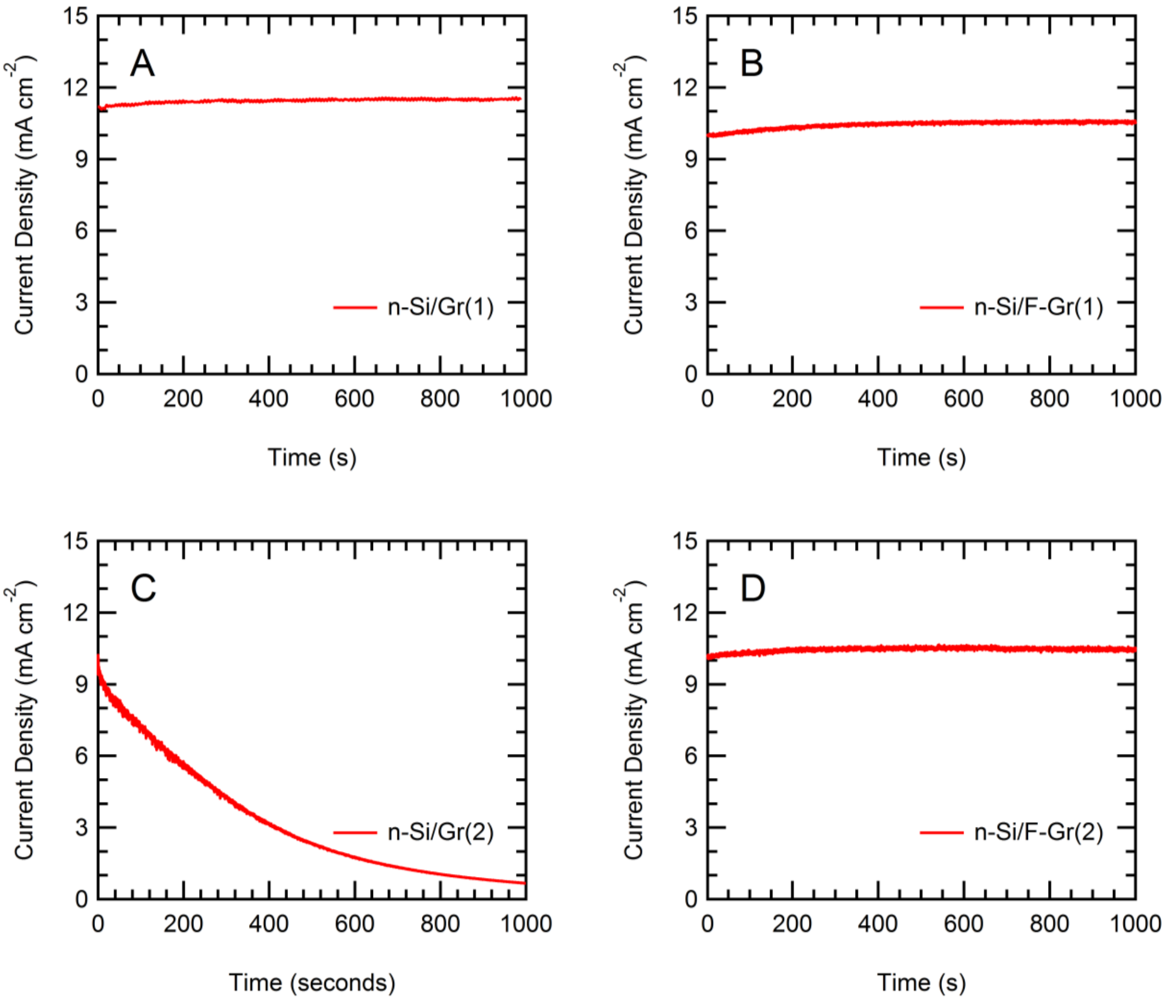

Figure 8. J-t data for n-Si/Gr and n-Si/F–Gr electrodes from two different Gr growths in contact with aqueous 50 mM $Fe(CN)_6^{3-}$ - 350 mM $Fe(CN)_6^{4-}$ under ~33 mW cm^{-2} of W-halogen illumination. (A) The n-Si/Gr from the first Gr sheet (growth 1) exhibited stable current densities for > 1000 s. (B) Fluorination of Gr from growth 1 yielded n-Si/F–Gr electrodes that exhibited stable current densities for > 1000 s. (C) Another Gr growth (growth 2) yielded n-Si/Gr electrodes that did not exhibit stable current densities for > 1000 s. (D) When Batch 2 was fluorinated, the n-Si/F–Gr electrodes exhibited stable current densities for > 1000 s.

Fluorinated graphene-coated and pristine graphene-coated n-Si electrodes were tested for photoelectrochemical stability under approximately 1 sun conditions (~100 mW cm^{-2} from an ENH-type W-halogen lamp). Figure 10a depicts the photoelectrochemical stability over 1000 s for n-Si/Gr and n-Si/F–Gr electrodes in contact with aqueous 50 mM Fe(CN)$_6^{3-}$ - 350 mM Fe(CN)$_6^{4-}$ under ~100 mW cm^{-2} of W-halogen illumination. The current density of the n-Si/F–Gr electrode was effectively constant over this time period, whereas the current density of the n-Si/Gr electrode decayed from ~25 mA cm^{-2} to less than 7 mA cm^{-2} over the same time period. This behavior supports the hypothesis that under these conditions fluorinated graphene provides a superior protective layer relative to pristine graphene. Figure 10b further depicts the photoelectrochemical stability under

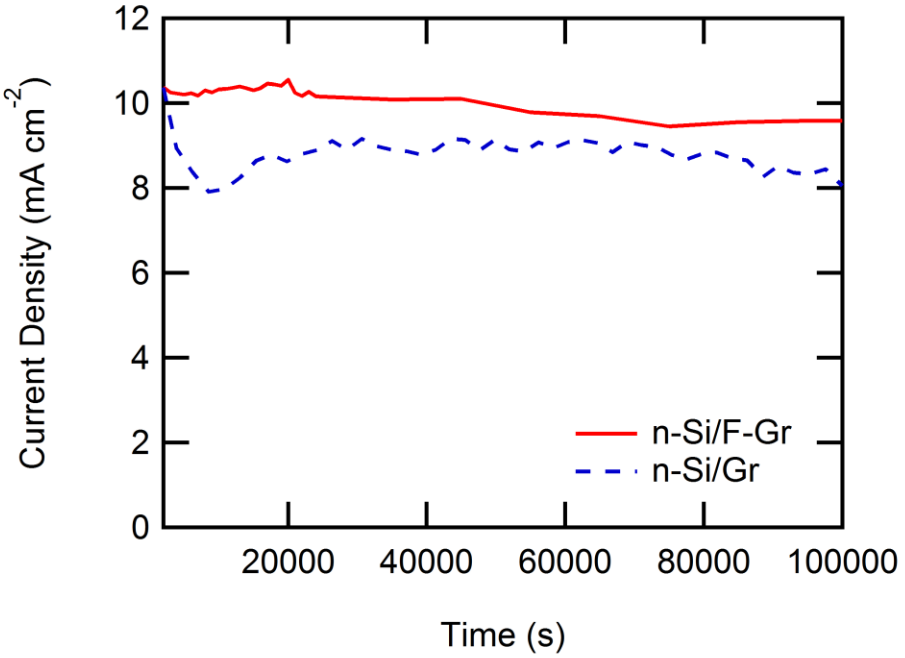

Figure 9. J-t data of the ‘champion’ n-Si/F–Gr and n-Si/Gr electrodes in contact with aqueous 50 mM Fe(CN)$_6^{3-}$ - 350 mM Fe(CN)$_6^{4-}$ under ~33 mW cm^{-2} of W-halogen illumination. After both starting at an initial current density of ~10 mA cm^{-2}, the n-Si/F–Gr electrode current density decayed to 9.5 mA cm^{-2} compared to the n-Si/Gr electrode which decayed to 8 mA cm^{-2}.

the same conditions of a F–Gr coated n-Si electrode over 100,000 s. Although the F–Gr coated electrode was stable over the same time period (100,000 s) under lower light intensity conditions (Figure 3), at near 1 sun conditions the current density of the electrode decayed to near baseline conditions over the same time period.

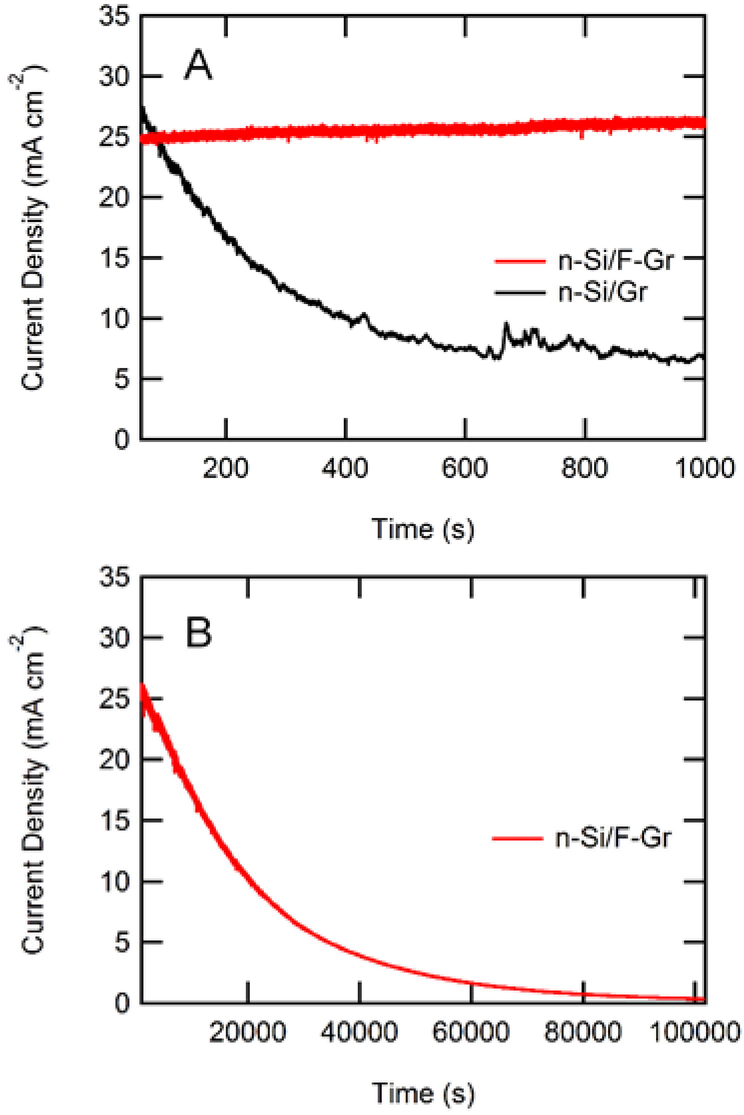

Figure 10. J-t data for n-Si/Gr and n-Si/F–Gr electrodes in contact with aqueous 50 Mm $Fe(CN)_6^{3-}$ - 350 mM $Fe(CN)_6^{4-}$ under ~100 mW cm^{-2} of W-halogen illumination (A) over 1000 s and (B) a n-Si/F–Gr electrodes under the same conditions over 100,000 s.

Chemical stability

The Raman spectra and optical images of the samples soaked in acidic and neutral solutions showed no change after testing (Figure 11-12). The samples tested in alkaline solutions showed a marked decrease in defect density of the remaining sections of fluorinated graphene, closely mimicking the profile of pristine graphene. Repeated tests of fluorinated graphene in 1 M KOH(aq) showed large-scale delamination of the fluorinated graphene sheet, as observed in the images before and after exposure to the aqueous pH 14 solution.

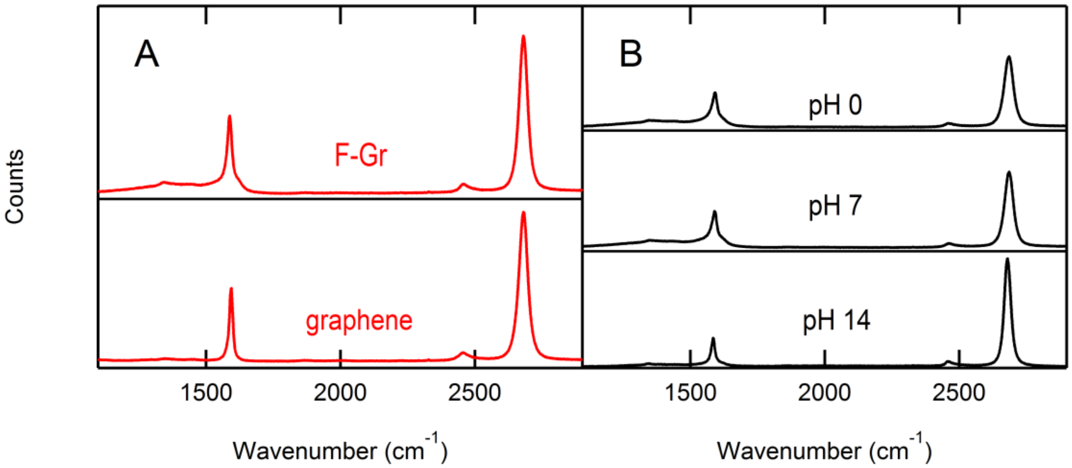

Figure 11. Stability tests of F–Gr in acidic (1 M HCl), alkaline (1 M KOH), and neutral (deionized water) conditions. An initial Raman of the pristine graphene sheets before fluorination and after fluorination showed an increase in the size of the defect peak at 1350 cm^{-1}. This defect peak remained unchanged after 1 h in acidic or neutral solutions. In contrast, immersion for 1 h in alkaline media produced a decrease in the density of the defect peak.

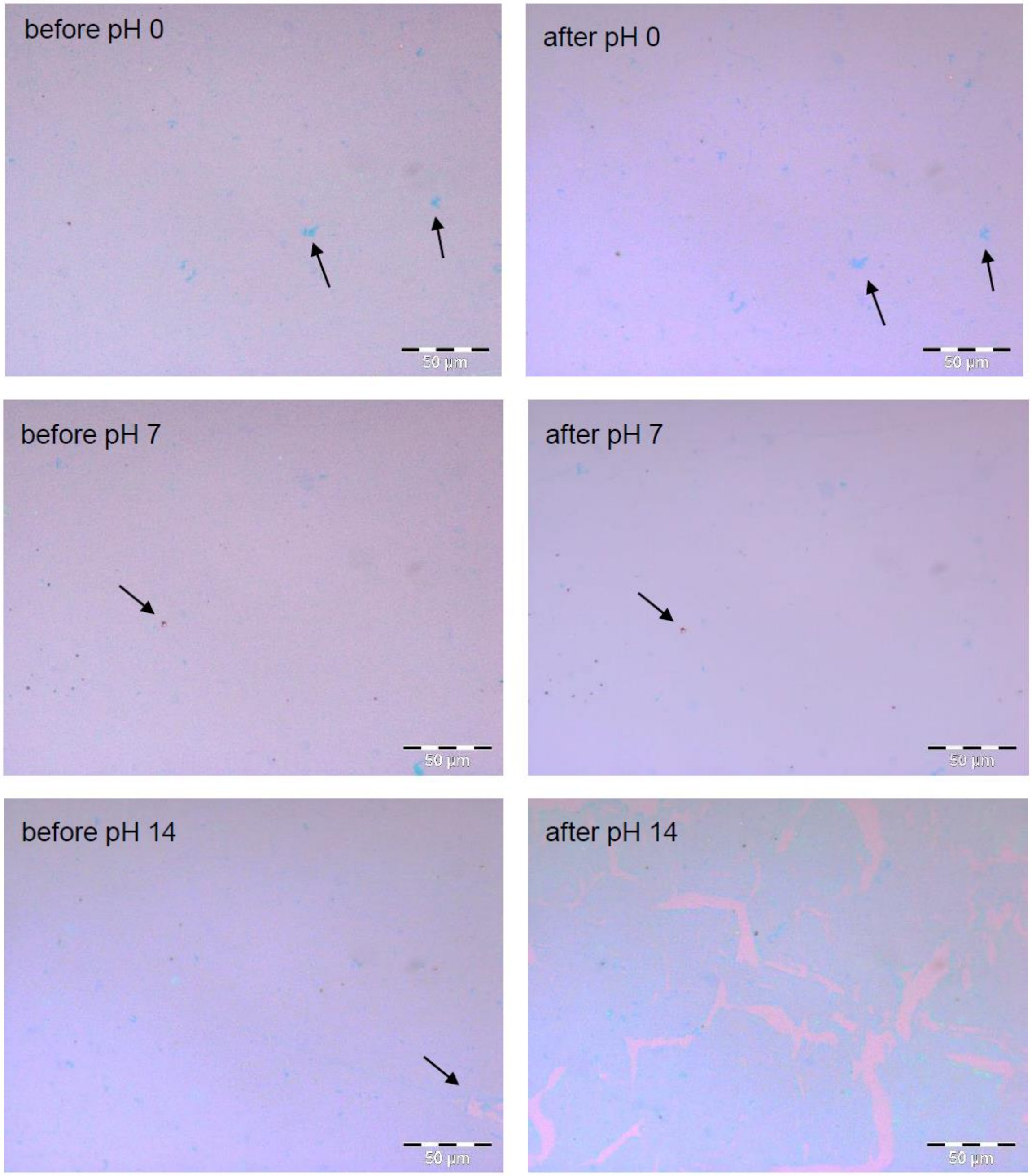

Figure 12. Optical images of stability tests of F–Gr in acidic (1 M HCl), alkaline (1M KOH), and neutral (deioninzed water) conditions. Arrows indicate points of reference for the corresponding before and after images.

The chemical stability of the F–Gr to the formation of silicide was also probed. XP spectra of Si-Me/F-Gr/Pt and Si-Me/Pt surfaces were obtained to investigate the ability of F-Gr to inhibit platinum silicide formation (Figure 13). Pt was deposited at ~3 nm thickness via electron-beam evaporation on both F-Gr covered and bare Si surfaces. The 3 nm Pt thickness was chosen to allow for interrogation of the sample surface to a depth at which both Si and Pt ware observable by XPS. Methylated Si surfaces were used to inhibit the formation of Si oxide at the Si/Pt interface during sample fabrication, because Si oxide of sufficient thickness is also capable of preventing silicide formation.[5] Figure 13a shows the XP spectrum of a pure Pt phase. A thicker Pt layer (20 nm) was used to interrogate only the pure Pt phase. Figure 13b shows the Pt 4f XP spectrum of CH_3-terminated Si with a 3 nm Pt overlayer. The Pt 4f peak shifted to higher binding energy, indicative of platinum silicide formation.[6] The shoulder of the peak at low binding energy is consistent with a pure Pt phase overlayer. Conversely, 3 nm of Pt on F-Gr covered silicon showed essentially no change in the Pt 4f binding energy immediately after fabrication (Figure 13c or after a 1 h anneal under forming gas at 300 °C (Figure 13d)). Figure 13e presents an overlay of the spectra in Figure 13a-13d and highlights the difference between the Pt 4f peak positions. The data are thus indicative of little or no platinum silicide formation.

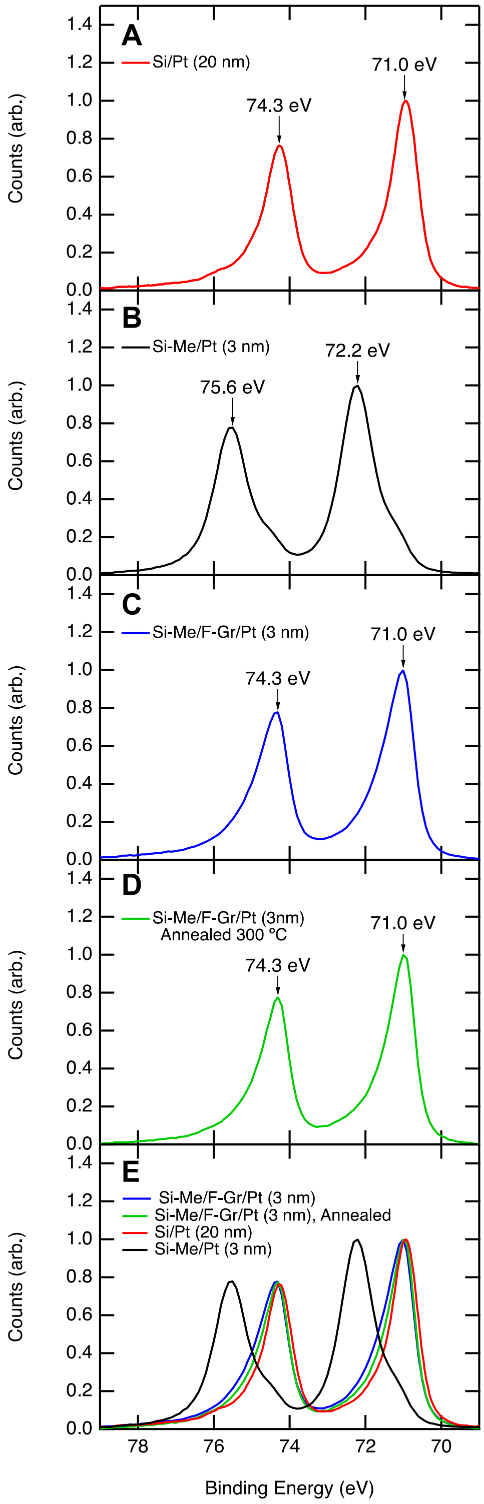

Figure 13. The Pt 4f XP spectra of Pt on both F-Gr covered and Si surfaces. (A) XP spectrum of a thick (20 nm) layer of Pt on Si. This spectrum is representative of a pure Pt phase. (B) XP spectrum of a 3 nm layer of Pt on Si. The Pt 4f peak shifted to high binding energy (72.2 and 75.6 eV), characteristic of platinum silicide formation.[6] The shoulder to lower binding energy is attributed to a pure Pt phase. (C) XP spectrum of Si-Me/F-Gr/Pt (3 nm). The Pt 4f peak positions (71.0 and 74.3 eV) are consistent with pure Pt. (D) XP spectrum of Si-Me/F-Gr/Pt after annealing at 300 °C under forming gas. (E) Overlay of XP spectra (A)-(D).

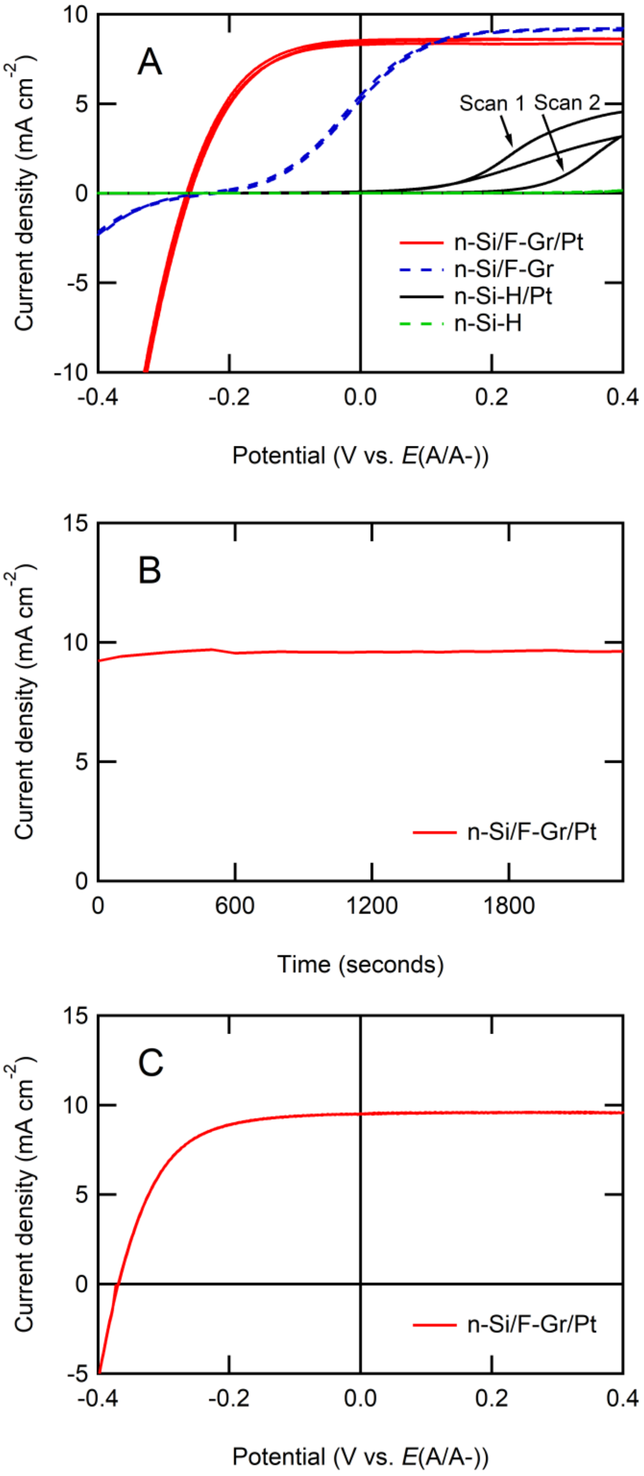

Figure 14. Electrochemical behavior of n-Si/F–Gr and n-Si–H electrodes with and without Pt deposition in aqueous 0.4 M Br$_2$ – 7.0 M HBr (pH=0) electrolyte under 33 mW cm^{-2} from an ELH-type W-halogen lamp). (A) J-E behavior of n-Si/F–Gr and n-Si–H electrodes with and without Pt deposition. Each cyclic voltammogram was started at +0.4 V vs. E(A/A$^-$) and swept twice to more negative potentials at 50 mV s^{-1}. (B) J-t behavior of an n-Si/F–Gr/Pt electrode over 45 minutes at E=0 V vs. E(A/A$^-$) (C) J-E behavior of an n-Si/F–Gr/Pt electrode after exposure to conditions described in (B).

Figure 14 displays the *J-E* behavior of n-Si–H and n-Si/F–Gr electrodes under ~33 mW cm^{-2} illumination intensity in contact with 0.4 M Br_2 – 7.0 M HBr (pH=0), with and without electrochemical deposition of 100 mC cm^{-2} of a Pt catalyst, respectively. With the Pt catalyst, the properties of the n-Si/F–Gr/Pt electrode improved to V_{oc} (n-Si/F–Gr/Pt) = 0.26 V, *ff* = 0.52, and J_{sc} = 8.3 mA/cm^2 from V_{oc} (n-Si/F–Gr) = 0.22 V, *ff* = 0.16, J_{sc} = 5.14 mA cm $^{-2}$. The improved *ff* can be ascribed to improved catalysis for the Br^- to Br_2 reaction effected by the Pt. The current density of the n-Si–H/Pt electrode under illumination decayed precipitously over two potential sweeps, while the n-Si/F–Gr/Pt electrode showed a stable *ff* and photocurrent density under the same conditions. The n-Si/F–Gr/Pt electrode had an ideal regenerative cell efficiency (η_{IRC}) of 3.5% in contact with the Br_2/HBr (aq) electrolyte.[33] The current density at n-Si/F-Gr/Pt electrodes was stable over 45 min at *E*=0 V vs. the Nernstian potential of the solution, *E*(A/A^-) and η_{IRC} increased to 5% over this time (Figure 15). The improvement in η_{IRC} indicates a change in the energetics of the n-Si/F–Gr/Pt interface after electrochemical deposition of Pt.

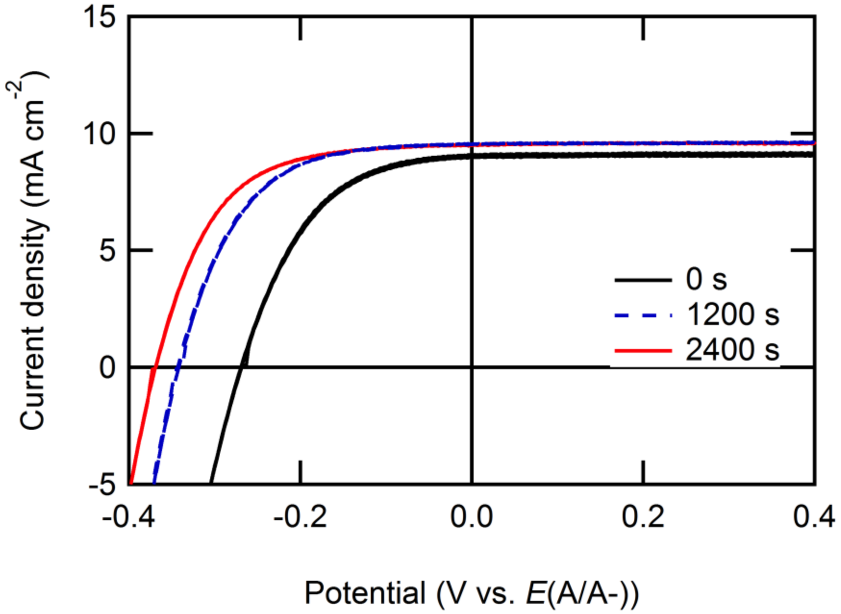

Figure 15. Current density-potential (*J*-*E*) behavior of an n-Si/F-Gr/Pt photoanode before, during, and after 2400 s of photoelectrochemical stability testing in contact with 0.4M Br_2 - 7.0 M HBr (pH=0) aqueous electrolyte. Photoelectrochemical stability was measured by observing the *J*-*t* behavior at an initial current density of 10 mA cm^{-2} over the specified time period (see Figure 14). The behavior of the n-Si/F-Gr/Pt electrode improved over 2400 s, with improvements in V_{oc} (0.27 V to 0.37 V), J_{SC} (9.0 mA to 9.5 mA), and *ff* (0.51 to 0.59), resulting in an increase in the ideal regenerative cell conversion efficiency rom 3.5% to >5%.

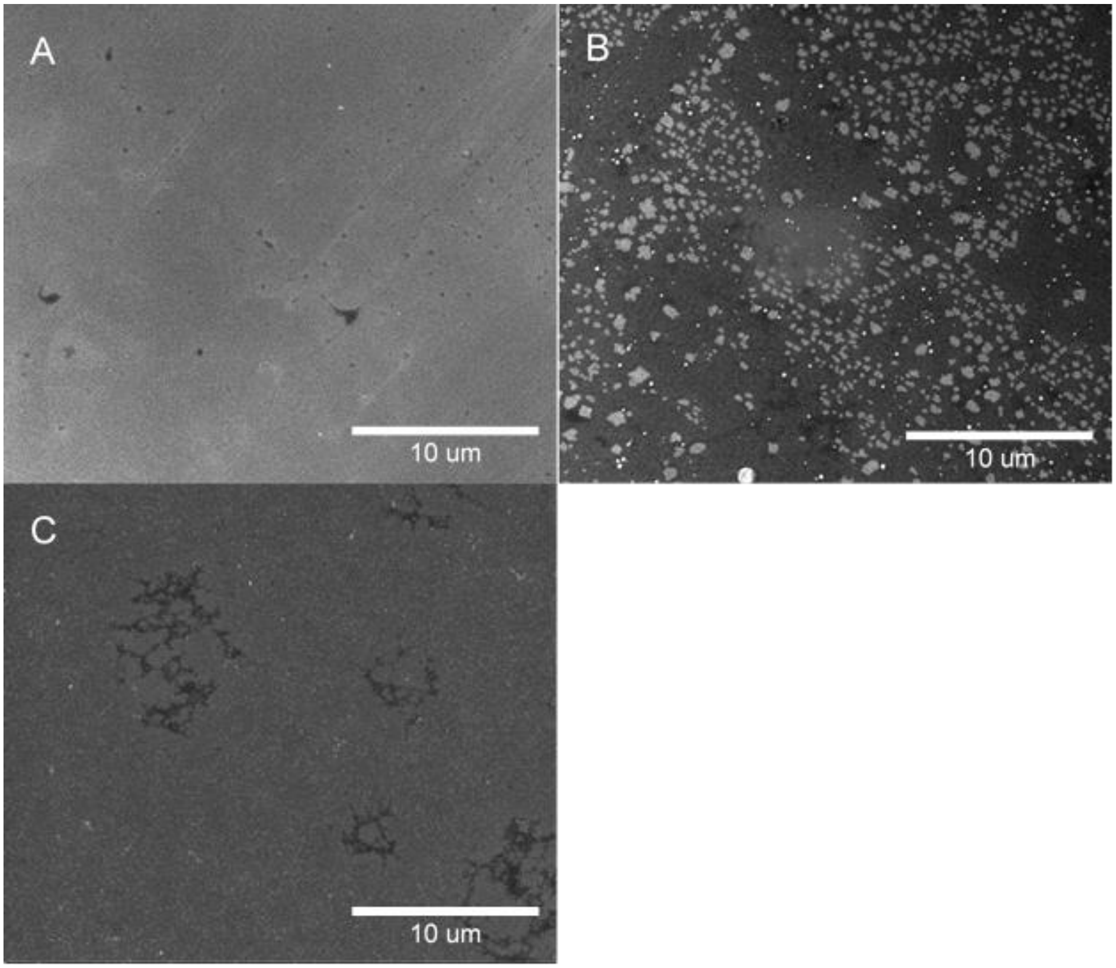

Figure 16. SEM of fluorinated graphene before and after photoelectrochemical deposition of Pt metal from an aqueous solution of 5 mM K_2PtCl_4 and 200 mM LiCl. A) SEM image of a fluorinated graphene-covered n-Si surface prior to deposition. B) SEM image of a fluorinated graphene-covered n-Si surface after passing 10 mC cm^{-2} charge during deposition. C) SEM image of a fluorinated graphene-covered n-Si surface after passing 100 mC cm^{-2} charge during deposition.

Assuming 100% faradaic yield for charge transfer to platinum during the photoelectrochemical deposition of Pt from an aqueous solution of 5 mM K_2PtCl_4 and 200 mM LiCl, in conjunction with 2 e- per Pt atom deposited, and a conformal deposition, a charge density of -100 mC cm^{-2} should result in the deposition of a ~50 nm thick of Pt layer on the nSi/F–Gr electrodes. SEM images were obtained on n-Si/F–Gr surfaces before photoelectrochemical deposition and after 10 mC cm^{-2} or 100 mC cm^{-2} of cathodic charge density was passed during electrodeposition (Figure 16). Figure 16 indicates that the Pt deposited stochastically across the F–Gr surface. This deposition stands in contrast to previous reports of metal deposition via other methods on graphene, which produced preferential metal deposition at grain boundaries. This difference in behavior may be due to passivation of highly reactive grain boundary sites by the XeF_2 treatment. The incomplete electrochemical stability observed in Figure 14 for the n-SiH/Pt electrode may be related to imperfect conformal deposition, consistent with the observations of Figure 16.

Discussion

A key hypothesis of this work is that the fluorination of CVD-grown graphene leads to passivation of defect sites present in CVD graphene. Assuming a carbon-carbon bond length of 0.142 nm and the hexagonal structure of graphene, the area of each hexagonal unit in a graphene sheet is 0.052 nm^2 and encompasses two carbon atoms. Therefore, a 1 cm^2 sheet of pristine graphene will include ~ $1x10^{15}$ carbon atoms. A rigorous evaluation of the density and total number of carbon atoms in a polycrystalline graphene sheet is challenging, due to the presence of a variety of defect types, including point and line defects, with various geometries, and also due to a variable number of defects that may be produced by fabrication of the graphene-covered electrode. For simplicity, we consider only the line defects associated with grain boundaries. These line defects have a variety of geometries and can be composed of alternating 5- and 7- membered carbon rings. Assuming that the density of carbon atoms at a line defect and in the defect-free graphene sheet are equivalent, and further that the density of carbon atoms in a polycrystalline CVD graphene sheet is equivalent to that in a single crystalline graphene sheet, allows calculation of the percentage of total carbon atoms at defect sites in the graphene sheet. The grain size of the graphene used in this work is 0.2-5 μm on a side. The grains are generally amorphously shaped, but are approximated herein as hexagons for simplicity. Assuming hexagonal grains with side length of 0.2 μm (area of 0.10 μm^2) implies ~10^9 grains in a 1 cm^2 sheet of graphene, and a total length of 8 x 10^8 μm of grain boundary area. If the width of these boundaries is equal to the width of a single hexagonal unit of the graphene lattice (~0.28 nm), and assuming that the carbon density is the same as that of a single hexagonal unit, the total number of defect carbon atoms at grain boundary line defects is ~10^{10}C atoms per 1 cm^2 area of graphene. Thus (10^{10} /10^{15}), i.e., 1 defective carbon atom is present for every 10^5 pristine carbon atoms in the polycrystalline graphene sheet. This ratio is significantly smaller than the ratio of F atoms to C atoms found via XPS analysis (10 > F/C > 0.01). In conjunction with the expectation that the defect sites on a graphene sheet are significantly more reactive than the pristine carbon sites, this XPS F/C ratio suggests that most or all of the defect carbon atoms are capped with fluorine.

Prior to the stability test, the open-circuit potential (V_{oc}) of the n-Si/F–Gr electrode was -0.27 V vs. $E(A/A^-)$, approximately 70 mV lower than the reported V_{OC} of -0.34 V vs. $E(A/A^-)$ for n-Si coated with a single layer of graphene.[22] Further, exposure of n-Si/F-Gr to a series of non-aqueous electrolytes of varying electrochemical potential showed a dependence of V_{oc} on $E(A/A^-)$, indicating partial Fermi level pinning of the n-Si surface with respect to the solution potential (Table 1). The mutually similar fill factors (*ff*) the n-Si/F–Gr electrode and np^+-Si/F–Gr electrodes, 0.33 and 0.30, respectively (Figure 3c, Figure 4c), indicated similar limiting resistance to charge transfer in both systems.

Additional tests of the chemical stability demonstrate that F-Gr is also an effective barrier against other deleterious surface reactions. F-Gr covered Si surfaces did not form platinum silicide upon evaporation of Pt onto the F–Gr/Si surface, and F–Gr is stable in both aqueous and acidic (pH 0) solutions, suggesting F–Gr also provides an effective physical barrier to inhibit Pt/Si reactivity and is stable under harsh fabrication and electrolyte conditions. Although only lightly fluorinated (C_xF, $x > 10$) graphene was used herein, these fluorinated graphene sheets provided superior protection against corrosion to the underlying Si relative to the protection imparted by monolayer graphene on n-Si(111) photoanodes (Figure 8).[22] These results are consistent with the hypothesis that light fluorination of graphene induces reaction with high-energy defect sites, such as dangling bonds or missing atoms, effectively sealing defects that otherwise would allow oxide formation at the n-Si surface and further degradation of the Gr protective layer. The bonding of a very electronegative atom to the surface may also increase the hydrophobicity of the graphene sheet, which would further reduce deleterious corrosion reactions near pinholes.

Conclusion

Fluorinated graphene forms an effective physical barrier between silicon surfaces and a number of contacting phases, including acidic and neutral pH aqueous electrolyte as well as metallic interfaces. Additionally, Si covered by fluorinated graphene exhibits partial Fermi level pinning in contact with non-aqueous electrolytes. Additional work at higher fluorination levels on both p-type and n-type silicon will elucidate whether a reduction in the density of states near the Fermi level can lead to a fully unpinned interface, and will allow elucidation of the effect of the graphene-based surface dipole on the electrochemical behavior of the resultant photoelectrode.

References

1. Hu, S.; Lewis, N. S.; Ager, J. W.; Yang, J.; McKone, J. R.; Strandwitz, N. C., Thin-Film Materials for the Protection of Semiconducting Photoelectrodes in Solar-Fuel Generators. *J. Phys. Chem. C* **2015,** *119* (43), 24201-24228.

2. Sun,
K.; Shen, S.; Liang, Y.; Burrows, P. E.; Mao, S. S.; Wang, D., Enabling Silicon for Solar-Fuel Production. *Chem. Rev.* **2014,** *114* (17), 8662-8719.

3. Sun, K.; McDowell, M. T.; Nielander, A. C.; Hu, S.; Shaner, M. R.; Yang, F.; Brunschwig, B. S.; Lewis, N. S., Stable Solar-Driven Water Oxidation to O2(g) by Ni-Oxide-Coated Silicon Photoanodes. *J. Phys. Chem. Lett.* **2015,** *6* (4), 592-598.

4. Hu, S.; Shaner, M. R.; Beardslee, J. A.; Lichterman, M.; Brunschwig, B. S.; Lewis, N. S., Amorphous TiO2 coatings stabilize Si, GaAs, and GaP photoanodes for efficient water oxidation. *Science* **2014,** *344* (6187), 1005-1009.

5. Strandwitz, N. C.; Comstock, D. J.; Grimm, R. L.; Nichols-Nielander, A. C.; Elam, J.; Lewis, N. S., Photoelectrochemical Behavior of n-type Si(100) Electrodes Coated with Thin Films of Manganese Oxide Grown by Atomic Layer Deposition. *J. Phys. Chem. C* **2013,** *117* (10), 4931-4936.

6. Bélanger, D.; Dodelet, J. P.; Lombos, B. A., Characteristics and Stability of n - Si / SnO2 and n - Si / SnO2 / Pt Photoanodes. *J. Electrochem. Soc.* **1986,** *133* (6), 1113-1119.

7. Contractor, A. Q.; Bockris, J. O. M., Investigation of a protective conducting silica film on n-silicon. *Electrochim. Acta* **1984,** *29* (10), 1427-1434.

8. Howe, A. T.; Hawkins, R. T.; Fleisch, T. H., Photoelectrochemical Cells of the Electrolyte-Metal-Insulator-Semiconductor (EMIS) Configuration: I . Metal Thickness and

Coverage Effects in the Pt/Silicon Oxide/n-Si System. *J. Electrochem. Soc.* **1986,** *133* (7), 1369-1375.

9. Menezes, S.; Heller, A.; Miller, B., Metal Filmed-Semiconductor Photoelectrochemical Cells. *J. Electrochem. Soc.* **1980,** *127* (6), 1268-1273.

10. Sze, S. M.; Ng, K., K., *Physics of Semiconductor Devices*. 3rd ed.; John Wiley & Sons, Inc.: Hoboken, NJ, 2007.

11. Chen, Y. W.; Prange, J. D.; Dühnen, S.; Park, Y.; Gunji, M.; Chidsey, C. E. D.; McIntyre, P. C., Atomic layer-deposited tunnel oxide stabilizes silicon photoanodes for water oxidation. *Nat. Mater.* **2011,** *10* (7), 539-544.

12. Fonash, S. J., *Solar Cell Device Physics*. 2nd ed.; Elsevier Inc.: Amsterdam, 2010.

13. Bansal, A.; Lewis, N. S., Stabilization of Si Photoanodes in Aqueous Electrolytes through Surface Alkylation. *J. Phys. Chem. B* **1998,** *102* (21), 4058-4060.

14. Bansal, A.; Lewis, N. S., Electrochemical Properties of (111)-Oriented n-Si Surfaces Derivatized with Covalently- Attached Alkyl Chains. *J. Phys. Chem. B* **1998,** *102* (7), 1067-1070.

15. Bolts, J. M.; Bocarsly, A. B.; Palazzotto, M. C.; Walton, E. G.; Lewis, N. S.; Wrighton, M. S., Chemically derivatized n-type silicon photoelectrodes. Stabilization to surface corrosion in aqueous electrolyte solutions and mediation of oxidation reactions by surface-attached electroactive ferrocene reagents. *J. Am. Chem. Soc.* **1979,** *101* (6), 1378-1385.

16. Chen, S.; Brown, L.; Levendorf, M.; Cai, W.; Ju, S.-Y.; Edgeworth, J.; Li, X.; Magnuson, C. W.; Velamakanni, A.; Piner, R. D.; Kang, J.; Park, J.; Ruoff, R. S., Oxidation Resistance of Graphene-Coated Cu and Cu/Ni Alloy. *ACS Nano* **2011,** *5* (2), 1321-1327.

17. Flynn, G. W., Perspective: The dawning of the age of graphene. *J. Chem. Phys.* **2011,** *135* (5), 050901-8.

18. Lee, Y.; Bae, S.; Jang, H.; Jang, S.; Zhu, S.-E.; Sim, S. H.; Song, Y. I.; Hong, B. H.; Ahn, J.-H., Wafer-Scale Synthesis and Transfer of Graphene Films. *Nano Lett.* **2010,** *10* (2), 490-493.

19. Prasai, D.; Tuberquia, J. C.; Harl, R. R.; Jennings, G. K.; Bolotin, K. I., Graphene: Corrosion-Inhibiting Coating. *ACS Nano* **2012,** *6* (2), 1102-1108.

20. Suk, J. W.; Kitt, A.; Magnuson, C. W.; Hao, Y.; Ahmed, S.; An, J.; Swan, A. K.; Goldberg, B. B.; Ruoff, R. S., Transfer of CVD-Grown Monolayer Graphene onto Arbitrary Substrates. *ACS Nano* **2011,** *5* (9), 6916-6924.

21. Sutter, E.; Albrecht, P.; Camino, F. E.; Sutter, P., Monolayer graphene as ultimate chemical passivation layer for arbitrarily shaped metal surfaces. *Carbon* **2010,** *48* (15), 4414-4420.

22. Nielander, A. C.; Bierman, M. J.; Petrone, N.; Strandwitz, N. C.; Ardo, S.; Yang, F.; Hone, J.; Lewis, N. S., Photoelectrochemical Behavior of n-Type Si(111) Electrodes Coated With a Single Layer of Graphene. *J. Am. Chem. Soc.* **2013,** *135* (46), 17246-17249.

23. Droscher, S.; Roulleau, P.; Molitor, F.; Studerus, P.; Stampfer, C.; Ensslin, K.; Ihn, T., Quantum capacitance and density of states of graphene. *Appl. Phys. Lett.* **2010,** *96* (15), 152104-3.

24. Ponomarenko, L. A.; Yang, R.; Gorbachev, R. V.; Blake, P.; Mayorov, A. S.; Novoselov, K. S.; Katsnelson, M. I.; Geim, A. K., Density of States and Zero Landau Level Probed through Capacitance of Graphene. *Phys. Rev. Lett.* **2010,** *105* (13), 136801.

25. Bae, S.; Kim, H.; Lee, Y.; Xu, X.; Park, J.-S.; Zheng, Y.; Balakrishnan, J.; Lei, T.; Ri Kim, H.; Song, Y. I.; Kim, Y.-J.; Kim, K. S.; Ozyilmaz, B.; Ahn, J.-H.; Hong, B. H.;

Iijima, S., Roll-to-roll production of 30-inch graphene films for transparent electrodes. *Nat. Nano.* **2010,** *5* (8), 574-578.

26. Nair, R. R.; Ren, W.; Jalil, R.; Riaz, I.; Kravets, V. G.; Britnell, L.; Blake, P.; Schedin, F.; Mayorov, A. S.; Yuan, S.; Katsnelson, M. I.; Cheng, H.-M.; Strupinski, W.; Bulusheva, L. G.; Okotrub, A. V.; Grigorieva, I. V.; Grigorenko, A. N.; Novoselov, K. S.; Geim, A. K., Fluorographene: A Two-Dimensional Counterpart of Teflon. *Small* **2010,** *6* (24), 2877-2884.

27. Robinson, J. T.; Burgess, J. S.; Junkermeier, C. E.; Badescu, S. C.; Reinecke, T. L.; Perkins, F. K.; Zalalutdniov, M. K.; Baldwin, J. W.; Culbertson, J. C.; Sheehan, P. E.; Snow, E. S., Properties of fluorinated graphene films. *Nano Lett.* **2010,** *10* (8), 3001-5.

28. Stine, R.; Lee, W.-K.; Whitener, K. E.; Robinson, J. T.; Sheehan, P. E., Chemical Stability of Graphene Fluoride Produced by Exposure to XeF2. *Nano Lett.* **2013,** *13* (9), 4311-4316.

29. Petrone, N.; Dean, C. R.; Meric, I.; van der Zande, A. M.; Huang, P. Y.; Wang, L.; Muller, D.; Shepard, K. L.; Hone, J., Chemical Vapor Deposition-Derived Graphene with Electrical Performance of Exfoliated Graphene. *Nano Lett.* **2012,** *12* (6), 2751-2756.

30. Pirkle, A.; Chan, J.; Venugopal, A.; Hinojos, D.; Magnuson, C. W.; McDonnell, S.; Colombo, L.; Vogel, E. M.; Ruoff, R. S.; Wallace, R. M., The effect of chemical residues on the physical and electrical properties of chemical vapor deposited graphene transferred to SiO2. *Appl. Phys. Lett.* **2011,** *99* (12), -.

31. Plymale, N. T.; Kim, Y.-G.; Soriaga, M. P.; Brunschwig, B. S.; Lewis, N. S., Synthesis, Characterization, and Reactivity of Ethynyl- and Propynyl-Terminated Si(111) Surfaces. *J. Phys. Chem. C* **2015,** *119* (34), 19847-19862.

32. Hao, Y.; Bharathi, M. S.; Wang, L.; Liu, Y.; Chen, H.; Nie, S.; Wang, X.; Chou, H.; Tan, C.; Fallahazad, B.; Ramanarayan, H.; Magnuson, C. W.; Tutuc, E.; Yakobson, B. I.; McCarty, K. F.; Zhang, Y.-W.; Kim, P.; Hone, J.; Colombo, L.; Ruoff, R. S., The Role of

Surface Oxygen in the Growth of Large Single-Crystal Graphene on Copper. *Science* **2013,** *342* (6159), 720-723.

33. Coridan, R. H.; Nielander, A. C.; Francis, S. A.; McDowell, M. T.; Dix, V.; Chatman, S. M.; Lewis, N. S., Methods for comparing the performance of energy-conversion systems for use in solar fuels and solar electricity generation. *Energy Environ. Sci.* **2015,** *8* (10), 2886-2901.

Chapter 3

The effects of 2D materials on semiconductor/liquid junctions

Covalent functionalization of semiconductor surfaces is a well-explored method for shifting band edge positions. However, the process of discovering the chemistry needed for such functionalization can be time-consuming and this strategy is not easily translated between materials without extensive work to develop new reactions. Recently, covering n-type silicon with single layer graphene and its derivative, fluorinated graphene, was reported as a portable strategy for protection against oxidation during photoanodic operation in aqueous solution. In addition, the open-circuit potential of these electrodes was shown to shift in contact with a series of nonaqueous redox couples of varying potentials, indicating a lack of Fermi-level pinning despite the Dirac point of graphene lying mid-gap to silicon (-4.55 eV vs. vacuum).

Further understanding the effect of the density of states of a 2D material on an interface is key to the successful integration of these materials into devices. Many of the extraordinary properties that have made graphene so well studied arise from the existence of a Dirac point in the density of states, which also introduces a finite number of surface states within the band gap of silicon. These states contribute to the formation of a rectifying potential-dependent barrier height in contact with both n-type and p-type silicon unlike the potential-independent barrier heights of semiconductor-electrolyte and semiconductor-metal interfaces. However, these states, and resulting dependence of barrier height on potential, can also attenuate the barrier height of fabricated devices by partially pinning the interface. In contrast, hexagonal boron nitride (h-BN), an analogue of graphene consisting of an alternating lattice of boron and nitrogen atoms, is primarily used as an inert protective layer on 2D material heterostructures. h-BN is known to be a good insulator with a bandgap of 5.97 eV. The lack of states within the bandgap of silicon make it an excellent endpoint for comparison with graphene, as the bandgaps of most 2D materials fall between the range presented by these two materials (0 eV-5.97 eV) and the behavior of each at an interface should be significantly different given their widely varying properties.

Here we probe the effect of 2D materials with significantly different distributions of density of state by comparing the impact of graphene (Gr) and hexagonal boron nitride (h-BN) on the photoelectrochemical performance of p-type silicon. Inserting two-dimensional (2D) materials at the semiconductor/liquid junction should have an impact on junction energetics through the equilibration of the Fermi levels of the semiconductor and the 2D material, depending on the density of states of the interstitial 2D material.

Although single crystals of 2D materials can be obtained through mechanical exfoliation of layered materials, these methods do not produce single crystals of a size large enough to cover even lab scale (~1 cm^2) photoelectrodes. Due to the large area needed, chemical vapor deposition grown (CVD) 2D materials are used because large (>1 cm^2) area samples can easily be produced. However, CVD grown graphene and h-BN are both polycrystalline materials that inherently contain grain boundaries and defects. There is a distinct difference between the electronic structure of the pristine material and the defective sites, which [are known to] locally impact the energetics at the semiconductor/liquid junction. Both the magnitude of such local differences and their influence on macroscale behavior remain as open questions. To address this issue, scanning electrochemical cell microscopy (SECCM) is demonstrated here as a tool to study junction energetics with submicron spatial resolution.

SECCM is a scanning probe microscopy technique that utilizes an electrolyte-filled glass nanopipette as the probe. The counter and reference electrodes of an electrochemical cell are housed within this pipette and connected to a potentiostat. Using a micropositioner, the opening of the pipette is brought close to a surface operating as the working electrode until a nanoscale liquid junction is formed between the pipette and the surface, completing the circuit for the electrochemical cell. The probe is then operated as an electrochemical cell with a working electrode area defined by the size of the liquid junction. SECCM allows standard electrochemical techniques to be performed with a high degree of spatial resolution, and has previously been used in PEC systems to measure resolve photocurrents on heterogeneous surfaces. Beyond enabling spatially resolved electrochemistry, the small surface area of the working electrode in contact with electrolyte makes SECCM ideal for samples that readily degrade or change structure under electrochemical operation, as a location can be tested without affecting the remainder of the sample. Demonstrating the utility of SECCM as a general technique for evaluation of PEC behavior on silicon, a readily available, stable, and well-characterized material, will set the stage for studying materials where the features of SECCM are necessary.

Here we compare the photoelectrochemical behavior of graphene and h-BN covered p-Si photoelectrodes to H-terminated Si (111) surfaces using both macro- and nano-scale photoelectrochemical measurements. We show that h-BN covered electrodes do not exhibit strong evidence of Fermi level pinning while the graphene exhibits evidence of partial Fermi level pinning. Both graphene and h-BN shift the flat band potential of the p-Si to negative potentials relative to the bare surface, resulting in lower open circuit voltages (V_{OC}) for these photoelectrodes in contact with a series of redox couples in solution. Additionally, we show that nanoscale SECCM measurements of V_{OC} correlate well to macroscale observations and replicate observed trends. Finally, we establish the ability of SECCM to elucidate local variability of V_{OC} to demonstrate its future applicability as a technique for imaging semiconductor/liquid junction energetics with nanoscale resolution.

Methods

Materials

Acetonitrile (Dri-Solv, 99.9%) was purchased from Fisher Scientific and used as received. Lithium perchlorate ($LiClO_4$, 99.99%, battery grade) was purchased from Sigma Aldrich and used as received.

Ferrocene (Fc), dimethylferrocene (DiMeFc), nickelocene (Nc), decamethylferrocene (DeMeFc), and cobaltocene (Cc) were all purchased from Sigma-Aldrich and and purified by sublimation prior to use. Cobaltocenium hexafluorophosphate (Sigma-Aldrich, 98%) was recrystallized from ethanol prior to use.

Methyl viologen hexafluorophosphate ($MV(PF_6)_2$) was prepared by metathesis of methyl viologen dichloride (Sigma-Aldrich, 98%) with ammonium hexfluorophosphate (Sigma-Aldrich, 99.98%) in water and recrystallized from ethanol prior to use.

Following purification or purchase, all chemicals were stored in a N_2-filled flush box for storage. Electrolyte solutions were prepared in the flush box using MeCN with 0.5 M $LiClO_4$ as supporting electrolyte. Except for DecaMeFc and MV, which had limited solubility, all of the redox couples were prepared at initial concentrations of ~10 mM. Bulk electrolysis was used to generate the reduced form of MV, as well as all the oxidized forms of the metallocenes except Cc.

Improved buffered HF (BHF, Transene) was used to etch any native oxide on the p-Si wafer pieces immediately before coating with graphene or hexagonal boron nitride. BHF was also used to clean bare p-Si electrodes immediately before electrochemical testing of the bulk properties.

CVD-grown monolayer graphene on Cu (Cu/Gr) was purchased from Advanced Chemical Supplier Materials (Medford, MA). Grains of graphene from this source are known to be around 50 μm in diameter as reported by the manufacturer. Monolayer hexagonal boron nitride grown by chemical vapor deposition on copper (Cu/h-BN) was purchased from Graphene Supermarket. Grains of h-BN from this source are known to be approximately 5 μm in diameter as reported by the manufacturer.

For electrochemical measurements, double-side polished, boron-doped, p-type Si(111) wafers (0.3 Ω cm resistivity, $N_A = 7 \times 10^{16}$ cm^{-3}) were obtained from Addison Engineering, Inc.

Electrode fabrication

Ohmic back contact to the back side for all the p-type silicon wafers used in this study were formed by evaporation of 100nm of gold (Labline Electron Beam Evaporator, Kurt J. Lesker) followed by an anneal at 350°C under forming gas (H_2(g):N_2(g) v:v 5:95). Wafer pieces used in SECCM studies were also lithographically patterned with registry marks to track the location of the electrochemical measurements and ensure that data were collected on intact portions of the 2D material monolayer.

Since the hexagonal boron nitride used in this study was grown on copper as the graphene was, electrodes for both were made analogously. The methods for the graphene electrodes are detailed here. To make the coated electrodes, a strip of copper covered by monolayer graphene (Cu/Gr) was coated with a supporting polymer layer of 495K A4 polymethyl methacrylate (PMMA, MicroChem) at 3000 rpm for 60 s. The resulting stack (Cu/Gr/PMMA) was then cured for 5 minutes at 120°C. Smaller pieces matching the desired size of the fabricated electrodes were cut and etched in a $FeCl_3$ etch solution (Copper etch, Transene) until the copper was gone by visual inspection, approximately 1.5h. This copper-free piece (Gr/PMMA) was transferred to a ≥18MΩ-cm resistivity water bath for 1h before transfer to a second clean water bath were it was left for 12h. After transfer to a final fresh water bath, the stack was pulled onto a p-Si wafer piece that had been etched with improved buffered HF (Transene), dried thoroughly using a gentle stream of nitrogen, and heated to 80°C for 10 minutes to allow the PMMA layer to reflow. The substrate was then rinsed in acetone for 10 minutes before being annealed for 2h at 350°C in a reducing atmosphere (H_2(g):Ar(g) v:v 5:95) to remove any residual PMMA from the transfer process.

The p-Si/Gr stack was attached to a Cu wire using Ga-In eutectic alloy and high purity silver paint (SPI Supplies, West Chester, Pennsylvania). The back of the electrode was covered with a layer of clear nail polish to prevent any leakage of the Ga-In eutectic. Then the sample was sealed to a Pyrex tube with a layer of Loctite 9460 Hysol epoxy and allowed to cure overnight. The area of the resulting electrode was measured using ImageJ to analyze optical images of each electrode.

For the macroscale measurements, a set of control electrodes (p-SiOx) were made analogously to the p-Si/Gr and p-Si/h-BN electrodes described above. In brief, a layer of PMMA was spun onto bare copper foil to generate a PMMA/Cu stack. This stack was processed identically to the PMMA/Gr/Cu stacks to yield p-Si-H with no 2D overlayer. The samples will be referred to as p-SiO_x or blank electrodes as the processing and annealing steps generated a small amount of silicon oxide on the surface, in contrast with the p-Si-H electrodes, which were etched with improved buffered HF immediately prior to testing to completely remove any oxide.

SECCM samples were made analogously to the bulk process above with the Gr and h-BN samples transferred to the same p-Si wafer chip to ensure uniformity between the two materials. After annealing, the sample was attached through the back contact to a custom SECCM stage for analysis.

Hall samples were prepared by transferring graphene using the methods detailed above to p-Si with a 300 nm thermal oxide. Gold top contacts were deposited by e-beam evaporation with a thin titanium adhesion layer.

Electrochemical Methods

Bulk electrolysis was performed in a four-neck round bottom flask inside a N_2 flush box with <3 ppm O_2. The working and counter electrodes were Pt meshes, while the reference electrode was a Pt-polypyrrole reference electrode prepared in a 0.5 M $LiClO_4$-MeCN solution. The reference and counter electrodes were each contained in separate compartments constructed from borosilicate tubing with a Vycor porous glass frit attached to the end with Teflon heat-shrink tubing. Each compartment was filled with 0.5 M $LiClO_4$-MeCN solution. Progress of the bulk electrolysis was monitored by cyclic voltammetry using a 12.5 µm radius Au ultramicroelectrode.

All macroscale measurements were performed inside an Ar drybox with <0.5 ppm O_2 using a SP-200 Biologic potentiostat. The reference electrode was a platinum wire coated with a layer of polypyrrole (Pt-PPy), deposited from a 10 mM solution of pyrrole in 0.5 M $LiClO_4$-MeCN following established procedures.[1] The reference was remade for testing with each redox couple and consistently produced a stable potential around +0.2 V vs. Ag/AgCl. Cyclic voltammograms on p-Si–H, pSiOx, p-Si/Gr, and p-Si/h-BN using each redox couple were recorded at 50 mV/s scan rate under illumination and in the dark. Open circuit potential was measured multiple times for each electrode, although the duration of the measurements were adjusted for different redox couples and locations to allow enough time for V_{OC} to stabilize.

Pipettes for SECCM were prepared using a Sutter Instruments P-2000 laser puller. Quartz theta capillaries (1.2 mm O.D., 0.9 mm I.D, Sutter Instruments) were first cleaned with acetone and methanol, then pulled to create pipettes with openings from 50-500 nm radius. The pipettes were then silanized with chlorotrimethylsilane to create a hydrophobic surface. Pipettes were filled with electrolyte solutions using a glass syringe and a stainless steel needle.

All SECCM measurements were performed using a CHI 920D inside a N_2 flush box with < 3 ppm O_2. The counter and reference electrodes were 0.2 mm Pt wires, each on opposite sides of the theta pipette, and the p-Si photoelectrode was the working electrode. Prior to approaching the surface, pipettes were positioned within 20 microns of the surface using an endoscope. The substrate was then biased positive with respect to the reference electrode as pipettes were brought towards the surface. Movement automatically stopped when the potentiostat detected the current spike that occurred when a liquid junction formed. Illumination for photoelectrochemical SECCM experiments was provided at a 45° angle by fiber optic attached to an ELH lamp inside the flush box that gave a measured illumination intensity equivalent to 1 sun. As in the macroscale measurements, cyclic voltammograms at each location using each redox couple were recorded at 50 mV/s scan rate under illumination and in the dark. Open circuit potential measurement times were adjusted for different redox couples and locations to allow enough time for V_{OC} to stabilize.

Instruments

X-ray photoelectron spectroscopic (XPS) data were collected at 1E-9 Torr using a Kratos AXIS Ultra DLD with a magnetic immersion lens that consisted of a spherical mirror and concentric hemispherical analyzers with a delay-line detector (DLD). An Al Kα (1.486 KeV) monochromatic source was used for X-ray excitation. Ejected electrons were collected at a 90° angle from the horizontal. The CASA XPS software package v 2.3.16 was used to analyze the collected data.

Carrier mobilities were obtained using an H-50 MMR Hall Measurement System. Raman spectra were collected with a Renishaw Raman microscope at λ=532 nm through an objective with numerical aperture=0.75. The laser power was ~3 mW. UV/Vis transmission spectra were collected with a Cary 5000 absorption spectrometer equipped with an external DRA 1800 attachment. The data were automatically zero/baseline corrected by the instrument before any additional processing was performed.

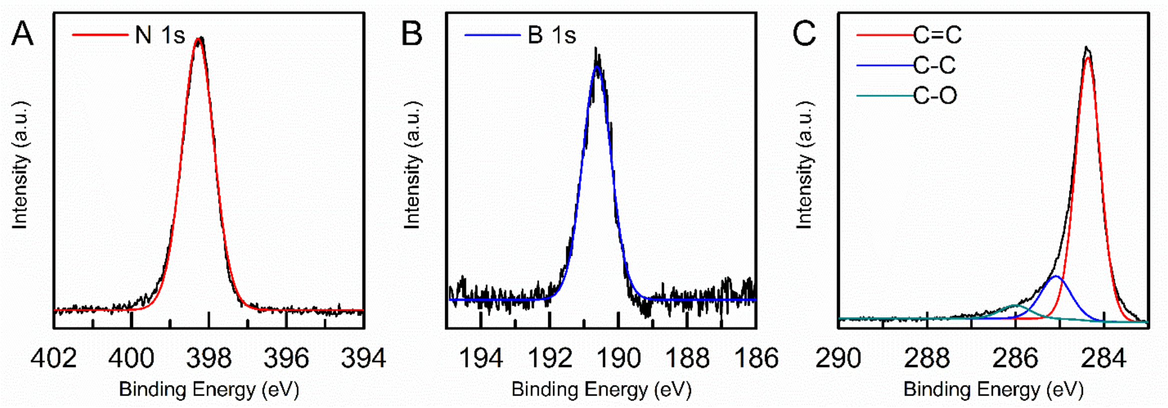

Figure 1. X-ray photoelectron spectra of A) the N 1s and B) the B 1s region of a typical p-Si/h-BN sample and C) the C 1s region of a typical p-Si/Gr sample.

Results

Characterization

The graphene and hexagonal boron nitride used in this study were fully characterized using x-ray photoelectron spectroscopy, Raman spectroscopy, and UV/vis spectroscopy. In addition, measurements of the Hall mobility of graphene were collected for four different devices, yielding an average value of 968 cm^2/V*s as expected for monolayer polycrystalline graphene.

Figure 1 shows the X-ray photoelectron spectra for typical p-Si/Gr and p-Si/h-BN samples after anneal under forming gas. Figure Xa-b displays the N 1s and B 1s regions of an h-BN sample with single peaks at 398.3 eV and 190.6 eV respectively, yielding a 1:1 ratio of B:N from the area after adjusting for elemental relative sensitivity factors. The C 1s region of a p-Si/Gr sample in Figure Xc has three peaks at 284.4 eV, 285.0 eV, and 286.1 eV, assigned to the sp^2 carbon bonds of graphene and the residual C-C and C-O bonds of the PMMA transfer support respectively.

Figure 2 shows the x-ray photoelectron spectra of the Si 2p region for a typical p-Si/Gr and p-Si/h-BN samples from this work. The peaks at 99.2 and 99.8 eV are assigned to the Si 2p$_{1/2}$ and 2p$_{3/2}$ peaks respectively. The peak at 102.5 eV is attributed

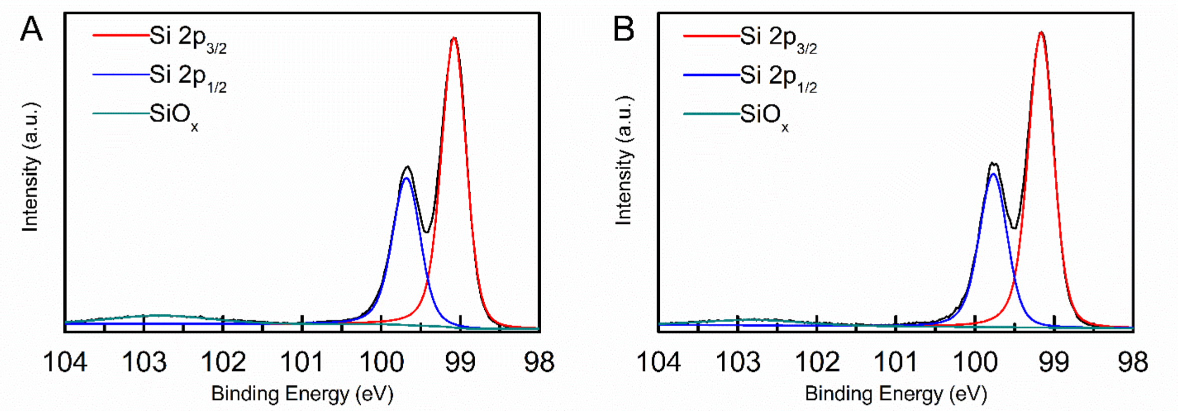

Figure 2. X-ray photoelectron spectra of p-Si surfaces. (A) The Si 2p region of a p-Si/Gr electrode after fabrication. (B) The Si 2p region of a p-Si/h-BN electrode after fabrication. The peaks at 99.2 and 99.8 eV are assigned to the Si 2p$_{1/2}$ and 2p$_{3/2}$ peaks respectively, while small peak at 102.5 eV is attributed the oxide formed during the fabrication process.

to the formation of oxide on the surface. Indeed, a small amount of oxide is expected from the fabrication process, due to the brief exposure of the surface to water during the transfer process. The thickness of this oxide was quantified using a simple substrate-overlayer model

$$d = \lambda_{ov} \sin\theta \left[\ln\left(1 + \frac{I_{Si}^{o}}{I_{ov}^{o}} * \frac{I_{ov}}{I_{Si}}\right) \right]$$

where λ_{ov} is the attenuation factor through the oxide overlayer (2.6 nm), θ is the angle from the surface to the detector, I_{Si}^{o}/I_{ov}^{o} is the instrument normalization factor expected from uncontaminated Si and SiO_2 samples, which was taken as 1.3 for this instrument, I_{ov} is the measured intensity of the silicon oxide peak found around 103 eV, and I_{Si} is the measured intensity of the silicon. [2,3] Using this equation, an oxide of approximately 0.22 nm was detected on the p-Si/Gr electrodes and an oxide of approximately 0.23 nm was detected on the p-Si/h-BN electrodes. As a monolayer of oxide is about 0.35 nm thick,[3] the average electrode tested in this work had less than a monolayer of oxide growth after the fabrication process.

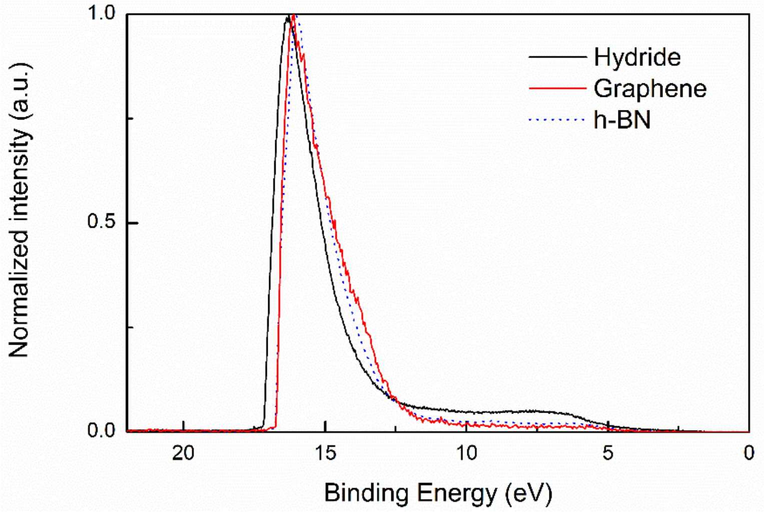

Figure 3. Ultraviolet photoelectron spectra of annealed p-Si-H, p-Si/Gr and p-Si/h-BN samples, corrected with reference to a sputter-cleaned Au sample.

The effect of the fabrication process on each sample was also followed by ultraviolet photoelectron spectroscopy (UPS) to understand the band positions of each type of sample. Figure 3 shows the normalized UP spectra of annealed p-Si-Gr and p-Si/h-BN samples. The secondary electron cutoff (SEC) of both shifted equally from the SEC of the annealed p-Si-H sample. The work function (W_F) of each sample was calculated by extrapolating the slope of the SEC to its intercept with the x-axis and subtracting that value from the excitation energy of He I (21.21 eV). The data before and after annealing are shown in Table 1. The magnitude of the work function for p-Si-H is attenuated from the value calculated from the dopant density (N_A=7x10^{16} cm^{-3}, W_F=5.02 eV, $E_{VBM}{}^B$=0.14 eV) but is consistent with the band-bending and dipole expected on this surface.[4] The increase in the work function of p-Si/h-BN is attributed to the formation of oxide during annealing by water trapped at the p-Si/h-BN interface during transfer, attenuating the surface dipole.

Table 1. Secondary electron cutoff, dipole, and work function of samples

	Before anneal				After anneal			
Sample	SEC eV	E_{VBM}^{S} eV	δ eV	W_{F}^{S} eV	SEC eV	E_{VBM}^{S} eV	δ eV	W_{F}^{S} eV
p-Si–H	16.82	0.59	-0.19	4.39	16.93	0.53	-0.36	4.28
p-SiO_x	16.43	0.29	-0.09	4.78	16.50	0.30	-0.16	4.71
p-Si/Gr	16.51	0.41	-0.06	4.70	16.48	0.56	+0.12	4.73
p-Si/ h-BN	16.58	0.53	-0.08	4.63	16.57	0.49	-0.04	4.64

Figure 4 displays the typical Raman spectrum for Gr and h-BN respectively along with contour plots of the surfaces. The Raman spectrum of Gr displays three peaks at 1595 cm^{-1}, 2464 cm^{-1}, and 2691 cm^{-1}, arising from the E_{2g} and A_{1g} modes of the lattice.[5] The primary peaks at 1595 cm^{-1} and 2691 cm^{-1} are known as the G and 2D peaks respectively. The ratio of these peaks (I_G/I_{2D}) is used to understand the integrity of graphene with intact graphene having a ratio of 0.4 to 0.6. In contrast, the Raman spectrum of h-BN has a single peak at 1367 cm^{-1} and so contour plots can only show the relative intensity of different spots on a sheet of h-BN.[6] Each contour plot exceeds the size expected for a single grain of Gr or h-BN, given an average diameter of 50 µm and 5 µm respectively. The scale for each plot is set so that regions with no intensity should be bright blue to differentiate between regions of variable and no intensity. For the graphene contour plot, 95% of values for the ratio of the G to 2D peak are found above 0.4 as expected for monolayer Gr. The dark spots on the plot correspond to a decreased ratio of these two peaks but not to a concomitant increase in the D peak at 1350 cm^{-1}, which would indicate defects in the sheet.[7] As only a single peak is present in a Raman spectrum of h-BN, the contour plot of h-BN displays peak intensity at each point. While intensity varies across the h-BN sheet, there are no voids visible at this scale.

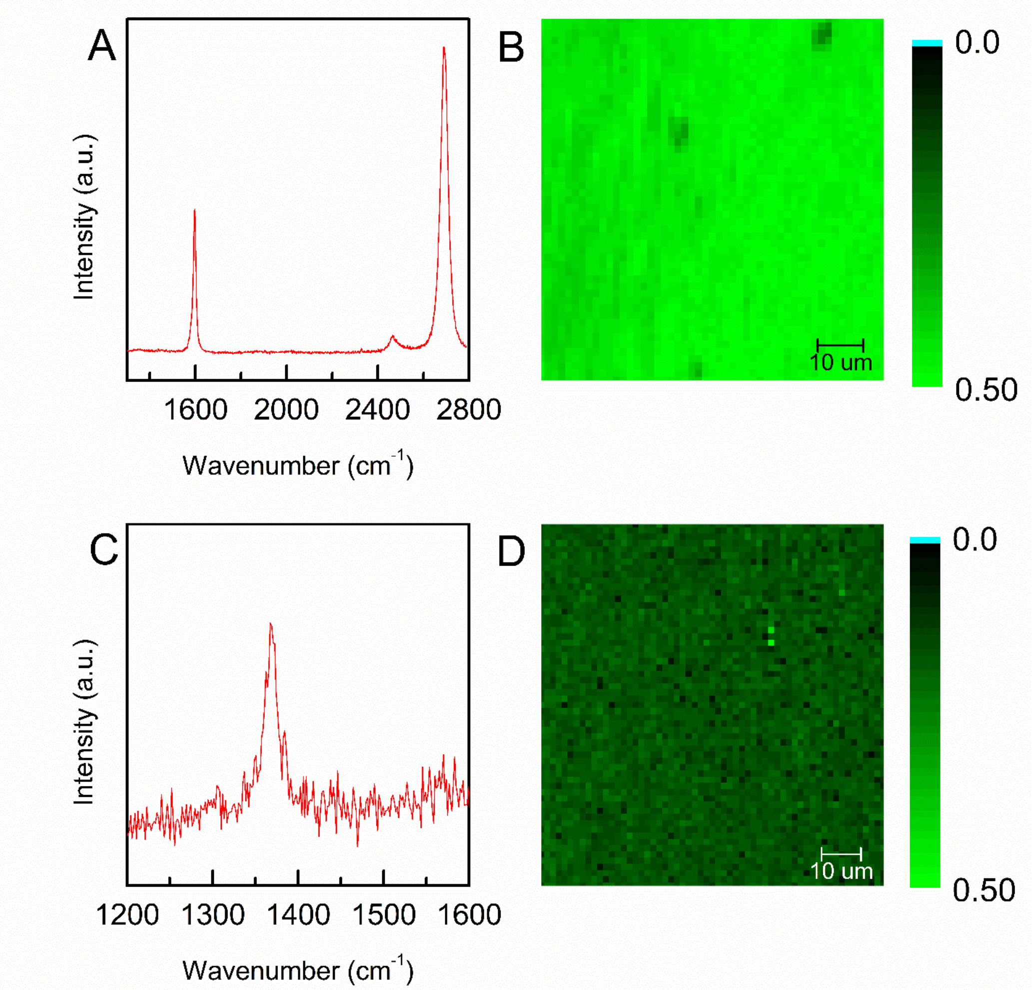

Figure 4. Raman spectra of Gr and h-BN on 300 nm SiO_2. (A) A typical Raman spectrum for a Gr sample with two main peaks at 1595 cm^{-1} (G) and 2691 cm^{-1} (2D). (B) Contour plot of the ratio of the 2D to G peak intensities for a typical monolayer Gr sample from a Raman map. (C) A typical Raman spectrum for an h-BN sample with a single peak at 1367 cm^{-1}. (D) Contour plot of the peak intensity for a typical monolayer h-BN sample from a Raman map. While intensity varies across the sample, the data indicates that the 1370 cm^{-1} peak is present in each spectra. Both contour plots display data for a 75x75 μm region on the sample, which should exceed the size of single grain on either 2D material. For each plot, bright blue is used for an intensity of zero to highlight any voids in the lattice, although none are visible.

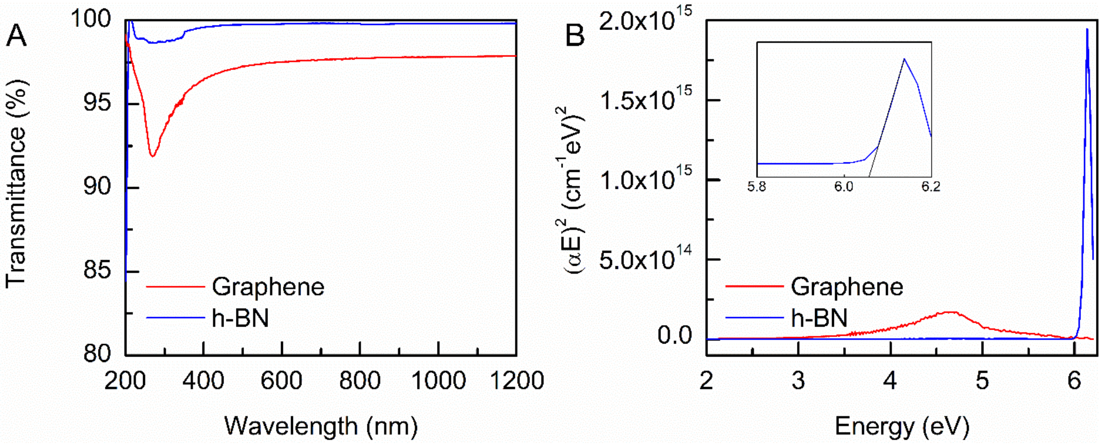

Figure 5. UV/Vis spectra for (A) Gr and h-BN samples on quartz slides and (B) the Tauc plot for h-BN and Gr. The fit for h-BN is shown in the inset.

Figure 5 displays the UV/vis spectra for Gr and h-BN on quartz. h-BN shows almost absorption across the visible light region (400-700 nm), while Gr absorbs 2.7% of light in the same region. The optical bandgap of h-BN was determined to be 6.07 eV from extrapolation of the linear region of the Tauc plot to an intercept with the x-axis, which is within the typical bounds for the polycrystalline material.[8] The same plot for the graphene shows no such sharp increase indicative of the presence of a bandgap.

Electrochemistry

Figure 6 compares the representative macroscale (A-B)and SECCM (C-D) behavior of current with respect to potential for p-Si, p-Si/Gr, and p-Si/h-BN electrodes in the dark and under 100 mW cm^{-2} ELH-s illumination in 0.5 M $LiClO_4$-MeCN solutions containing either Fc or Cc. Additional samples referred to as p-SiO_x, or “blank” electrodes, in reference to the small amount of oxide grown on the surface during fabrication (see Methods for more detail), are also included in the macroscale measurements to show the behavior of the Si wafer when it was subjected to the same processing steps as the p-Si/Gr and p-Si/h-BN electrodes without actually transferring a 2D overlayer to the surface. For macroscale electrodes (Figure 6A, C), the bare p-Si-H and p-SiO_x electrodes exhibited rectifying behavior toward both redox couples, as indicated by cathodic photocurrent under reverse bias. In Fc, p-Si/h-BN electrodes exhibit minimal rectification under illumination, but still have a significant current under reserve bias in the dark. In Cc, these electrodes show strong rectification with only minimal dark current and a large photocurrent. In contrast, the p-Si/Gr samples exhibit ohmic behavior in the Fc solution and moderately rectifying behavior in the Cc solution, as shown by the rapid increase in currents under forward bias for both of these sample types in the dark. Similar behavior for all samples was observed by SECCM (Figure 6B, D). While the macroscale measurements are shown as current density versus potential, the same metric is not used for the SECCM measurements due to effect of pipette tip size on resulting current density. Thus, the SECCM data is graphed as a ratio of the current to the steady-state current (i/i_{ss}), a ratio commonly used in the SECCM literature.

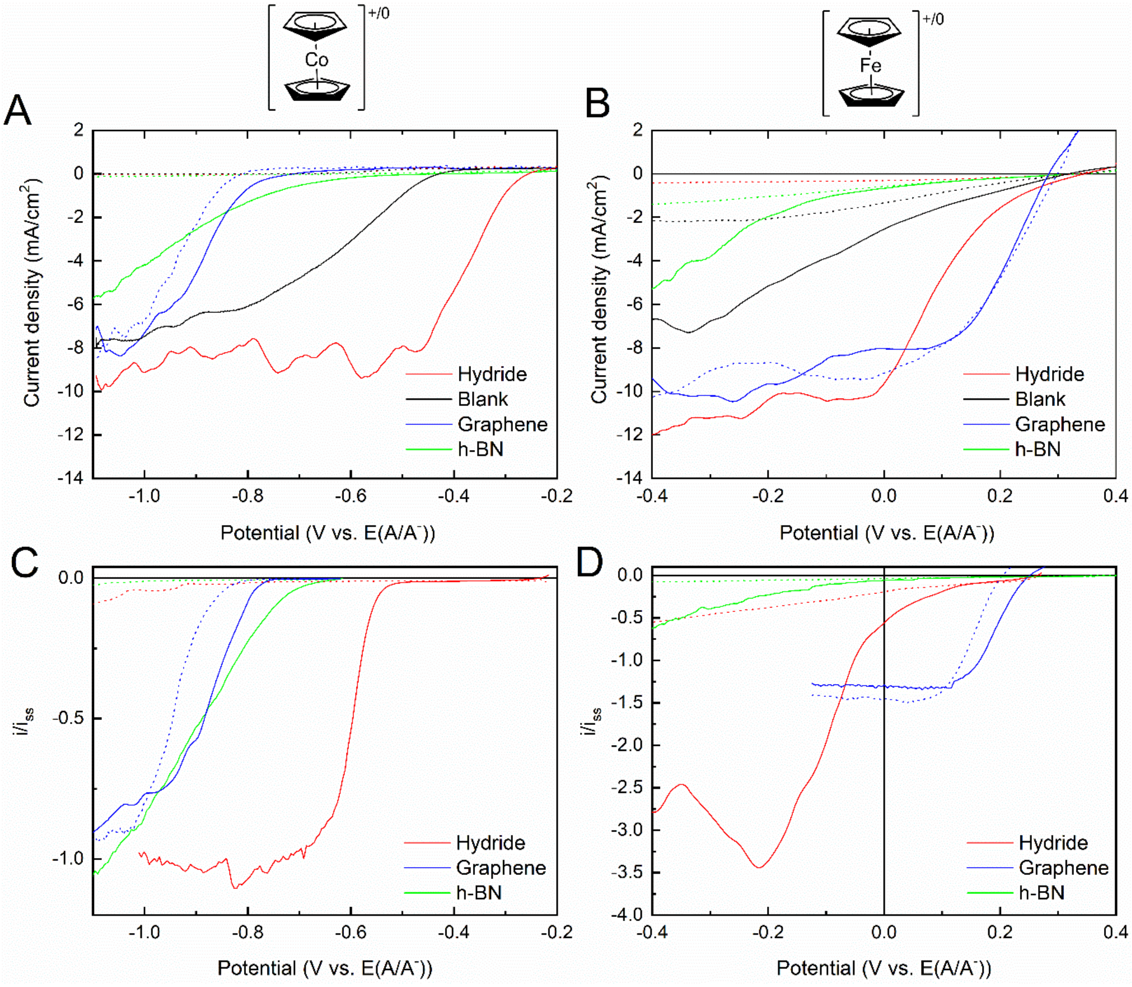

Figure 6. Photocurrent density-potential (J-V) performance of p-Si electrodes in contact with cobaltocene (A, C) and ferrocene (B, D) in CH_3CN–0.5 M $LiClO_4$ under 100 mW cm^{-2} ELH illumination. The dashed lines show scans of the same electrodes without illumination. In both sets of data, the fill factor of p-Si/h-BN electrode is significantly worse than either the p-Si-H or p-SiO_x, while the p-Si/Gr electrode display little to no shift upon illumination as expected in Cc and Fc for a weakly rectifying or ohmic contact respectively with solution.

Figure 7 shows the dependence of V_{OC} on the effective solution potential for p-Si–H, p-Si/Gr, and p-Si/h-BN in contact with 1.0 M $LiClO_4-CH_3CN$ under 100 mW cm^{-2} ELH-type illumination. Each point represents an average of at least 5 electrodes with standard deviations represented by the error bars. Since the effective potential of Fc and DiMeFc were very close, only data for Fc is shown in Figure 7 for clarity. The V_{OC} data for DiMeFc can be found in Table 2. In both the macroscale and SECCM measurements, the p-Si–H, $pSiO_x$, and p-Si/h-BN samples show two distinct trends: regions at relatively positive or negative $E_{eff}(A/A^-)$ where V_{OC} is fixed with respect to $E_{-eff}(A/A^-)$ and a second region where V_{OC} scales approximately linearly with V_{OC}. The slopes of V_{OC} with respect to effective potential is lower than reported previously, but the maximum ΔV_{OC} of 470±57 mV for p-Si–H is comparable with the previously reported value of 523±42 mV.[9] The p-Si–H samples in this work display a slope around 0.50 while the $p\text{-}SiO_x$ and p-Si/h-BN samples both have a slope around 0.35. The p-Si/Gr samples display the least change in V_{OC} across the full range of redox couples, shifting only in couples with sufficiently negative $E_{eff}(A/A^-)$ with a slope around 0.10. This is true for both the macroscale and SECCM measurements. The maximum ΔV_{OC} for p-Si–H by SECCM is 342±18 mV, which is closer to 401±33 mV, the maximum ΔV_{OC} value for the macroscale $p\text{-}SiO_x$ measurements. As the p-Si—H, p-Si/Gr, and p-Si/h-BN measurements were all taken on the same wafer chip to ensure uniformity in sample preparation, it was not possible to etch the p-Si–H surface immediately before testing, leaving a small amount of oxide on the surface, similar to the preparation of the $p\text{-}SiO_x$ electrodes described previously. Experimental conditions and all V_{OC} data for the macroscale and SECCM measurements are summarized in Table 2.

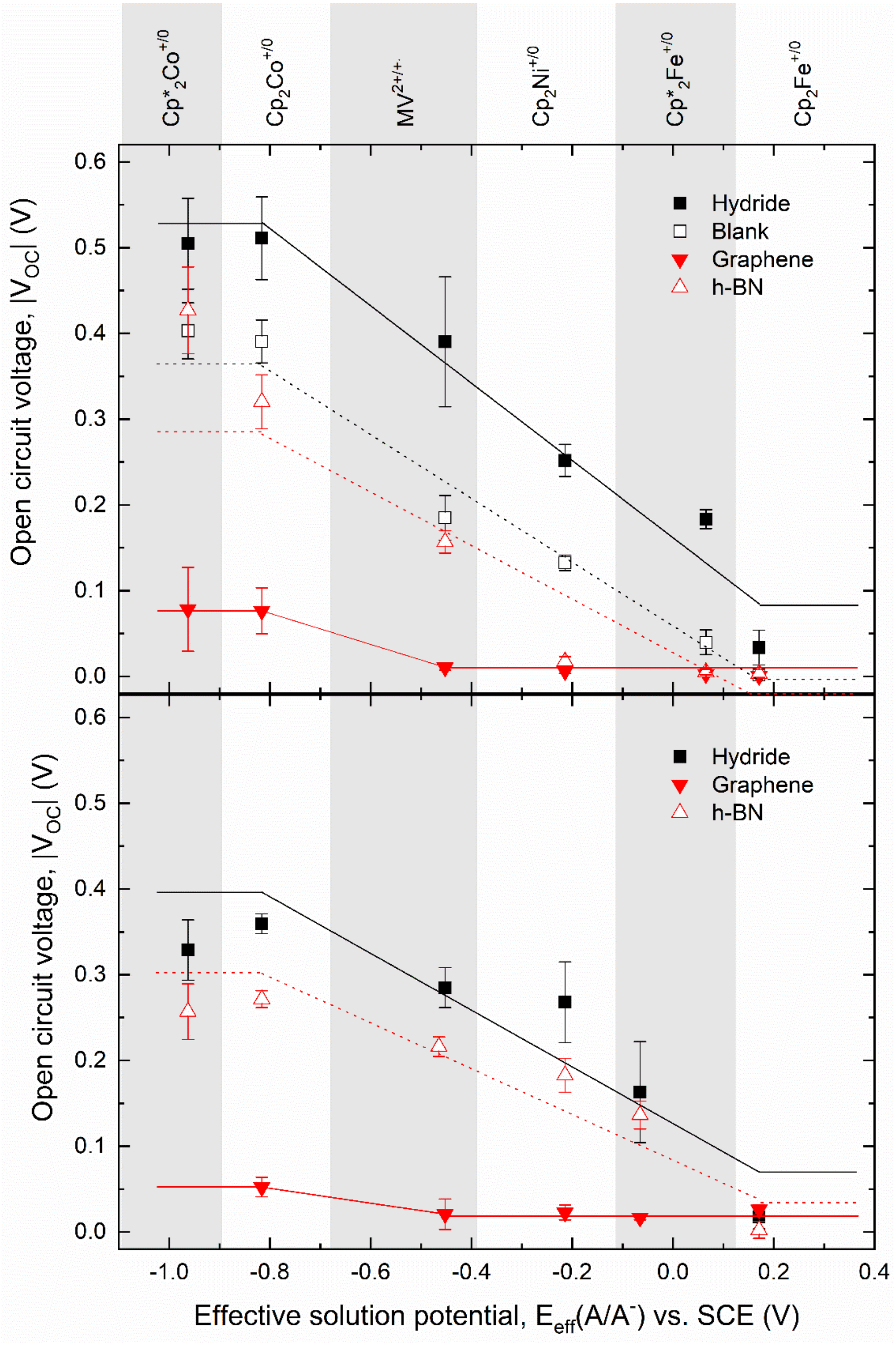

Figure 7. Comparison of open-circuit potential of p-Si–H, p-SiO$_x$, p-Si/Gr, and p-Si/h-BN electrodes versus the effective potential of various redox couples for macroscale electrodes (upper) and by SECCM (lower). Three regions have been identified for all samples. These regions are highlighted with lines meant to guide the eye.

Table 2. Summary of experimental conditions and results [a]

	concentration (mM)		effective potential vs. SCE (V)	V_{OC} (V) from macroscale electrodes				V_{OC} (V) from SECCM electrode		
	ox	red		p-Si–H	p-SiO$_x$	p-Si/ Gr	p-Si/ h-BN	p-Si–H	p-Si/ Gr	p-Si/ h-BN
decamethyl-cobaltocene$^{+/0}$ Cp*$_2$Co$^{+/0}$	5.7	0.4	-0.963	0.505(53)	0.403(33)	0.078(49)	0.427(50)	0.329(35)	-[b]	0.257(32)
cobaltocene$^{+/0}$ Cp$_2$Co$^{+/0}$	16.6	0.4	-0.816	0.511(48)	0.391(25)	0.077(27)	0.320(31)	0.360(11)	0.052(11)	0.272(10)
methyl viologen$^{2+/+\bullet}$ MV$^{2+/+\bullet}$	2.0	0.1	-0.453	0.390(76)	0.185(26)	0.011(3)	0.157(13)	0.285(23)	0.021(18)	0.216(11)
nickelocene$^{+/0}$ Cp$_2$Ni$^{+/0}$	0.5	2	-0.214	0.252(19)	0.133(9)	0.006(3)	0.018(6)	0.268(47)	0.023(9)	0.183(20)
decamethyl-ferrocene$^{+/0}$ Cp*$_2$Fe$^{+/0}$	1.3	0.2	0.065	0.183(11)	0.040(14)	0.003(1)	0.005(3)	0.163(60)	0.017(3)	0.136(16)
dimethyl-ferrocene$^{+/0}$ Me$_2$Cp$_2$Fe$^{+/0}$	10.6	2.4	0.167	0.087(48)	0.005(3)	0	0	0.066(12)	0.018(5)	0.019(9)
ferrocene$^{+/0}$ Cp$_2$Fe$^{+/0}$, or Fc$^{+/0}$	12.9	0.7	0.171	0.034(20)	0.002(1)	0	0.003(5)	0.018(14)	0.026(5)	0.002(10)

[a] Each value of V_{OC} represents measurements from at least six photoelectrodes on the macroscale and at least three spots by SECCM. Standard deviations are given in parentheses, where appropriate.

[b] Due to the lack of stability in the decamethylcobaltocene couple, no SECCM measurements could be collected for the p-Si/Gr interface

Figure 8 shows line scans of V_{OC} by SECCM for p-Si/Gr and p-Si/h-BN in contact with Cc, Nc, and DiMeFc. These measurements were taken in consecutive 10 μm steps, although each scan with a different redox couple was collected on a separate region of the sample in order to avoid cross contamination of the redox species. For p-Si/Gr, the measurements for Nc and DiMeFc are very similar and show little spatial variation across the measured region. The V_{OC} values for pSi/Gr in contact with Cc are distinctly higher but also show relatively little spatial variation. The V_{OC} of p-Si/h-BN sample in contact with the same redox couples shifts over a much wider range of potentials. For both samples, the V_{OC} does not vary significantly across the surface, despite the presence of grain boundaries in the polycrystalline material. The measurements of V_{OC} in contact with Nc shows the largest variation across the surface on both the p-Si/Gr and p-Si/h-BN.

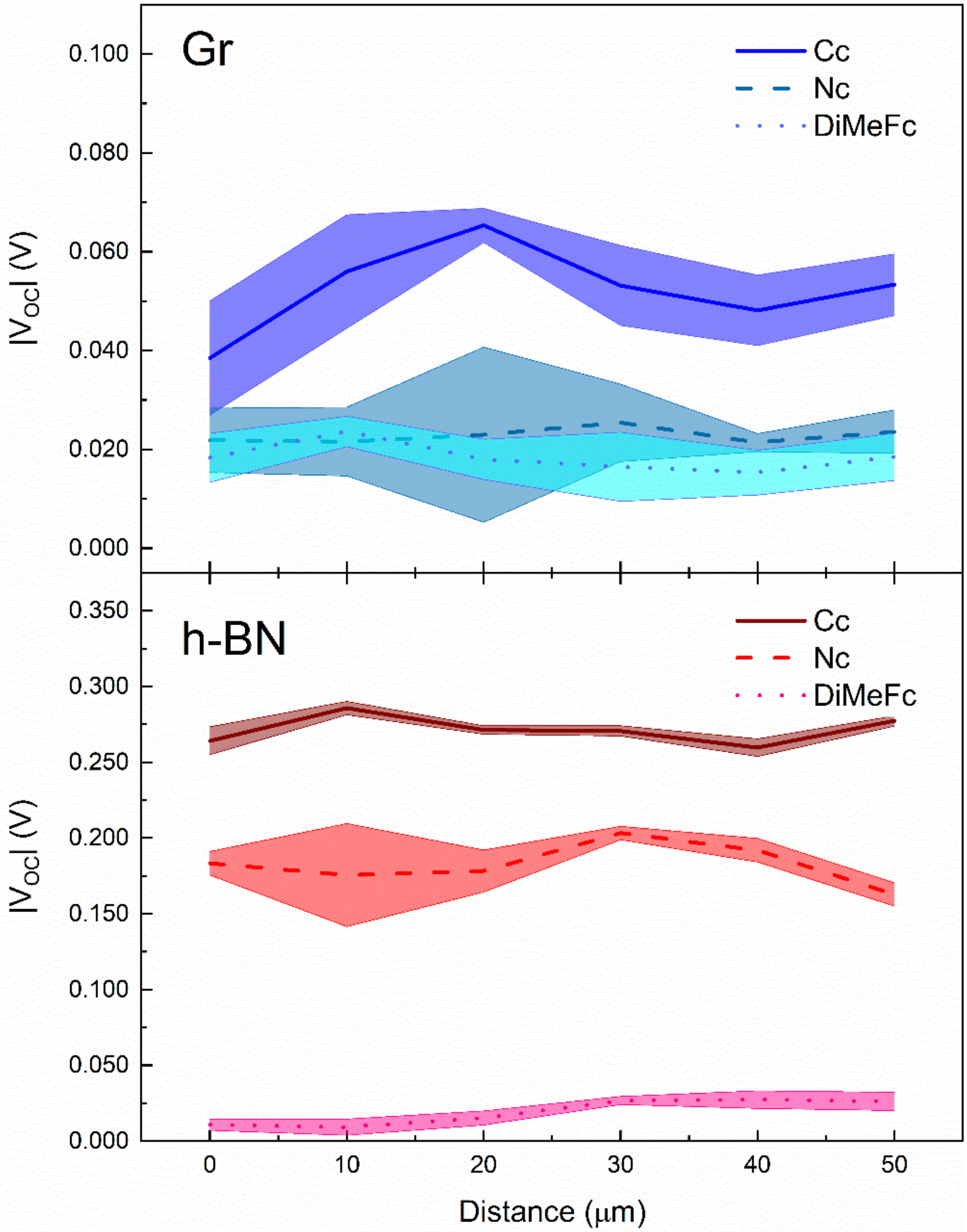

Figure 8. SECCM line scan of V_{OC} in 10 µm steps on Gr (upper) and h-BN (lower) in contact with Cc, Nc, and DiMeFc. Each value is the average of six measurements at the same spot. Standard deviations are represented by the shaded regions surrounding each scan.

Discussion

During macroscale testing, six replicate photoelectrodes were tested for each redox couple. Each photoelectrode was used to measure V_{OC} against a single redox couple to avoid testing samples that may have degraded through use. Specifically, this procedure guards against using samples where graphene has delaminated from the Si surface due to capillary forces produced as the electrolyte solvent dries while cleaning and moving a single sample between different solutions. Because of this precaution, the V_{OC} has not been tested against the full range of redox couples for any single electrode. Due to the small spot size of SECCM, the full complement of redox couples could be measured on a single 1 cm^2 sample containing bare regions and regions covered separately by Gr and h-BN, thereby allowing their distinct behaviors to be elucidated.

As shown in Figure 6, measurements of V_{OC} by SECCM generally show excellent agreement with their macroscale counterparts with few exceptions. The values for V_{OC} of p-Si–H at the macroscale are consistently higher than those observed by SECCM. The values of V_{OC} for p-Si–H by SECCM are much closer to the values of V_{OC} for the macroscale p-SiO_x electrodes. This similarity follows from the data in Figure 4, which shows that the same thickness of oxide was generated at the surface of the p-SiO_x electrodes as the p-Si/Gr and p-Si/h-BN electrodes during fabrication. Thus, the bare region of the single electrode used for SECCM is more similar to the silicon surface under Gr or h-BN than to a freshly etched p-Si–H electrode. The oxide then accounts for a decrease in observed V_{OC} of approximately 100 mV.

Additionally, select measurements, such as the V_{OC} of p-Si/h-BN in contact with $Nc^{0/+}$, were lower in the macroscale measurements than in the SECCM. However, these differences are predominantly observed for the less stable redox couples (i.e. DecaMeCc, Nc). The slope in V_{OC} for p-Si–H, p-SiO_x and p-Si/h-BN are identical within error for the macroscale and SECCM measurements, demonstrating the observed trends remain the same across the macro and nanoscale, despite minor discrepancies. Hence, measurements against redox couples spanning a large range of potentials are necessary to fully understand the trend in V_{OC} on a photoelectrode using these techniques.

A comparison of the cyclic voltammetry (Figure 7) shows identical shapes between macroscale and SECCM measurements for these samples, but reveals different behavior between the types of sample. The p-Si–H is strongly rectifying in contact with cobaltocene and has a high value of V_{OC} upon illumination. While the p-Si/h-BN is also rectifying, the shape of the curve under illumination shows much more resistive behavior than that of the p-Si–H. In fact, the light limiting current was not reached until the potential was pushed further negative of the window shown. The p-Si/Gr interface was shown to be weakly rectifying to cobaltocene and shows very little difference in behavior in the dark or under illumination, indicating that it forms a poor interface for charge separation as fabricated. In contact with Fc, all samples are ohmic and display similar shapes to the voltammetry against Cc.

The differences in the values for V_{OC} in the p-Si/Gr and p-Si/h-BN samples could be attributed to the presence of oxide at the surface, increased surface recombination due to the surface oxide or defects in the 2D material overlayer, and the relative density of states of each overlayer. The effect of the oxide on V_{OC} has already been discussed and ΔV_{OC} was calculated to be about 100 mV as compared to the V_{OC} from the pristine p-Si-H surface. However, this does not account for the additional 200-300 mV difference observed between the p-SiO_x and p-Si/2D overlayer electrodes. The similarity in slopes for the p-SiO_x and p-Si/h-BN electrodes suggests that alterations to the expected V_{OC}, the value for p-Si–H at the same potential, can be treated as linear decreases in the overall performance of the p-Si/h-BN electrodes. The difference between the p-Si/h-BN and p-SiO_x samples was consistently 65 mV for both the macroscale and SECCM measurements. In contrast, the p-Si/Gr electrodes have very different behavior over the same range of effective potentials, suggesting that a different mechanism is at work to explain the drastic decrease in V_{OC} observed for these samples.

The samples fabricated in this work used polycrystalline, CVD-grown sheets of monolayer 2D material, which is known to contribute to defects on the surface of a 2D material and provide sites for increased surface recombination.[10,11] A comparison of the surface recombination velocity (SRV) of these samples shows that p-SiO_x samples have a slightly lower SRV (3025 cm s^{-1}) than the p-Si/Gr (4064 cm s^{-1}) and p-Si/h-BN samples (3905 cm s^{-1}) by a factor of 0.33. The difference between the SRV for p-SiO_x and p-Si/2D overlayer could be attributed to the additional recombination sites provided by the defects in the polycrystalline 2D material overlayer; however, while the polycrystallinity of the Gr and h-BN used in this work would contribute to the smaller range of tunable V_{OC} when compared to p-Si–H or p-SiO_x, it would not account for the differences between the p-Si/Gr and p-Si/h-BN samples. In particular, the grains of the h-BN used in this work, and thus the number of atoms involved in bonding at a grain boundary, were smaller than those in the Gr by an order of magnitude. If the crystallinity were the sole factor in limiting the range of potentials at the interface, p-Si/h-BN would be predicted to have lower values of V_{OC} than p-Si/Gr. Since the reverse behavior is observed, the difference in the samples cannot be attributed to the different grain sizes.

As the surface oxide, increase in recombination, and polycrystalline nature of the 2D overlayer only partially account for the difference between p-Si–H and p-Si/Gr or p-Si/h-BN, the properties of the 2D material and interaction with the surface must also contribute significantly to the observed differences. The crystal structure and lattice constants for Gr and h-BN are nearly identical and differ most prominently in the size of bandgap. With a limited density of states near its Fermi level, which is positioned mid-gap to silicon, graphene is more likely to be pinned at the interface than h-BN, which has no states mid-gap or near the conduction or valence band of silicon. This difference between Gr and h-BN is reflected in the values for δ calculated from the XPS data. Both p-Si–H and p-Si/h-BN electrodes after anneal have negative surface dipoles, which contribute beneficially to V_{OC}, although p-Si/h-BN has a significantly smaller surface dipole than p-Si–H. In contrast, the p-Si/Gr electrodes have a positive surface dipole, which lowers the resulting V_{OC}. The original dipole of the p-Si/Gr surface suggests that before the annealing step the p-Si/Gr should have a V_{OC} closer to the values seen on the annealed p-Si/h-BN surface. Similarly, the unannealed p-Si/h-BN samples should have values of V_{OC} close to a freshly etched p-Si–H. Thus, the changes to the surface because of annealing, including removal of polymer residue and growth of the interfacial oxide, affect both p-Si/h-BN and p-Si/Gr interfaces, but are more detrimental to the p-Si/Gr interface due to the reversal of the surface dipole.

Conclusion

This work demonstrates that the macroscale behavior of photoelectrodes can be reliably reproduced on the nanoscale by SECCM. Additionally, the V_{OC} values for p-Si/h-BN and p-Si/Gr demonstrate that the performance of these interfaces is dependent primarily on the position of the Fermi level and density of states relative to band edges of the chosen semiconductor as well as fabrication techniques.

References

1. Ghilane, J., Hapiot, P. & Bard, A. J. Metal/Polypyrrole Quasi-Reference Electrode for Voltammetry in Nonaqueous and Aqueous Solutions. *Anal. Chem.* **78**, 6868–6872 (2006).
2. *Auger and X-ray photoelectron spectroscopy*. (Wiley, 1996).
3. Haber, J. A. & Lewis, N. S. Infrared and X-ray Photoelectron Spectroscopic Studies of the Reactions of Hydrogen-Terminated Crystalline Si(111) and Si(100) Surfaces

with Br2, I2, and Ferrocenium in Alcohol Solvents. *J. Phys. Chem. B* **106**, 3639–3656 (2002).

4. Gleason-Rohrer, D. C., Brunschwig, B. S. & Lewis, N. S. Measurement of the Band Bending and Surface Dipole at Chemically Functionalized Si(111)/Vacuum Interfaces. *J. Phys. Chem. C* **117**, 18031–18042 (2013).
5. Ferrari, A. C. *et al.* Raman Spectrum of Graphene and Graphene Layers. *Phys. Rev. Lett.* **97**, 187401 (2006).
6. Gorbachev, R. V. *et al.* Hunting for Monolayer Boron Nitride: Optical and Raman Signatures. *Small* **7**, 465–468 (2011).
7. Ferrari, A. C. Raman spectroscopy of graphene and graphite: Disorder, electron–phonon coupling, doping and nonadiabatic effects. *Solid State Commun.* **143**, 47–57 (2007).
8. Cassabois, G., Valvin, P. & Gil, B. Hexagonal boron nitride is an indirect bandgap semiconductor. *Nat. Photonics* **10**, 262–266 (2016).
9. Grimm, R. L. *et al.* Comparison of the Photoelectrochemical Behavior of H-Terminated and Methyl-Terminated Si(111) Surfaces in Contact with a Series of One-Electron, Outer-Sphere Redox Couples in CH3CN. *J. Phys. Chem. C* **116**, 23569–23576 (2012).
10. Denis, P. A. & Iribarne, F. Comparative Study of Defect Reactivity in Graphene. *J. Phys. Chem. C* **117**, 19048–19055 (2013).
11. Banhart, F., Kotakoski, J. & Krasheninnikov, A. V. Structural Defects in Graphene. *ACS Nano* **5**, 26–41 (2011).

Chapter 4

Integration of graphene into a strain-based chemiresistive sensor

While covalent functionalization has become an ubiquitous method to control the physical, optical, and electrical properties of graphene, the inhomogeneity of the distribution of functional groups across the basal plane has stymied the integration of functionalized graphene into commercial devices, which typically require a high degree of fidelity for successful scale-up. Existing methods for covalent functionalization rely on the formation of widespread defects in the pristine graphene basal plane before the attachment of functional groups to the surface, degrading the final quality of the lattice. Thus, researchers have developed new graphene-polymer composites to introduce new functionalities to graphene without destroying the lattice. Polymer composites have the advantage of better reproducibility and strength than either the polymer or graphene alone. These composites have been used successfully in a number of sensor devices, but still rely on integration with oxidized graphene flakes instead of pristine graphene due to the lack of known methods for maintaining the lattice.

Graphene strain sensors are a well-developed area of study but have rarely been used as chemiresistors, in part because the graphene in these sensors is typically integrated with a polymer that does not readily respond to the presence of a vapor (i.e. polydimethylsiloxane (PDMS)). However, strain-based graphene devices, which rely on changes to the resistance of graphene at the surface through increased electron localization, have recently been introduced as a method for the controlled reaction of various molecules with the surface of graphene without permanently damaging the lattice through oxidation. This strain-based approach to altering reactivity is possible, because the graphene lattice can undergo substantial deformation without breaking.[1] When the lattice of graphene is deformed through the application of compressive or tensile strain, the bond lengths with the lattice change based on the direction of the strain. Tensile strain is of particular interest as it is easier to access experimentally, since current techniques for inducing compressive strain in graphene typically result in permanent wrinkles with no long range order.[2–4] Current transfer methods typically introduce measurable amounts of strain to the lattice. Transmission electron microscopy (TEM) experiments have shown that even pristine graphene suspended away from a substrate contains some number of ripples a few nanometers in height.[2]

In this chapter, a sensor substrate was developed to support graphene as a partially suspended layer above the surface. By suspending the graphene, material is allowed to expand and contract in response to the movement of a polymer overlayer. In this way, the sensor can access both the sensitivity of the graphene and the specific response of different polymers.

Methods

Materials

CVD-grown monolayer graphene on Cu (Cu/Gr) was purchased from Advanced Chemical Supplier Materials (Medford, MA). Grains of graphene from this source are known to be around 50 μm in diameter as reported by the manufacturer. Poly(ethylene-*co*-vinyl acetate) (PEVA, vinyl acetate 18 wt. %) was purchased from Sigma Aldrich. Black Pearls 2000 carbon black (Cabot Co.) were used in the control solutions. All solvents were purchased reagent grade from VWR and used without further purification to generate the vapors tested herein.

Sensor Fabrication

The textured sensor substrates were prepared in a Class 100 cleanroom. Glass slides were first cleaned with acetone and isopropanol before baking at 170°C to remove any residual solvent. Microposit S1813 photoresist (MicroChem) was spun onto the cleaned slide at 500 rpm for 30 s and 4000 rpm for another 60 s followed by a 10 s exposure to a 425 nm lamp in a contact mask aligner (Suss MicroTech MA6/BA6) through the appropriate mask. The pattern was developed in MF-319 developer (MicroChem) for 90 s. Columns of different heights were grown on the patterned slide by depositing 50 to 300 nm of silicon dioxide with an e-beam evaporator (CHA Industries Mark 40). Lift-off was completed by sonicating the slides at 60°C in Remover PG (MicroChem) for 45 minutes. Contacts were formed by sequentially evaporating 5 nm of Ti, followed by 45 nm of Au, onto masked glass slides. This process produced two metallic electrodes that were separated by a 0.3 cm gap.

Solutions of 4 wt. % PEVA in toluene were sonicated for 2-4 h until the PEVA was well dispersed. To make the coated sensors, a strip of copper covered by monolayer graphene (Cu/Gr) was coated with a supporting layer of PEVA at the selected speed (1000-8000 rpm) for 60 s. The resulting stack (Cu/Gr/PEVA) was then cured for 1 minute at 150°C. Smaller pieces approximately 1 cm x 3 mm (active area ~0.1-0.2 cm^2) were cut and etched in a $FeCl_3$ etch solution (Copper etch, Transene) until the copper was gone by visual inspection, approximately 1.5h. This copper-free piece (Gr/PEVA) was transferred to a ≥18MΩ-cm resistivity water bath for 1h before transfer to a second clean water bath were it was left for 12h. After transfer to a final fresh water bath, the stack was pulled onto the appropriate sensor substrate and dried using a gentle stream of nitrogen.

The sensors used as controls were fabricated using similar transfer techniques. Solutions of 4 wt. % PEVA and 1 wt. % CB were sonicated for 2-4h until well dispersed. The solution was then spun onto bare copper and transferred as before or applied to the sensors using an airbrush. Graphene with no PEVA coating was transferred with a supporting layer of 495K A4 polymethyl methacrylate (PMMA, MicroChem) spun at 3000 rpm for 60 s. After transfer, the PMMA was removed by soaking the sensor in acetone for 10 minutes.

Instrumentation

Sensors were tested using a custom setup that has been described previously. Nitrogen was used as a carrier gas through the bubblers at a flow rate of 3000 mL/min. Organic vapors were generated by sparging N_2(g) through 45 cm tall bubblers that had been filled with the appropriate solvents. The analyte concentration was controlled by adjusting the volumetric mixing ratio of the saturated analyte stream to the background N_2(g) stream. The flow rates of the background and analyte gases were regulated using mass flow controllers. Each run started with a 700 s background collection. Each analyte exposure consisted of 200 s of pure background gas, 80 s of diluted analyte, and then 200 s of background gas to purge the system. The sensors were loaded into a rectangular, 16-slot chamber connected by Teflon tubing to the gas delivery system. The resistance of each of the sensors in the array was measured by a Keithley 2002 multimeter coupled to a Keithley 7001 multiplexer. The measurement electronics were interfaced with a computer via a GPIB connection and were controlled with LabVIEW software.

Profilometry data of the polymer overlayers was collected on a Bruker Dektak XT profilometer using a probe with a 2 μm tip radius. Atomic force microscope images of the sensors were collected using a Bruker Dimension Icon atomic force microscope. Raman spectra were collected with a Renishaw Raman microscope at λ=532 nm through an objective with numerical aperture=0.75. The laser power was ~3 mW.

Results

Figure 1 shows the response of a sensor coated with Gr/PEVA to a single pulse of vapor. Upon exposure of the sensor to the analyte, the resistance steadily increases until the analyte is purged from the chamber, at which point the resistance decreases back to the baseline value. The response from this sensor is quantified as the change in resistance (ΔR) with respect to the resistance of the baseline (R_b), shown below in Equation 1, where R_p is the peak resistance of the sensor.

$$S = \frac{R_p - R_b}{R_b} * 100 = \frac{\Delta R}{R_b} * 100 \qquad (1)$$

The responses for all sensors in this work will be reported as $\Delta R/R_b$.

Several sets of control sensors were fabricated to compare with the optimized sensor design. Typical polymer composite sensors contain carbon black (CB) as a conductive material. The percent composition by weight of CB determines the baseline resistance and the optimal sensor response. The sensors in this work replace CB with a conductive monolayer of graphene. The control samples included graphene alone on a flat substrate, graphene on 150 nm columns, PEVA/CB transferred in various ways to flat substrates and substrates with columns (Figure 2). The sensors fabricated in this work on a substrate with 150 nm columns show the best response by far (Figure 3). Strikingly, the PEVA/CB composite sprayed onto the surface of a substrate shows a strong negative response to ethanol and ethyl acetate, behavior which has been reported previously for these sensors.[5] However, the PEVA/CB composites formed as uniform films show a positive response instead.

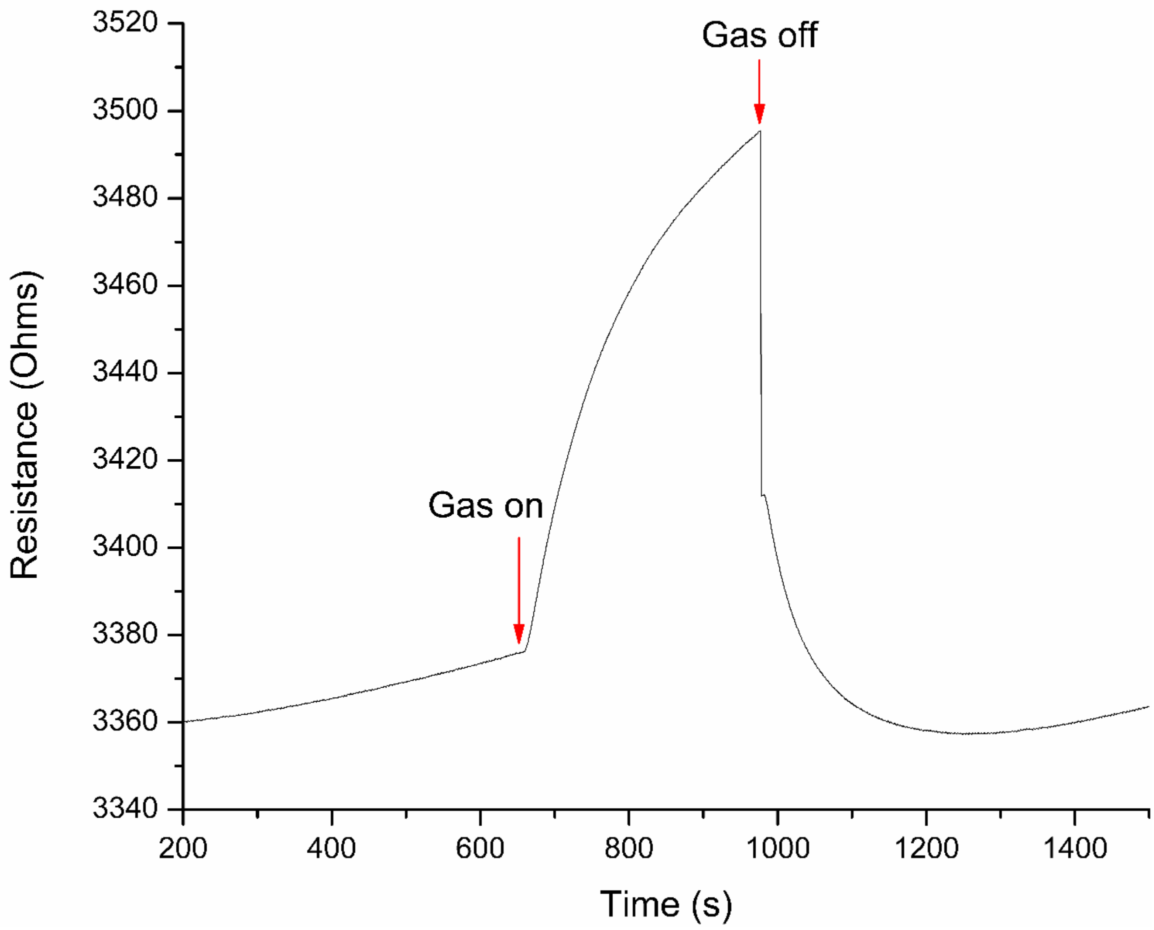

Figure 1. A typical sensor response. The points at which the sensor was exposed to the analyte and purged with the carrier gas are marked above.

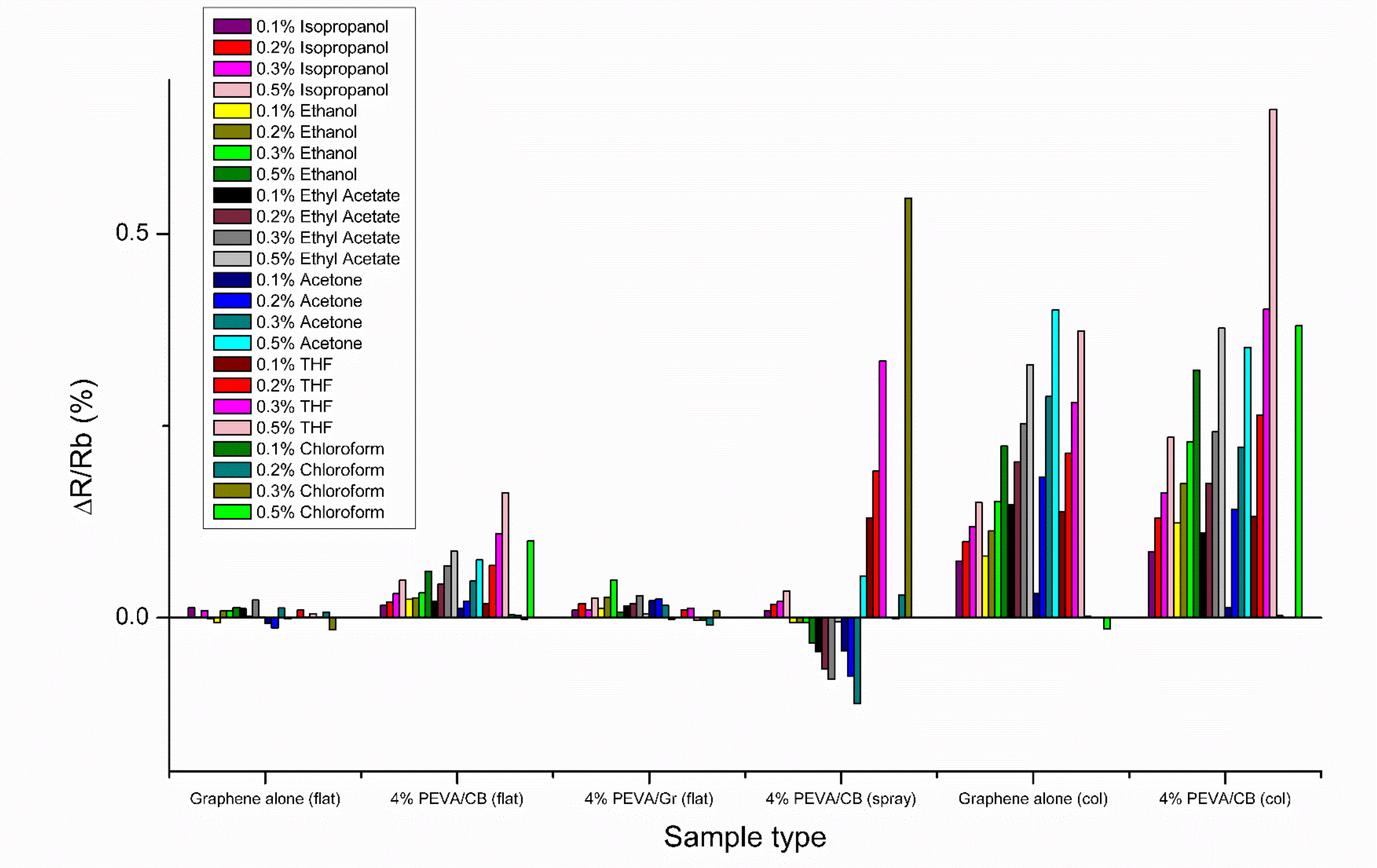

Figure 2. Responses from control sensors. The type of material the sensing material is shown below the x-axis with the type of substrate listed in parentheses. Textured substrates with columns are abbreviated as (col) while flat substrates are (flat).

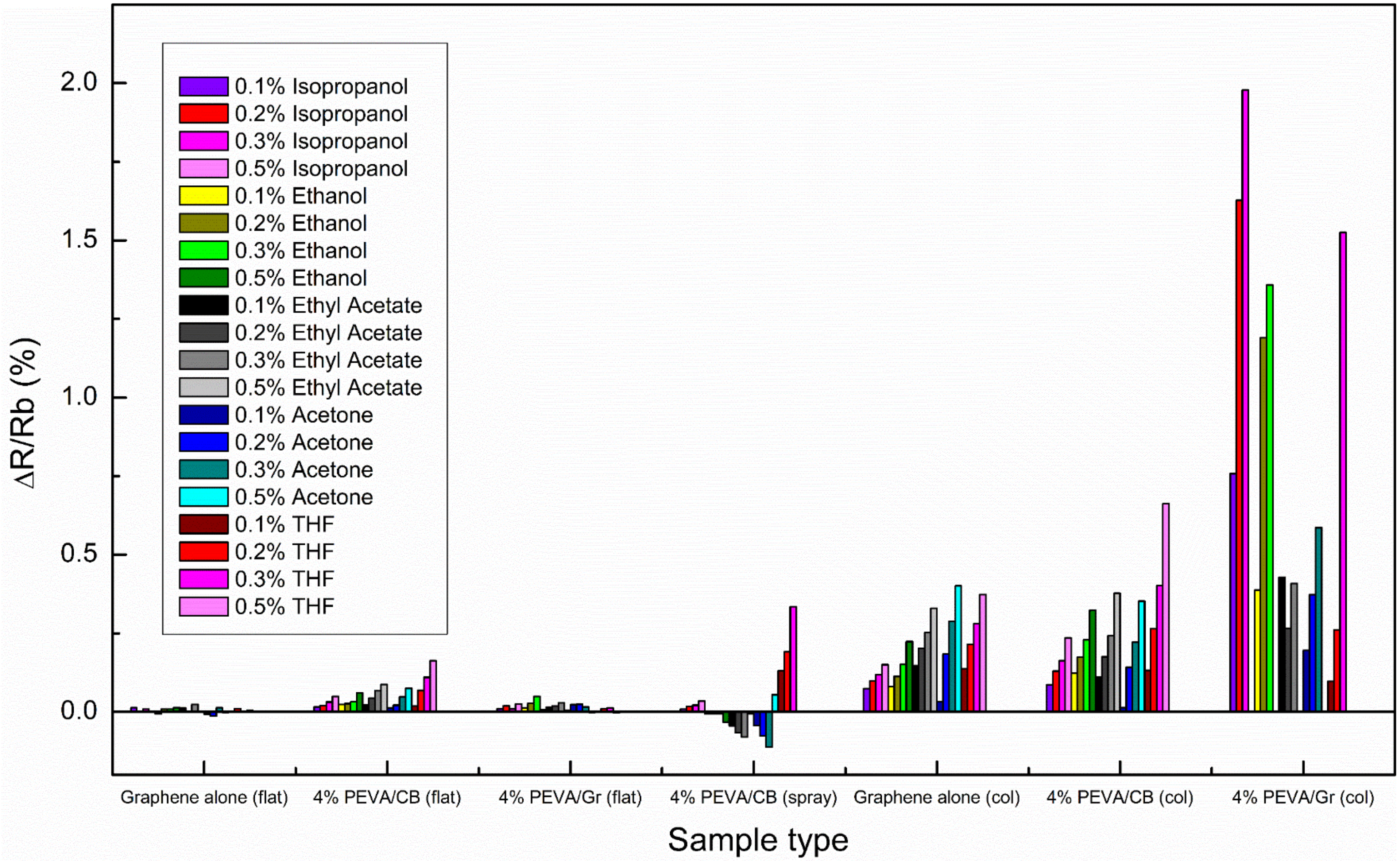

Figure 3. Control sensors versus PEVA/Gr on columns (far right). The best response comes from the PEVA-graphene film on a glass substrate with 150 nm high columns with a 3 μm diameter and 7 μm pitch. This design outperforms PEVA-CB and graphene alone.

The sensors in this work were optimized for the ideal thickness of the polymer overlayer (Figure 4). A spin curve for the 4 wt. % PEVA solution in toluene shows the expected dependence of thickness, which goes as the square root of the speed. Figure 4b shows the responses for sensors with the polymer overlayer spun on at speed between 1000 and 8000 rpm. Although the thickest layer (~320 nm) showed a strong response to various analyte, the responses increase significantly for sensors with thinner layers of PEVA.

The sensors were similarly optimized for the number of columns on the substrate, shown in Figure 5. The standard pattern were columns with 3 μm diameter and a pitch of 7 μm. The pitch was then varied between 7 and 120 μm with a constant thickness of polymer overlayer and size of the Gr/PEVA sheet transferred. As the number of columns decreased, so did sensor response. Figure 5b shows the response with respect to the number of columns and show a plateau around 500,000 columns.

The reproducibility of the responses of the optimized sensor was also probed through repeated measurements of response to the same amount of analyte. Figure 7 shows the response of an optimized sensor upon repeated exposures to 0.3% acetone. The response decreases over time to a plateau at 60% of the original signal, but after being allowed to rest, the sensor recovers the full response seen initially.

Raman spectra were collected for a sensor in contact with a 0.3% exposure of acetone. Figure 7 shows the response before and after exposure to the analyte. The G and 2D peaks of graphene can be seen. An additional broad peak from the substrate can be seen at 2400 cm^{-1}. This substrate peak does not shift upon exposure, while the 2D and G peaks shift significantly higher in energy upon exposure. The shift to higher energies is indicative of contraction of the lattice (Figure 7a).

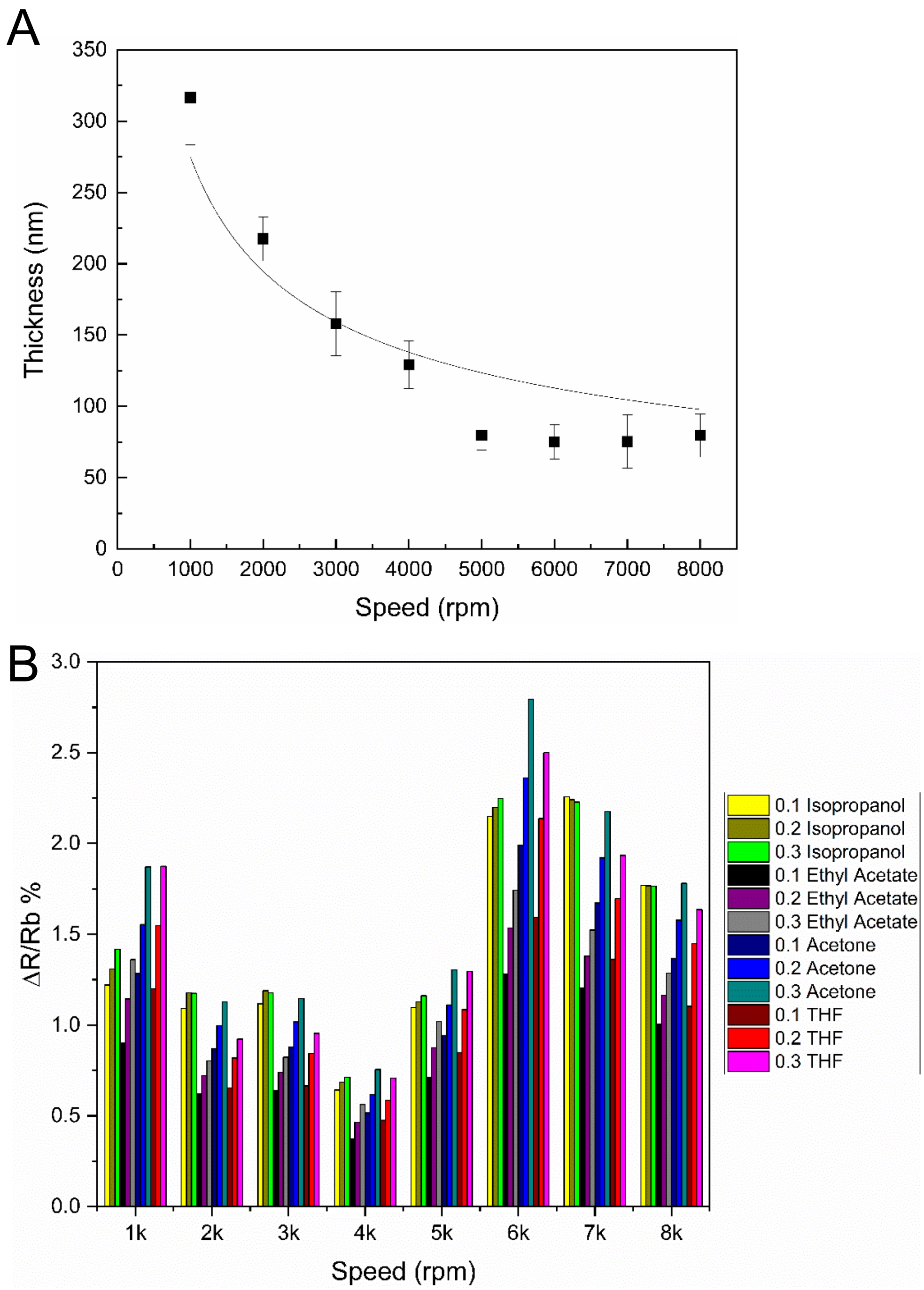

Figure 4. Effect of polymer overlayer on response. A) Polymer spin curve for a 4 wt. % solution of PEVA in toluene. B) Responses for different thicknesses of polymer. The best sensitivity and response is seen from the samples spun at 6000 rpm.

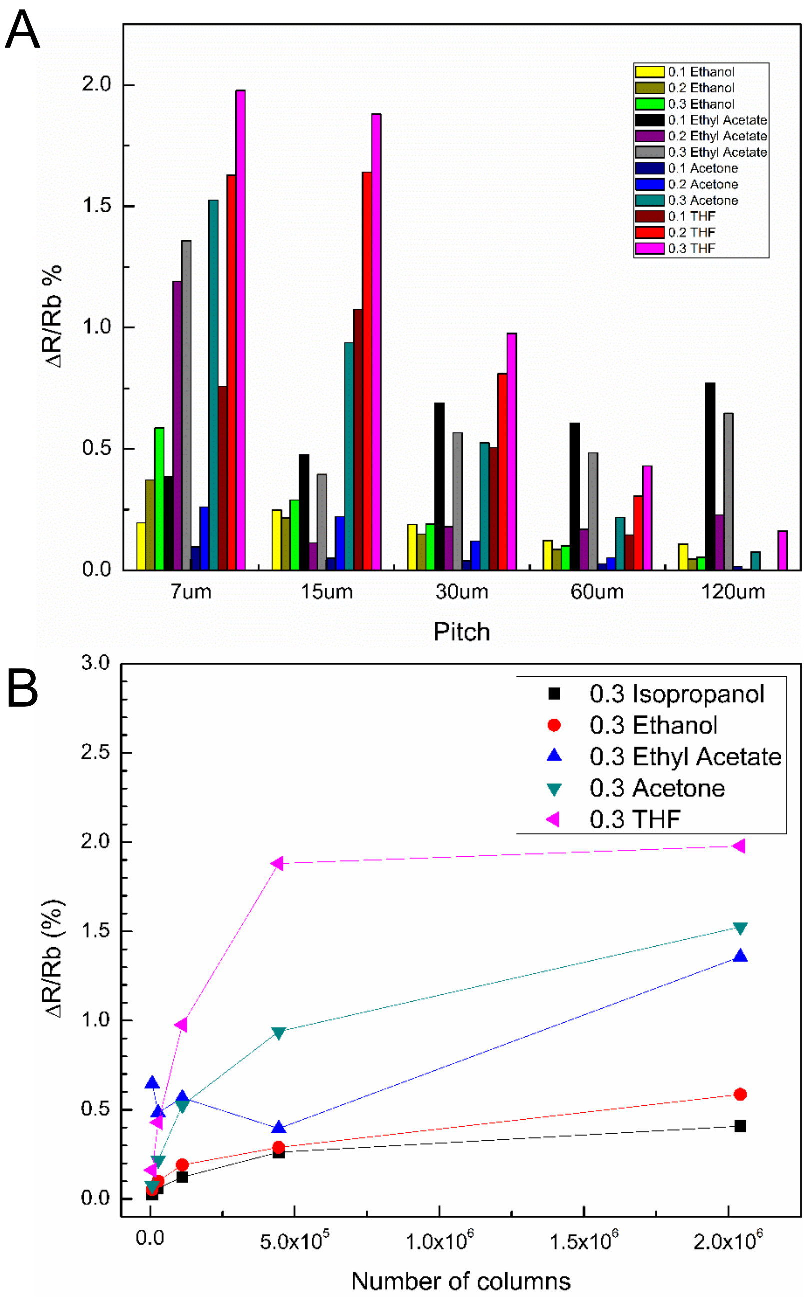

Figure 5. Effect of pitch on response. A) Comparison of responses with changing pitch. More closely spaced columns improve the response of the film. B) While the number of columns makes a large difference initially, the magnitude of response begins to plateau after enough columns are added.

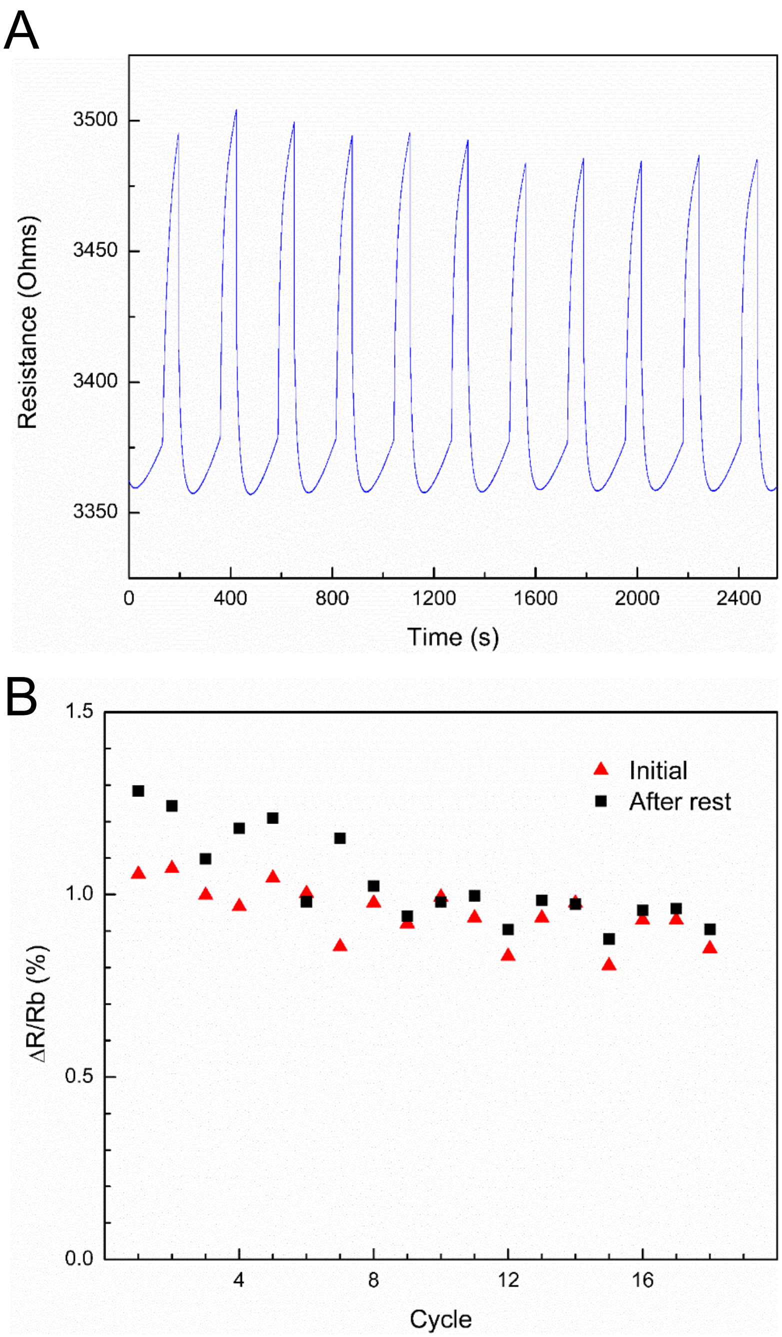

Figure 6. Stability of the polymer-graphene chemiresistors. A) Change in 0.3% acetone response versus time. Although the magnitude of the response decreases slightly, the shape of the response does not change over repeated exposures. B) Initial responses to 0.3% acetone compared to the same exposures after letting the sensor rest for an hour. The response fully recovers after this prolonged rest.

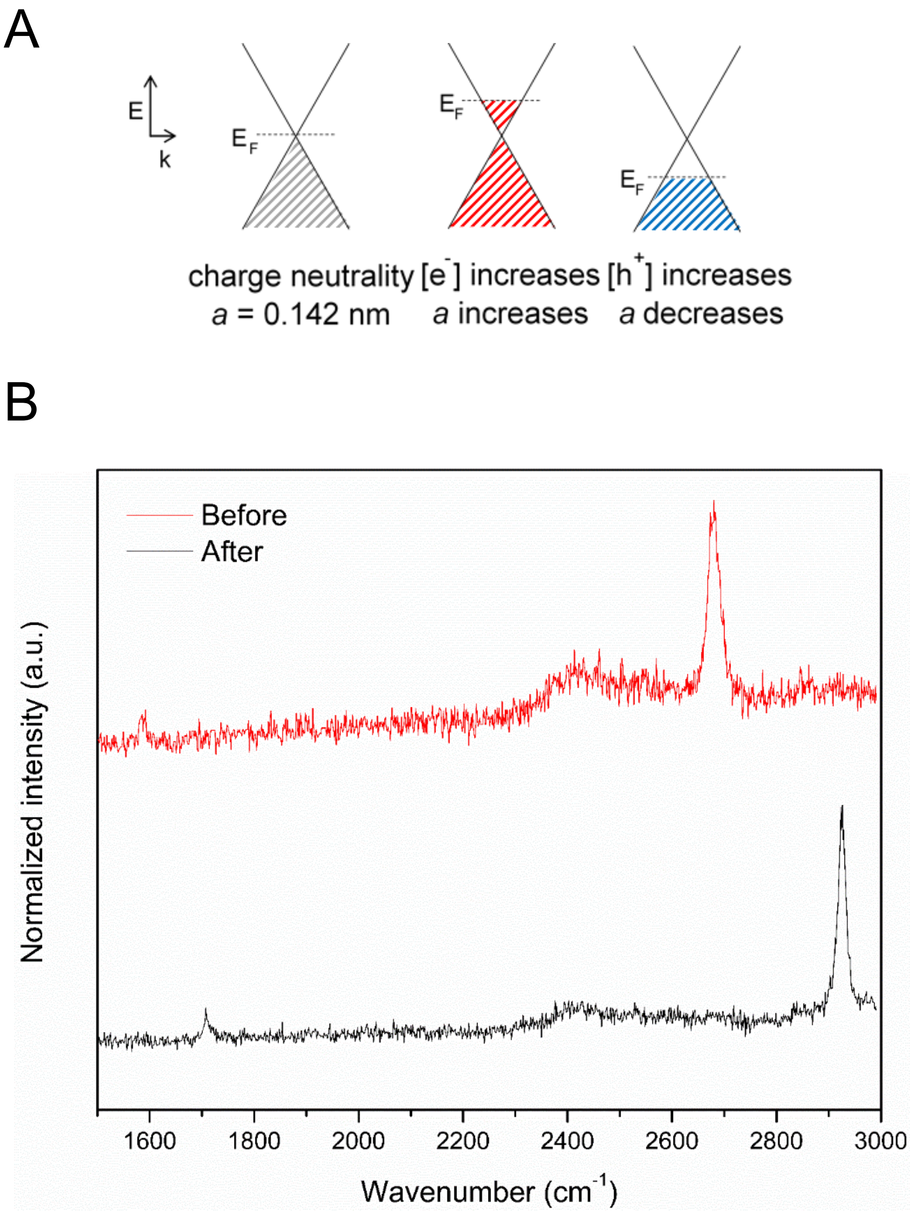

Figure 7. Raman at a representative spot on a sensor. A) How a lattice change in graphene is related to the shift in Fermi level. B) Before exposure to acetone, the G peak (1580 cm^{-1}) and 2D peak (2670 cm^{-1}) are visible. After exposure, both have shifted significantly to higher wavenumbers. This shift indicates that the graphene in this region has likely contracted, which leads to changing conductive pathways through the graphene, measured as a change in resistance.

Discussion

The response of the optimized sensors described here show a strong dependence on the number of columns (Figure 5). On this scale, increasing the number of columns leads to a higher response until a plateau is reached at 500,000 columns. This plateau indicates that on this scale that the resistance change in the graphene is limited by the degree of strain that an analyte can impose on the PEVA/Gr stack as more columns do not substantially enhance the signal. Response also depends on the thickness of the polymer overlayer, scaling proportional to the square root of the thickness (Figure 4). The optimal thickness is then around 70 nm, while the optimal spacing is columns with a 3 μm diameter and 7 μm pitch. While the signal does degrade overall, the sensors have highly reproducible signals but a long recovery time (Figure 6).

Raman spectroscopy has been established as the primary method to characterize strain in graphene. A Raman spectrum of pristine graphene has two main peaks, at 1560 cm^{-1} and 2700 cm^{-1}, which are labeled as the G and 2D peaks, respectively. Both arise from the breathing mode of the graphene lattice.[6] These characteristic peaks are very responsive to small perturbations in the electronic structure of the graphene lattice, such as any shift of the Fermi level of graphene (E_F). As strain is known to change the localization of electron density in graphene and shift E_F, compressive and tensile strain can readily be identified. Tensile strain leads to a red shift of the G peak on the order of hundreds of wavenumbers (cm^{-1}) while compressive strain leads to a slightly smaller blue shift of the G peak (around 20 cm^{-1}).[7] When the lattice is disrupted through the formation of defects, a third peak appears in the spectrum around 1320 cm^{-1} and is labeled the D peak. The intensity of the D peak correlates to the degree of lattice disruption.[8] Consequently, the introduction of defects to the lattice alters the Raman spectrum of graphene in an essentially orthogonal manner to strain-induced changes. The ratio of the intensity of the D peak to the G peak (I_D/I_G) can be used as a metric for the growth of defects in the graphene while the shifts of the G and 2D peaks are indicative of a strained monolayer of graphene. However, it is important to note that any shift in E_F results in changes to the shifts of the G and 2D peak. Thus, it is particularly important to characterize the strained surface before and after functionalization to isolate any changes from the shift of E_F due to strain from those due to fabrication. Here the Raman spectrum (Figure 7) demonstrates that sensor exposed to analyte undergoes a significant shift in the Fermi level, indicative of a large change in the surface strain. When the analyte is removed, the original spectrum can be obtained. No permanent defects are introduced as only the 2D and G peaks are visible in both spectra.

Conclusion

This work demonstrates that polymer-coated monolayer graphene can be integrated with a simple textured electrode to produce a stronger response than a polymer-CB film or graphene alone. The response is controlled by the structure of the underlying substrate along with the thickness of the polymer overlayer. While this sensor has a long recovery time for successive tests, it recovers full functionality after rest period. Raman indicates that the monolayer of graphene is intact on the substrate and undergoes electronic changes when exposed to an analyte.

References

1. Lee, C., Wei, X., Kysar, J. W. & Hone, J. Measurement of the Elastic Properties and Intrinsic Strength of Monolayer Graphene. *Science* **321**, 385–388 (2008).
2. Deng, S. & Berry, V. Wrinkled, rippled and crumpled graphene: an overview of formation mechanism, electronic properties, and applications. *Mater. Today* **19**, 197–212 (2016).
3. Chen, W. *et al.* Controllable Fabrication of Large-Area Wrinkled Graphene on a Solution Surface. *ACS Appl. Mater. Interfaces* **8**, 10977–10984 (2016).
4. Jung, W.-B., Cho, K. M., Lee, W.-K., Odom, T. W. & Jung, H.-T. Universal Method for Creating Hierarchical Wrinkles on Thin-Film Surfaces. *ACS Appl. Mater. Interfaces* **10**, 1347–1355 (2018).
5. Doleman, B. J., Lonergan, M. C., Severin, E. J., Vaid, T. P. & Lewis, N. S. Quantitative study of the resolving power of arrays of carbon black-polymer composites in various vapor-sensing tasks. *Anal. Chem.* **70**, 4177–4190 (1998).
6. Ferrari, A. C. *et al.* Raman Spectrum of Graphene and Graphene Layers. *Phys. Rev. Lett.* **97**, 187401 (2006).
7. Bissett, M. A., Tsuji, M. & Ago, H. Strain engineering the properties of graphene and other two-dimensional crystals. *Phys. Chem. Chem. Phys.* **16**, 11124–11138 (2014).
8. Beams, R., Gustavo Cançado, L. & Novotny, L. Raman characterization of defects and dopants in graphene. *J. Phys. Condens. Matter* **27**, 083002 (2015).